Progress Towards an Atomic Metamaterial

by

Zachary Noel Buckholtz

A dissertation submitted in partial fulfillment

of the requirements for the degree of

Doctor of Physics

(Physics)

At the

UNIVERSITY OF WISCONSIN-MADISON

2020

Date of final oral examination: May 14, 2020

The dissertation is approved by the following members of the Final Oral Committee:

Deniz D. Yavuz, Professor, Physics

James E. Lawler, Professor, Physics

Shimon Kolkowitz, Professor, Physics

John C. Wright, Professor, Chemistry

I do not think that the wireless waves I have discovered will have any practical application.

-Heinrich Hertz on his discovery of radio waves.

Acknowledgements

First off, I would like to thank my advisor, Deniz Yavuz. In addition to being very knowledgeable about physics, Deniz was always willing to talk and has always been eager to help and willing to listen when I needed someone to bounce ideas off of.

I would also like to thank my lab mates. Nick Brewer and Zach Simmons did an excellent job showing me the ropes and preparing me to take the lead on the negative index project. David Gold, Ben Lemberger, and Dipto Das had many helpful discussions with me as well. I would also like to thank Eli Mueller for his work around the lab. Last but not least, I would like to thank Josh Karpel, whose five years in the same office with me melded us into the same person. I would also like to commend Josh on his outstanding leadership on the board of Couch Club and Office Outing.

There are many people around the department I would like to thank as well. Ann Austin has always been a huge help with our orders. Keeley Bannon has been kind enough to supply me with folders so that my desk didn't become a huge pile of papers. Instead, it became a huge pile of folders. Sara Yeager has also been extremely helpful for having the patience to reteach me everything ever time I went into the machine shop. I'd also like to thank Brett Unks for keeping a cool head despite all the broken lab equipment and for being such a wonderful sailor.

I'd like to thank Jim Reardon for all his effort towards making TAing as accommodating as possible. I really appreciate that he and Deniz gave me the opportunity to work on lab development for Physics 325 and 707. I have had many other great teaching op-

portunities in the department with Susan Coppersmith, Pupa Gilbert, Baha Balantekin, Francis Halzen, Jim Lawler, and Shimon Kolkowitz, all of whom were a pleasure to work with. I'd also like to thank Susan Nossal for bringing me into the Physics Learning Center and for all I learned there. I'd also like to thank her for all her support and encouragement as I made the transition to atmospheric science.

I would also like to thank my cohorts, Steven Casper, Adrian Fraser, Sam Neyens, Chris Yip, Patrick Vanmeter, and Bunheng Ty who have all been lasting and honorable members of Couch Club, Office Outing, and Friday Feast. I probably learned more about physics from our endless arguing than I did from my classes.

I'd like to thank Neil Campbell, Ben Rosenwaser, and Gage Bonner. It is now day 55 of quarantine and, despite the many uncleaned French presses, have managed to make this stay-at-home period manageable. There will be many more omelets and pies in our future.

Finally, I would like to thank my parents, Debbie and Steve Buckholtz. Their support and encouragement have been a big reason I made it to the finish line. I also appreciate their reminders that I could always stay with them if I couldn't find a job.

Contents

List of Figures

Abstract

Progress Towards an Atomic Metamaterial

Zachary Noel Buckholtz

Under the supervision of Professor Deniz D. Yavuz

At the University of Wisconsin - Madison

There are no naturally occurring materials with a negative index of refraction (NIM). However, in 1968, Victor Veselago noted that a NIM could in principle be produced if a material had both a negative permittivity and permeability. The idea of a NIM remained relatively unexplored until John Pendry's seminal paper in 2000 where he proposed an implementation of a NIM in the form of a material constructed from metallic nanostructures engineered to have the electric and magnetic response required to produce a negative index, called a metamaterial. Pendry also noted that NIMs could be used to construct so called "perfect lenses", a lens which, in principle, could have infinite resolution. Since the publication of this seminal paper, NIM and metamaterials have been explored both theoretically and experimentally and have found numerous interesting and exotic applications.

However, this form of metamaterials that relies on artificial structures has several limitations, one of which is the smallest scale at which these nanostructures can be produced. Currently, the state of the art puts this scale at about 100 nm. This scale puts limitations on the properties of NIMs, such as the practical limit of resolution of the perfect lens. The main goal of our work is to construct what we are calling an

atomic metamaterial out of a rare-earth doped crystal which will circumvent the scale limitations of traditional metamaterials by using the naturally small scale of the crystal structure (about 1 nm). Rare earths are known to have strong magnetic transitions, which are a requirement for NIMs, in the optical region of the spectrum, but these transitions have remained relatively unexplored.

Our work has focused on the $^7F_0 \rightarrow ^5D_1$ transition in europium doped yttrium orthosilicate (Eu:YSO). We have measured the magnetic dipole moment of this 527 nm transition via Rabi oscillations. We then studied the effects of the host crystal on the dipole moment to understand discrepancies between our measured value and our theoretical value. Our work on Eu:YSO has also included manipulating the linear magnetic response via spectral hole burning, as well as the nonlinear magnetic response via electromagnetically induced transparency. Last, we have theoretically explored implementing a driven negative index scheme using this europium transition in YSO and other host crystals, as well the possibility of using terbium doped crystals.

Chapter 1

Introduction

If there is one thing I've learned in graduate school, it's that you can do just about anything you want to light. Generate it, absorb it, shift the frequency to any frequency, entangle it, manipulate the statistics, even produce a Fourier transform that is floating right in front of your face via Fourier image processing. As long as conservation laws are obeyed and causality isn't violated, then you can probably do it. The restriction of causality is even more loose than might first appear. As it turns out, individual modes and even the entire group velocity can be superluminal and not violate any causal relations.

One of the more interesting ways in which light can be manipulated, in my opinion, has to do with negative indices of refraction. Typically we think of the index of refraction being greater than or equal to 1, otherwise the phase velocity could become greater than the speed of light in a vacuum. However, theoretical and experimental works have shown that such materials are possible and indices less than one or even negative have been demonstrated. When the index of refraction becomes negative, the nonintuitive properties multiply. With a negative index of refraction, the phase velocity becomes negative meaning that the phase is propagating in the opposite direction of the pulse [2]. This phenomenon has consequences ranging from a reversed Doppler effect to the

Sci-Fi evoking radiation tension.

The work in this thesis is aimed at developing what we are calling atomic metamaterials. There are no known natural materials with a negative index of refraction. The main limitation is that a negative index requires a strong response from the material to both the electric and magnetic field of light. Unfortunately, at optical frequencies, the magnetic response is typically orders of magnitude smaller than the electric response. To get around this limitation, researchers have developed what are called metamaterials, materials constructed from arrays of metallic nanostructures that are engineered to have the electric and magnetic response required for a negative index [3]. Although these traditional metamaterials have achieved great success, there are limitations to the smallest wavelength at which these materials can have a negative index. Our atomic approach offers a new route to a negative index that is based on manipulating the response of ions within a solid and opens up the possibility of circumventing the limitations of traditional metamaterials.

The ability to design the index of refraction of a material, whether through traditional or atomic metamaterials, can lead to some pretty astounding applications. Many of these applications were discovered through a field of study that developed alongside metamaterials: transformation optics [4]. Transformation optics uses ideas from differential geometry to describe how light propagates through a material with an index that depends on time and space and is, in some cases, negative. It draws heavily on the techniques of general relativity and has even been used to devise an index profile that would simulate a black hole [5]. Transformation optics has been used to design beam shifters, construct simplified optical systems [6], as well as to tailor the radiation pattern of antennae [7]. Some of the more fantastical sounding applications of transformation optics are the various cloaking schemes. One of the early applications of transformation optics was in designing an index profile that could be used as an invisibility cloak; the incident light would be diverted around an object and then returned to their previous

trajectory [8]. The idea of a spatial cloak was then taken one step further by [9]. There, the authors have devised a temporal cloak; a cloak that hides events rather than objects. The time varying material properties of the temporal cloak achieve this by slowing down the light preceding the event and speeding up the light following the event, resulting in the obfuscation of the event. Such a temporal cloak has been demonstrated in optical fibers [10, 11].

The foundations of transformation optics are quite general and have been applied to other types of waves. The methods of transformation optics have been used to study metamaterials designed for heat waves [12] as well as acoustic waves [13]. Work has even gone into developing seismic metamaterials [14] which offer the possibility of protecting buildings from earthquakes.

Among all the amazing applications of negative indices, the one that has gotten the most attention is the so called perfect lens [3]. A perfect lens is a slab of negative index materials that can resolve sub-diffraction limited features with, in principle, infinite resolution. The slab is able to do this because of particular surface phenomenon at the interfaces between the negative index slab and the positive index material in which the slab is embedded.

Some of the physics of light propagation and index of refraction is reviewed in Chapter 2. It turns out that the theory behind the properties of negative index of refraction is not all that different from positive index materials. However, the content of Chapter 2 is meant to illuminate the origins of the strange properties of negative index materials. In Chapter 2, I also discuss metamaterials and their limitations, as well as a couple of our schemes to implement a negative index in an atomic medium.

In order to understand how to produce an atomic metamaterial, we must understand the material we are starting with. Our approaches utilized rare-earth doped crystals. Rare-earth ions have been shown to exhibit relatively strong magnetic responses. By doping them into a crystal, we are able to achieve much higher densities than we would

with an atomic vapor, which will aid us in achieving a negative index. In chapter 3 I discuss some of the physics of rare earth ions and crystal fields. These concepts are necessary to accurately calculate the magnetic (and electric for that mater) response of our material.

Chapter 4 delves into the details of our crystal, europium doped yttrium orthosilicate. There I talk about the spectral properties of europium ions, as well as the crystal structure of yttrium orthosilicate. The next two chapters discuss the details of our experiments with this crystal. In chapter 5, I discuss our Rabi flopping experiment in which we measured the magnetic dipole moment of a 527.5 nm transition. In chapter 6, I discuss our experiments where we manipulated the response of this transition. These experiments include spectral hole burning, electromagnetically induced transparency, and linear slow light.

In chapter 6, I discuss our theoretical investigations of terbium and the possibility of implementing one of our schemes in a terbium doped crystal. Experimental investigations of terbium are discussed in chapter 7, along with other potential future directions, such as refinements of our measurements with europium, other host crystals for europium, and combining our observed magnetic response in europium with an electric response to produce a negative index.

Chapter 2

Negative Index of Refraction

2.1 Brief Review of Light Propagating Through a Medium

Before we get too far into discussions about index of refraction, it will be useful to review some properties of electromagnetic fields in dielectric and magnetic materials. This will mainly be discussions and equations from E&M class, but cast in a way that lends them to discussions of negative indices of refraction. The materials we will discuss are assumed to be isotropic, homogeneous, and have no free charges or currents.

Let's begin with the constitutive relations. When matter is exposed to electric and magnetic fields, the atoms that compose the material respond according to the electric and magnetic susceptibilities, χ_E and χ_M. For an electric field, the material becomes polarized according to

$$\vec{P} = \epsilon_0 \chi_E \vec{E} \tag{2.1}$$

where ϵ_0 is the permitivity of free space. This is typically combined with the electric field within the material to give the displacement field

$$\vec{D} = \epsilon_0 \vec{E} + \vec{P} = \epsilon_0 (1 + \chi_E) \vec{E} = \epsilon \vec{E} \tag{2.2}$$

thus defining the permitivity of the material

$$\epsilon = \epsilon_0(1 + \chi_E). \tag{2.3}$$

Similar relations can be found for the magnetic field where the magnetization

$$\vec{M} = \chi_M \vec{H} \tag{2.4}$$

replaces the polarization and

$$\vec{B} = \mu_0(\vec{H} + \vec{M}) = \mu_0(1 + \chi_M)\vec{H} = \mu\vec{H} \tag{2.5}$$

where μ_0 is the permeability of free space, μ is the permeability of the material and is defined as

$$\mu = \mu_0(1 + \chi_M). \tag{2.6}$$

Typically $\mu \approx \mu_0$ at optical frequencies.

Maxwell's equations for a material with no free charges or currents are

$$\nabla \cdot \vec{D} = 0 \tag{2.7a}$$

$$\nabla \cdot \vec{B} = 0 \tag{2.7b}$$

$$\nabla \times \vec{E} = -\frac{\partial \vec{B}}{\partial t} \tag{2.7c}$$

$$\nabla \times \vec{H} = \frac{\partial \vec{D}}{\partial t}. \tag{2.7d}$$

These equations, along with the divergence theorem and Stokes's theorem give us the

boundary conditions

$$D_{1,\perp} = D_{2,\perp} \tag{2.8a}$$

$$B_{1,\perp} = B_{2,\perp} \tag{2.8b}$$

$$E_{1,||} = E_{2,||} \tag{2.8c}$$

$$H_{1,||} = H_{2,||}. \tag{2.8d}$$

If we take Maxwell's equations and the vector identity:

$$\nabla \times (\nabla \times) = \nabla(\nabla \cdot) - \nabla^2 = -\nabla^2 \tag{2.9}$$

we find that the electric and magnetic fields obey the wave equations

$$\nabla^2 \vec{E} = \epsilon\mu \frac{\partial^2 \vec{E}}{\partial t^2} \tag{2.10a}$$

$$\nabla^2 \vec{B} = \epsilon\mu \frac{\partial^2 \vec{B}}{\partial t^2} \tag{2.10b}$$

where the prefactor on the right is equal to one over the phase speed squared. In general, both ϵ and μ are functions of frequency.

We can factor out the free space phase values of ϵ and μ to get

$$\epsilon\mu = \epsilon_0\mu_0 \frac{\epsilon}{\epsilon_0}\frac{\mu}{\mu_0} = \frac{1}{c^2}\epsilon_r\mu_r = \frac{n^2}{c^2} \tag{2.11}$$

where ϵ_r and μ_r are the relative permitivity and permeability, respectively, and the factor

$$n = \sqrt{\epsilon_r\mu_r} \tag{2.12}$$

is the index of refraction, and we see that the index of refraction describes how the phase speed of light propagating through a medium differs from that of free space. If we take

either of the Eqs. 2.10 and substitute in a monochromatic wave

$$\vec{E} = \vec{E}_0 e^{i(\vec{k}\cdot\vec{r}-\omega t)} \tag{2.13a}$$

$$\vec{B} = \vec{B}_0 e^{i(\vec{k}\cdot\vec{r}-\omega t)}, \tag{2.13b}$$

where $|E_0|$ and $|B_0|$ are the amplitudes of the fields and we assumed linear polarization for simplicity, we find the dispersion relation

$$\frac{\omega}{k} = \frac{c}{n} \tag{2.14}$$

We can also use Eqs. 2.13 to find a relationship between the magnitude of the electric and magnetic fields. Let's take Eqs. 2.13, plug them into Eq. 2.7c, and take the absolute value to get

$$k|E| = \omega|B| \rightarrow |E| = \frac{\omega}{k}|B| = \frac{c}{n}|B|. \tag{2.15}$$

which can be expressed as

$$|E| = \frac{c}{n}\mu|H| = \frac{1}{\sqrt{\epsilon\mu}}\mu H = \sqrt{\frac{\mu}{\epsilon}}|H| = \eta|Z||H| \tag{2.16}$$

by using Eq. 2.5. The quantity

$$Z = \eta\left|\sqrt{\frac{\mu}{\epsilon}}\right| \tag{2.17}$$

is the impedance of the material and η is the sign of the square root in Eq. 2.17 which will be useful later.

Eq. 2.15 is often used with the Poynting vector to get a relationship between the electric field and the time-averaged intensity of the beam propagating in a nonmagnetic material. This relationship is often expressed as $I = \frac{1}{2}cn\epsilon_0|E|^2$. Since we will be working

with magnetic materials, it will be useful to reexpress this equation, using Eq. 2.11, as

$$I = \frac{1}{2}|\vec{E} \times \vec{H}^*| = \frac{1}{2}\frac{|E|^2}{Z}. \tag{2.18}$$

We can use Eq. 2.16 to find the relation between the magnetic field magnitude and the beam intensity to be

$$I = \frac{1}{2}Z|H|^2. \tag{2.19}$$

Reflection, Transmission, and Refraction

The boundary between a positive and negative index material is of special interest because phenomenon at the surface are what give negative index materials some of their more interesting properties, such as negative refraction and perfect lensing. To derive Snell's law, we often look at the boundary condition in Eq. 2.8c. Because the component of the electric field that is parallel to the interface must be equal on each side of the boundary, the phase, $e^{i\vec{k}\cdot\vec{r}}$, must also be equal anywhere along the interface, meaning

$$\begin{aligned} \vec{k}_i \cdot \vec{r}|_{interface} &= \vec{k}_r \cdot \vec{r}|_{interface} = \vec{k}_t \cdot \vec{r}|_{interface} \\ &\rightarrow \frac{2\pi n_1}{\lambda}\sin(\theta_i) = \frac{2\pi n_1}{\lambda}\sin(\theta_r) = \frac{2\pi n_2}{\lambda}\sin(\theta_t) \end{aligned} \tag{2.20}$$

giving us Snell's law

$$n_1 \sin(\theta_i) = n_2 \sin(\theta_t). \tag{2.21}$$

The subscripts 1, 2, i, and t are defined in Fig. 2.1 and r is the label for the reflected beam, which is not shown in the figure. We can follow a similar procedure using the magnetic field as well.

There is an alternative point of view of Snell's law that can provide some intuition

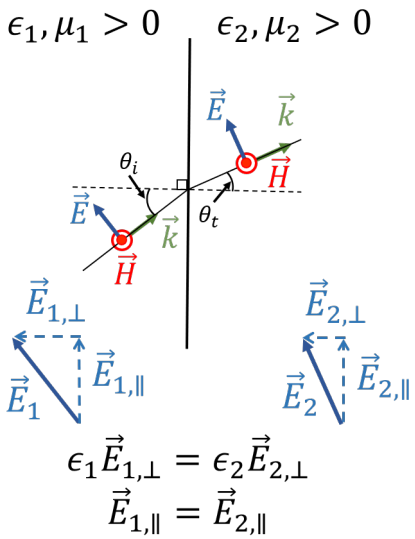

Figure 2.1: The field vectors for an electromagnetic wave incident on an interface between two positive index materials. The subscripts 1 and 2 label the materials that the incident/reflected beams and the transmitted beams travel through, respectively, and the subscripts i and t label the incident angle and transmitted/refracted angle, respectively.

that will be useful for understanding negative refraction. This point of view makes use of two boundary conditions, Eqs. 2.8c and 2.8a (or Eqs. 2.8d and 2.8b if we wanted to look at the magnetic field), and is depicted in Fig. 2.1. Since the electric field vector, magnetic field vector, and k vector form a triad, we can find the change of angle of k by considering the change of angle of the electric field. Only the perpendicular component of the electric field changes as the beam crosses the boundary and this change depends on the dielectric constant of the material, ϵ. For a positive index to positive index interface, both dielectric constants are also positive and so the perpendicular component of the electric field has the same direction on both sides of the interface. However, for a positive index to negative index interface, the dielectric constant switches signs and therefore the direction of the perpendicular component of the electric field switches directions.

The coefficients of reflection and transmission can also be derived using the boundary

conditions for Maxwell's equations. These are particularly relevant for the perfect lens, which is typically depicted as a slab of negative index material embedded in a positive index material. I think that the easiest way to understand the transmission and reflection from a negative index slab is using the transfer matrix method. Other methods wind up with divergences and handling these can get confusing. More on that later though.

The amount of light reflected or transmitted depends on the boundary conditions in Eq. 2.8. As an example, I will discuss the TE wave pictured in Fig. 2.1. Our boundary conditions say that the total electric field in material one is equal to the total electric field in material two at the boundary (this is because there is no perpendicular electric field component). Similarly, the total parallel H field in material one is equal to the total parallel H field in material two.

$$E_1^+ + E_1^- = E_2^+ + E_2^- \tag{2.22a}$$

$$H_{1,||}^+ + H_{1,||}^- = H_{2,||}^+ + H_{2,||}^- \tag{2.22b}$$

where the $+$ superscript indicates waves moving from left to right, and the $-$ superscript indicates wave moving from right to left. The second equation above can be rewritten using Eq. 2.16,

$$\eta_1 Z_1 \cos(\theta_i)(E_1^+ - E_1^-) = \eta_2 Z_2 \cos(\theta_t)(E_2^+ - E_2^-). \tag{2.23}$$

We can combine the above equations into one single matrix relation

$$\begin{pmatrix} 1 & 1 \\ \eta_2 Z_2 \cos(\theta_t) & -\eta_2 Z_2 \cos(\theta_t) \end{pmatrix} \begin{pmatrix} E_2^+ \\ E_2^- \end{pmatrix} = \begin{pmatrix} 1 & 1 \\ \eta_1 Z_1 \cos(\theta_i) & -\eta_1 Z_1 \cos(\theta_i) \end{pmatrix} \begin{pmatrix} E_1^+ \\ E_1^- \end{pmatrix} \tag{2.24}$$

which becomes [1]

$$\begin{pmatrix} E_2^+ \\ E_2^- \end{pmatrix} = \frac{-1}{2\eta_2 Z_2 \cos(\theta_t)} \begin{pmatrix} -\eta_1 Z_1 \cos(\theta_i) - \eta_2 Z_2 \cos(\theta_t) & \eta_1 Z_1 \cos(\theta_i) - \eta_2 Z_2 \cos(\theta_t) \\ \eta_1 Z_1 \cos(\theta_i) - \eta_2 Z_2 \cos(\theta_t) & -\eta_1 Z_1 \cos(\theta_i) - \eta_2 Z_2 \cos(\theta_t) \end{pmatrix} \begin{pmatrix} E_1^+ \\ E_1^- \end{pmatrix} \tag{2.26}$$

In my view, some of the properties of positive to negative interfaces are easier to understand in terms of these transfer matrices. It is important to note that all of the matrices discussed so far are nonsingular and the elements are finite. The importance of this will become more evident in the context of negative index materials. The field reflection and transmission coefficients are defined in a straightforward manner as

$$r = \frac{E_1^-}{E_1^+} \qquad t = \frac{E_2^+}{E_1^+}. \tag{2.27}$$

Typically, in a real physical situation, there is an incident beam, reflected beam, and a transmitted beam. In other words, $E_2^- = 0$. When this is the case, it is straightforward to derive the reflection coefficient from Eq. 2.26

$$r = \frac{\eta_1 Z_1 \cos(\theta_i) - \eta_2 Z_2 \cos(\theta_t)}{\eta_1 Z_1 \cos(\theta_i) + \eta_2 Z_2 \cos(\theta_t)}. \tag{2.28}$$

The reflection coefficient can be used with Eq. 2.26 to find the transmission coefficient

$$t = \frac{2\eta_1 Z_1 \cos(\theta_i)}{\eta_1 Z_1 \cos(\theta_i) + \eta_2 Z_2 \cos(\theta_t)}. \tag{2.29}$$

[1] The inverse of the matrix on the left side of Eq. 2.24 is

$$\frac{-1}{2\eta_2 Z_2 \cos(\theta_t)} \begin{pmatrix} -\eta_2 Z_2 \cos(\theta_t) & -1 \\ -\eta_2 Z_2 \cos(\theta_t) & 1 \end{pmatrix} \tag{2.25}$$

2.2 What is the Index of Refraction?

The index of refraction is a parameter that describes how light propagates through a material. It describes how the phase velocity and wavelength are modified by the material, angles of refraction, and reflection and transmission coefficients at an interface. However, ultimately, the phenomenon that are typically parameterized by the index of refraction are a result of the electric and magnetic responses of the material, χ_E and χ_M through which the light is propagating.

The motivation for this thesis is negative indices of refraction. However, according to the discussion above, these indices appear to be manifestly unphysical because an index of refraction less than one would allow the phase velocity in the medium to be larger than the speed of light in a vacuum. Have we failed before we even begin? We can better understand the limitations imposed on the index of refraction by studying the limitations on the susceptibilities.

2.2.1 Kramers-Krönig Relations

We can start by taking the Faltung theorem

$$c(\omega) = a(\omega)b(\omega) \rightarrow C(t) = \frac{1}{\sqrt{2\pi}} \int_{-\infty}^{\infty} d\omega c(\omega) e^{-i\omega t} = \int_{-\infty}^{\infty} A(\tau)B(t-\tau)d\tau \qquad (2.30)$$

and identify $a(\omega)$ ($A(t)$) with $\chi_E(\omega)$ ($G(t)$), $b(\omega)$ ($B(t)$) with $E(\omega)$ ($E(t)$), and $c(\omega)$ ($C(t)$) with $D(\omega)$ ($D(t)$). We then get

$$P(t) = \int_{-\infty}^{\infty} G(\tau)E(t-\tau)d\tau. \qquad (2.31)$$

Eq. 2.31 tells us that the polarization at a particular time is dependent on the electric field and response function at all other times due to Eq. 2.30. We are assuming that the spatial variation of the field is much larger than the microscopic spatial scales of the

material.

It is reasonable to assume that the polarization will not be affected by the electric field from some future time. We can use this assumption to make very general statements about the response function G, which is the Fourier transform of the susceptibility

$$G(\tau) = \frac{1}{\sqrt{2\pi}} \int_{-\infty}^{\infty} \chi(\omega) e^{-i\omega\tau} d\omega. \tag{2.32}$$

This integral can be evaluated by contour integration in the complex ω plane. The contours are shown in Fig. 2.2. Lets split it into two cases: $\tau > 0$, for past times, and $\tau < 0$, for future times. For the first case $\tau > 0$, the exponential in Eq. 2.32 becomes

$$-i\omega\tau = -i\omega_r|\tau| + \omega_i|\tau| \qquad \tau > 0. \tag{2.33}$$

In order for the contour integral not to diverge, we must integrate around the lower-half plane. Since it is fine for G to be nonzero for $\tau > 0$, G can have poles in this part of the complex ω plane.

The other case, $\tau < 0$, however, is where the magic happens. In this case the exponential becomes

$$-i\omega\tau = i\omega_r|\tau| - \omega_i|\tau| \qquad \tau > 0 \tag{2.34}$$

and the contour must be around the upper-half plane. Since there can be no response from times where $\tau < 0$, $G(\tau < 0) = 0$ and therefore there G must be analytic in the upper-half plane.

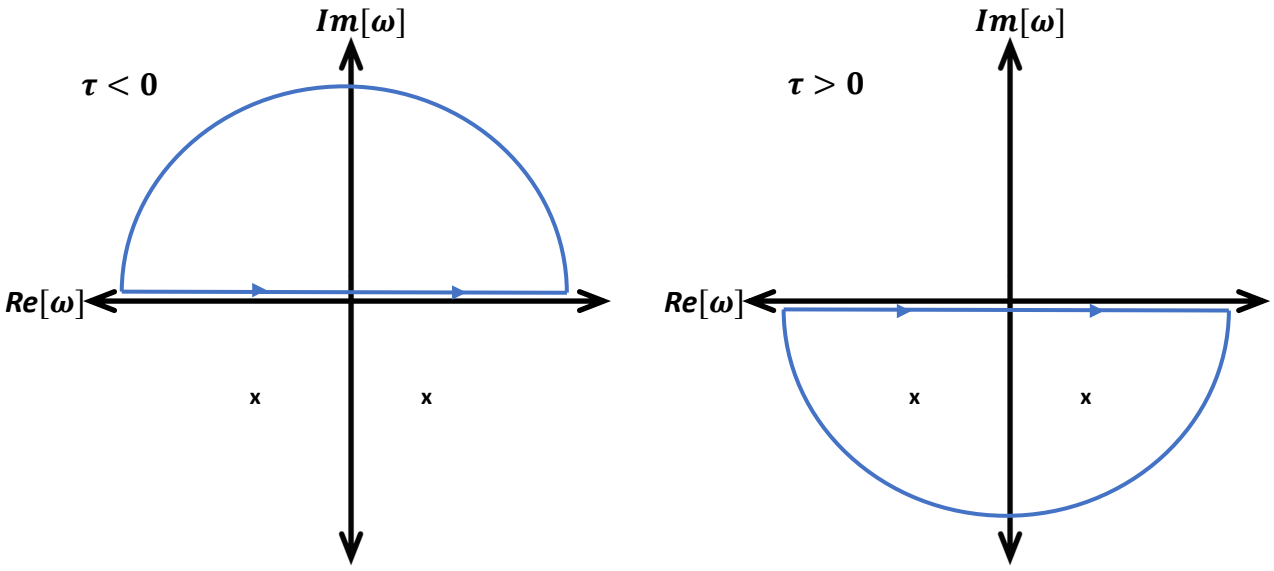

Figure 2.2: The contours for integrating Eq. 2.32. The x's represent the location of χ's poles. For $\tau > 0$ we must integrate around the lower-half plane and we get a nonzero result because of the poles. For $\tau < 0$ we must integrate around the upper-half plane and we get zero.

This restriction has important consequences for the susceptibility. First of all, we can restrict the inverse of Eq. 2.32 to

$$\chi(\omega) = \frac{1}{\sqrt{2\pi}} \int_0^\infty G(\tau) e^{i\omega\tau} d\tau. \tag{2.35}$$

We can use Eq. 2.35 to get a rough idea of the large ω dependence of χ. Due to the cyclic nature of $e^{i\omega\tau}$, for large ω we can restrict our attention to small τ and Taylor expand G

$$G(\tau) \approx G(0) + \tau G'(0) + ... \tag{2.36}$$

Plugging this into Eq. 2.35 and integrating by parts results in

$$g(\omega) \approx i\frac{G(0)}{\omega} - \frac{G'(0)}{\omega^2} + ... \tag{2.37}$$

Since $G(0^-) = 0$ it is reasonable to assume that $G(0^+) = 0$ as well. Thus, the dependence of $g(\omega)$ as $\omega \to \infty$ allows us to take Cauchy's theorem

$$\chi(\omega) = \frac{1}{2\pi i}\oint_C \frac{\chi(\omega')}{\omega' - \omega}d\omega' \tag{2.38}$$

and extend the contour out to infinity resulting in

$$\chi(\omega) = \frac{1}{2\pi i}\int_{-\infty}^{\infty} \frac{\chi(\omega')}{\omega' - \omega}d\omega'. \tag{2.39}$$

This can be further modified to give

$$\chi(\omega) = \frac{-i}{\pi}P\int_{-\infty}^{\infty} \frac{\chi(\omega')}{\omega' - \omega}d\omega' \tag{2.40}$$

which give us our final result: The Kramers-Krönig relations

$$\Re[\chi(\omega)] = \frac{1}{\pi}P\int_{-\infty}^{\infty} \frac{\Im[\chi(\omega')]}{\omega' - \omega}d\omega' \tag{2.41a}$$

$$\Im[\chi(\omega)] = \frac{-1}{\pi}P\int_{-\infty}^{\infty} \frac{\Re[\chi(\omega')]}{\omega' - \omega}d\omega'. \tag{2.41b}$$

This result shows that if the susceptibility is nonzero, then there must be an imaginary component to it as well as dispersion. Through Eq. 2.12, we see that this can be extended to the index of refraction; the index of refraction can have a positive or negative real part and not violate causality as long as there is a sufficient imaginary part and dispersion.

Eqs. 2.41b give the restrictions that prevent a material from responding to future fields. We can extend this result to show that the edge of the field cannot propagate

to another point in the material faster than c. The field at a particular position can be expressed as

$$E(x=0,t) = \frac{1}{\sqrt{2\pi}} \int_{-\infty}^{\infty} d\omega \mathcal{E}(\omega) e^{-i\omega t} \tag{2.42}$$

where

$$\mathcal{E}(\omega) = \frac{1}{\sqrt{2\pi}} \int_{-\infty}^{\infty} dt' E(x=0,t') e^{i\omega t'}. \tag{2.43}$$

For $t' < 0$, $E = 0$. We can use Eqs. 2.13 and 2.14 to see that the field at some other position will be

$$\begin{aligned} E(x,t) = \frac{1}{\sqrt{2\pi}} \int_{-\infty}^{\infty} d\omega \mathcal{E}(\omega) e^{ikx - i\omega t} &= \frac{1}{\sqrt{2\pi}} \int_{-\infty}^{\infty} d\omega \mathcal{E}(\omega) \exp\left[i\omega \left(\frac{n(\omega)}{c} x - t \right) \right] \\ &= \frac{1}{2\pi} \int_{-\infty}^{\infty} d\omega \int_{-\infty}^{\infty} dt' E(x=0,t') \exp\left[i\omega \left(\frac{n(\omega)}{c} x - (t-t') \right) \right]. \end{aligned} \tag{2.44}$$

Based on the relationship between the susceptibilities and index of refraction, we can make similar arguments for the index of refraction as we did for the susceptibilities and conclude that the index of refraction should be analytic in the upper-half plane. We can also assume that the resonances that cause the susceptibilities/index of refraction to deviate from their free space values occur at finite frequency. The exponent in Eq. 2.44 is then $i\omega(x/c - (t-t'))$ for large enough ω.

The ω integral in Eq. 2.44 can be done via contour integration. For $x/c > t - t'$, we must integrate around the upper-half plane. Since $n(\omega)$ is analytic in the upper-half plane, the integral will be zero. In addition, because $E(x=0,t'<0) = 0$, the t' integral can start at zero. Therefore, unless $t > x/c$, $x/c > t - t'$ for all t' where $E(x=0,t')$ is nonzero and $E(x,t) = 0$. This means that the signal cannot arrive faster than it would if traveling in free space, regardless of whether or not the index of refraction is less than

one or negative at a particular frequency.

2.2.2 Group Velocity

With the factor n^2/c^2, where n is the real part of the index of refraction, identified as the phase speed of a mode of the wave Eqs. 2.10, we see that the effect of the index of refraction is to modify the phase speed. However, the constitutive parameters, ϵ and μ, are frequency dependent and thus the index of refraction is frequency dependent. We can see the consequences of this by considering the propagation of a pulse through a medium with a frequency dependent index of refraction. If we take the pulse

$$a(x,t) = \frac{1}{\sqrt{2\pi}} \int_{-\infty}^{\infty} dk A(k) e^{i(kx-\omega t)} \tag{2.45}$$

and assume the pulse's bandwidth is narrow compared to its central frequency so that

$$\omega(k) = \omega_0 + (k-k_0)\frac{d\omega}{dk} \tag{2.46}$$

we can plug Eq. 2.46 into Eq. 2.45 to get

$$\begin{aligned} a(x,t) =& \frac{1}{\sqrt{2\pi}} \int_{-\infty}^{\infty} dk A(k) e^{i\left(kx-\omega_0 t - k\frac{d\omega}{dk}t + k_0\frac{d\omega}{dk}t\right)} \\ =& \frac{1}{\sqrt{2\pi}} e^{i\left(k\frac{d\omega}{dk}-\omega_0\right)t} \int_{-\infty}^{\infty} dk A(k) e^{ik\left(x-\frac{d\omega}{dk}t\right)} \\ =& a\left(x - \frac{d\omega}{dk}t, 0\right) e^{i\left(k\frac{d\omega}{dk}-\omega_0\right)t}. \end{aligned} \tag{2.47}$$

Eq. 2.47 shows us that this pulse propagates with a speed

$$v_g = \frac{d\omega}{dk} \tag{2.48}$$

known as the group velocity. If we were to include more terms in the Taylor series in Eq. 2.46 we would find what is known as the group velocity dispersion, along with higher

order terms that are important when working with ultra short pulses.

We use the dispersion relation, Eq. 2.14, to rewrite Eq. 2.48 in terms of the frequency derivative of the index of refraction.

$$\begin{aligned} v_g &= \frac{d}{dk}\frac{ck}{n(k)} = c\left(\frac{1}{n(k)} - \frac{k}{n^2(k)}\frac{dn}{dk}\right) \\ &= \frac{c}{n(k)} - \frac{\omega}{n(k)} v_g \frac{dn}{d\omega}. \end{aligned} \tag{2.49}$$

Solving for v_g we get

$$v_g = \frac{c}{n + \omega\frac{dn}{d\omega}}. \tag{2.50}$$

Eq. 2.50 shows us that we can manipulate the group velocity by manipulating the frequency dependence of the index of refraction. The larger the slope, the slower the light.

2.2.3 Imaginary Part Leads to Absorption

We have seen in the previous sections that the real part of the index of refraction leads to phenomenon associated with wave propagation. The imaginary part of the index of refraction plays the important role of absorption. The imaginary part is often called the absorption coefficient and is represented as α. If we put both the real and imaginary part of the index of refraction into the wave formula, we get

$$e^{\frac{2\pi i(n+i\alpha)}{\lambda}x} = e^{2\pi i\frac{nx}{\lambda}} e^{-2\pi\frac{\alpha x}{\lambda}}. \tag{2.51}$$

For passive materials, we can see from the above equation that the absorption coefficient must be positive. Otherwise the field amplitude would increase exponentially which is impossible for a passive material.

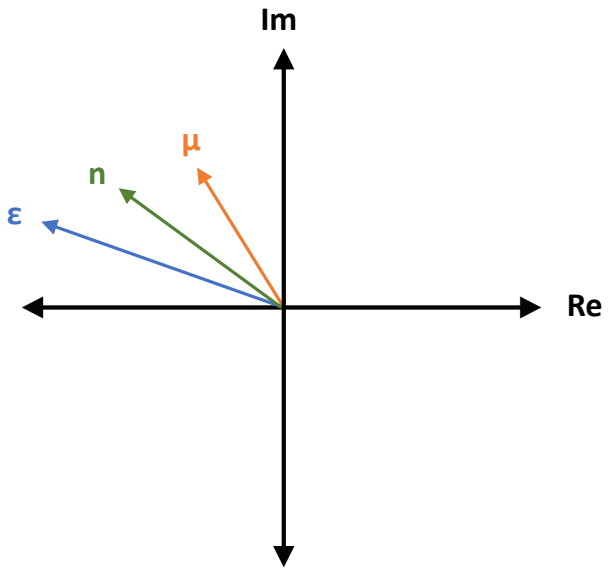

Figure 2.3: Complex valued ϵ, μ, and index of refraction, $n = \sqrt{\mu_r \epsilon_r}$. When the real part of the permeability and permittivity are negative and the imaginary parts are positive (as we would expect from a passive material), the real part of the index of refraction is negative.

2.3 What is a Negative Index of Refraction?

First thing's first. You might be looking at the definition of the index of refraction, $n = \sqrt{\epsilon_r \mu_r}$, and wondering how having a negative μ and ϵ requires us to take the negative branch of the square root when the radical still seems to be positive. What we have seen in the beginning of this chapter that if μ and ϵ differ from their free space value then they must be complex valued and their imaginary part must be positive. In the original papers about negative index, the material was considered to be lossless and therefore did not have an imaginary part. When we add the imaginary part in, we must specify that a negative index of refraction requires a negative **real** part of μ and ϵ. The way in which these requirements results in a negative (real part of the) index of refraction can be seen in Fig. 2.3. The square root in the definition of the index of refraction puts the index's phase angle between the phase angles of the permeability and permittivity. If

the permeability and permittivity have their phase angles in the second quadrant, then the index of refraction will also be in the second quandrant with a negative real part.

In 1968 Victor Vesalago [2] pointed out that, in principle, it was possible for a material to have a negative index of refraction. Although there are no naturally occurring materials with negative index and schemes for artificial materials had not yet been devised, Vesalago considered the consequences of a wave propagating with a negative index, and therefore a negative phase velocity.

There are many strange consequences of a negative index/negative phase velocity. Consider plugging the plane-wave solution Eq. 2.13 into the two Maxwell's Eqs. 2.7c and 2.7d. This would give us

$$\begin{aligned} \vec{k} \times \vec{E} &= \frac{\omega}{c} \mu \vec{H} \\ \vec{k} \times \vec{H} &= -\frac{\omega}{c} \epsilon \vec{E}. \end{aligned} \tag{2.52}$$

We can see from Eq. 2.52 that if ϵ and μ are positive, then $\vec{k}$, $\vec{E}$, and $\vec{H}$ for a right handed triad. However, in the negative index case with ϵ and μ negative, we get a left handed triad. If we then consider the triad formed between $\vec{E}$, $\vec{H}$, and the Poynting vector

$$\vec{S} = \vec{E} \times \vec{H} \tag{2.53}$$

we see that these vectors for a right handed triad no matter the sign of ϵ and μ. Therefore, in a negative index material, the vectors $\vec{k}$ and $\vec{S}$ are antiparallel.

In addition to negative phase velocity and antiparallel $\vec{k}$ and $\vec{S}$, a negative index material would also undergo a reversed Cerenkov effect, where the radiation cone is obtuse instead of acute, reverse Doppler effect, where emitters moving towards you are red shifted and those moving away are blue shifted, and a radiation tension, instead of radiation pressure.

There are also consequences of a negative on Snell's law. As it turns out, you can just

plug the negative index straight into Snell's law. The result will be a negative angle of refraction; the refracted beam remains on the same side of the normal as the incident beam. Fig. 2.4 shows how this works through the boundary conditions of Maxwell's equations, similar to Fig. 2.1.

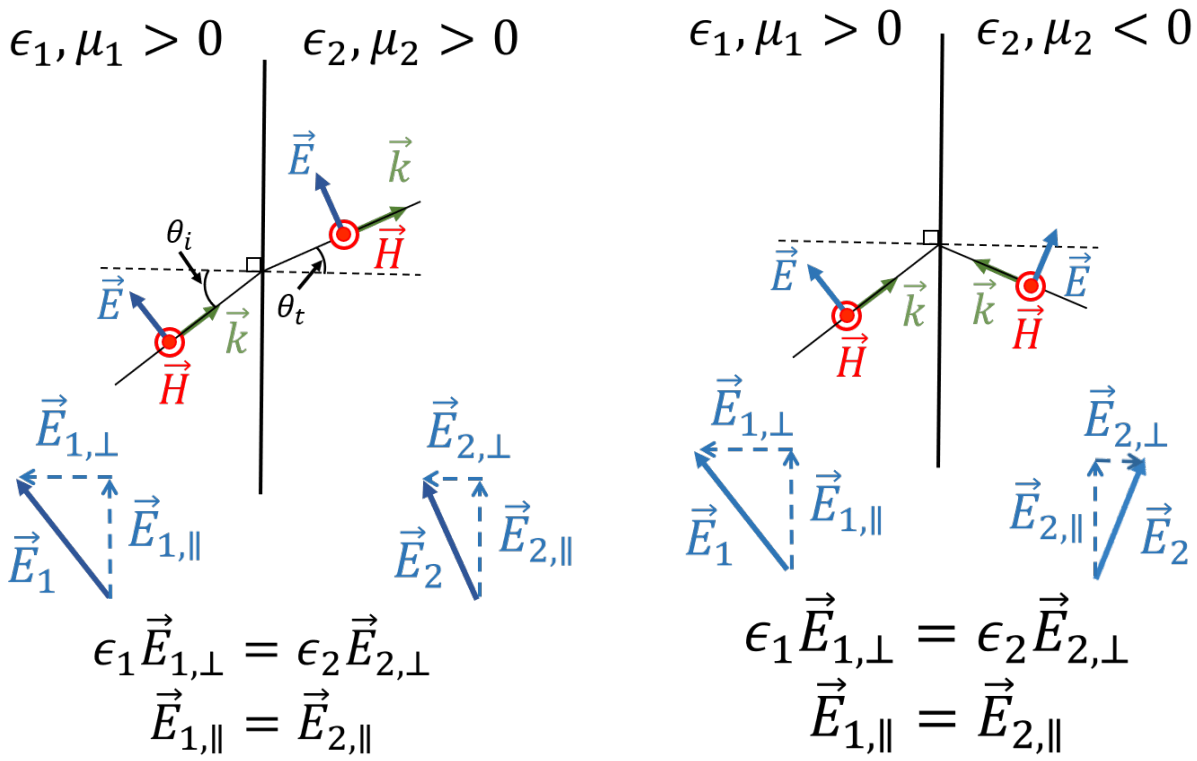

Figure 2.4: The field vectors and boundary conditions from Fig. 2.1 on the left. We can compare these to the right hand side which shows the field vectors and boundary conditions for a positive-negative index interface. The change in sign of the dielectric constant causes the direction of the perpendicular component of the electric field to switch direction. The result is that the beam refracts to the same side of the normal that the incident beam is on.

Vesalago considered the first implementations of these strange optical elements by noting that a lens could be made by using a slab of negative index material with flat, parallel interfaces with a positive index material, shown in Fig. 2.5.

Although Vesalago considered the possibility of a negative index lens in 1968, the

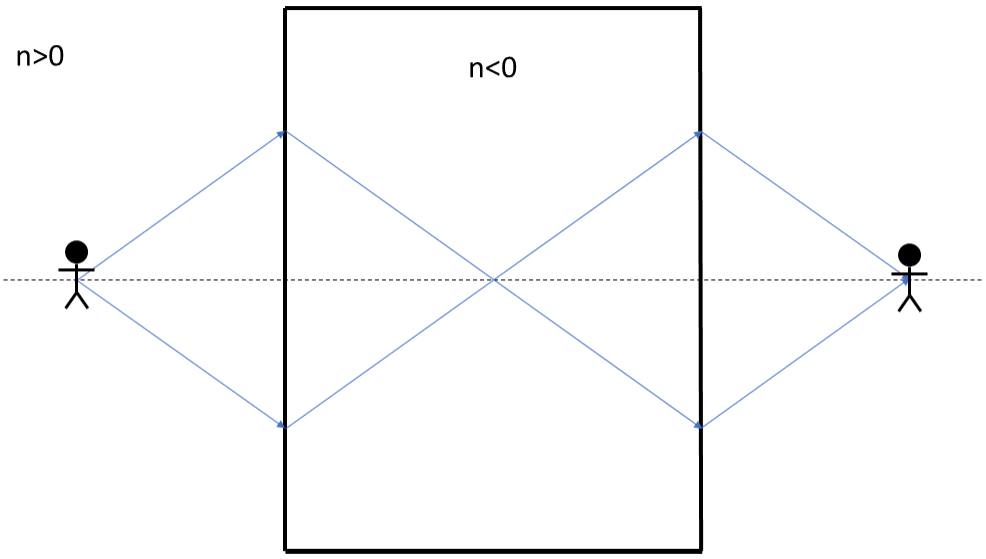

Figure 2.5: A lens made out of a rectangular slab of negative index material embedded in a positive index material. The change in sign of the refracted angle means that the image can be formed without the usual requirement of curved surfaces.

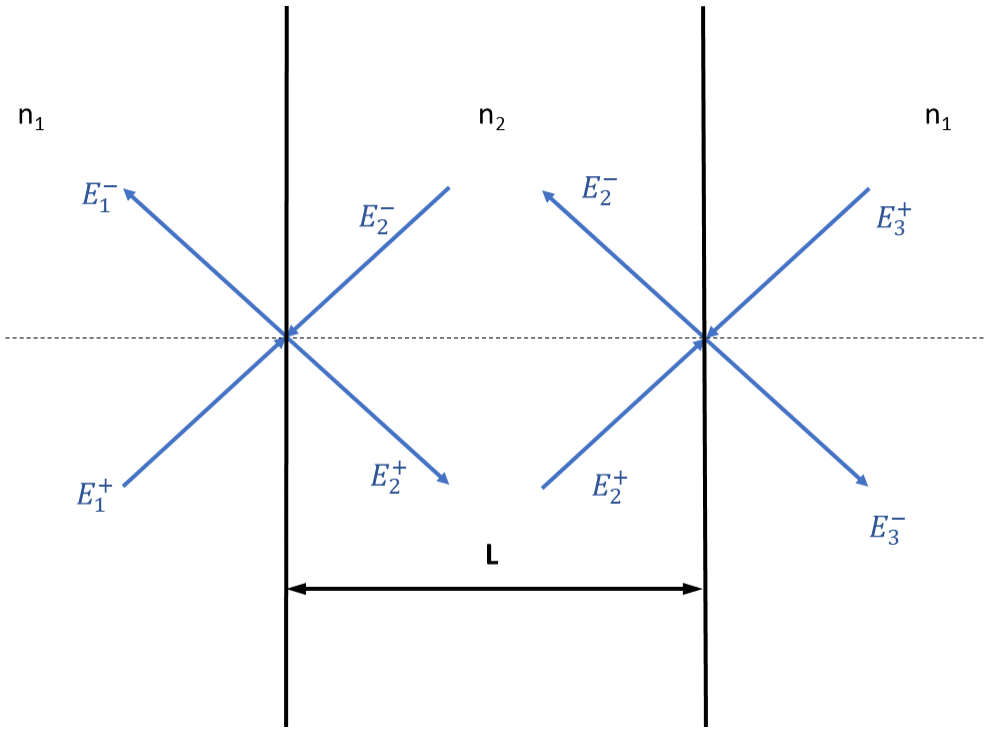

Figure 2.6: The fields and interfaces of a slab of length L with index of refraction equal to n_2 embedded in a material with index of refraction n_1.

subject did not attract much attention until 2000 when John Pendry pointed out that a slab with $n = 1$ could be used as a "perfect" lens [3], a lens that, in principle, has infinite resolution. The waves coming off subwavelength features of an object are evanescent waves; they have an exponential spatial decay. The ability of the perfect lens to resolve subwavelength features relies on the negative index slab's ability to amplify those evanescent waves [15, 16, 17].

Several authors took issue with Pendry's original paper [18, 19, 20] because he reaches his conclusion by calculating the reflection and transmission coefficients in a way that makes them appear to diverge. Although the issue was eventually sorted out [21, 22, 23] and the divergences turned out to not be an issue, I think it is easier to understand evanescent wave amplification by considering transfer matrices such as Eq. 2.26, the transfer matrix for a single interface.

We can see the divergences of the reflection and transmission coefficients derived

from Eq. 2.26. If we set $n = -1$, and therefore $\eta_2 = -1$, we see that the denominators of Eqs. 2.28 and 2.29 go to zero and the coefficients diverge. However, the transfer matrix that these coefficients are derived from does not have any divergences and is nonsingular. We can consider the transmission and reflection coefficients for a slab by using the well behaved matrix in Eq. 2.26 with the transfer matrix for propagation through the slab and the matrix for the second interface [24].

Consider system shown in Fig. 2.6. There we have a slab of thickness L with the same positive index material on either side. The transfer matrix for this system is given by

$$\mathbf{M} = \mathbf{M}_{12} \begin{pmatrix} e^{ik_z L} & 0 \\ 0 & e^{-ik_z L} \end{pmatrix} \mathbf{M}_{21} \tag{2.54}$$

where $\mathbf{M}_{12}$ is the transfer matrix from into the slab, $\mathbf{M}_{21}$ is the transfer matrix out of the slab, and k_z is the component of the k vector in the direction of the optical axis of the system. Note that we have not yet required the wave to be evanescent or that the slab have a negative index. If we carry out the matrix multiplication we get

$$\mathbf{M} = \begin{pmatrix} \cos(k_z L) + \frac{i}{2}\left(\frac{\eta_1 Z_1 \cos(\theta_{12,i})}{\eta_2 Z_2 \cos(\theta_{12,t})} + \frac{\eta_2 Z_2 \cos(\theta_{12,t})}{\eta_1 Z_1 \cos(\theta_{12,i})}\right)\sin(k_z L) & \frac{i}{2}\left(\frac{\eta_1 Z_1 \cos(\theta_{12,i})}{\eta_2 Z_2 \cos(\theta_{12,t})} - \frac{\eta_2 Z_2 \cos(\theta_{12,t})}{\eta_1 Z_1 \cos(\theta_{12,i})}\right)\sin(k_z L) \\ \frac{-i}{2}\left(\frac{\eta_1 Z_1 \cos(\theta_{12,i})}{\eta_2 Z_2 \cos(\theta_{12,t})} - \frac{\eta_2 Z_2 \cos(\theta_{12,t})}{\eta_1 Z_1 \cos(\theta_{12,i})}\right)\sin(k_z L) & \cos(k_z L) - \frac{i}{2}\left(\frac{\eta_1 Z_1 \cos(\theta_{12,i})}{\eta_2 Z_2 \cos(\theta_{12,t})} + \frac{\eta_2 Z_2 \cos(\theta_{12,t})}{\eta_1 Z_1 \cos(\theta_{12,i})}\right)\sin(k_z L) \end{pmatrix} \tag{2.55}$$

Setting $n = -1$ requires us to set $\eta_1 = \eta = -\eta_2$ and $Z_1 = Z_2 = Z$. Adding in the condition that the wave be evanescent means that $k_z = i\kappa$. Putting these together into Eq. 2.55 gives us

$$\mathbf{M} = \begin{pmatrix} \cos(i\kappa L) - i\sin(i\kappa L) & 0 \\ 0 & \cos(i\kappa L) + i\sin(i\kappa L) \end{pmatrix} = \begin{pmatrix} e^{\kappa L} & 0 \\ 0 & e^{-\kappa L} \end{pmatrix} \tag{2.56}$$

Eq. 2.56 can then be used to find the transmission coefficient

$$t = \frac{E_3^+}{E_1^+} = e^{\kappa L}. \tag{2.57}$$

The divergences and amplification can be interpreted in terms of a phenomenon called surface waves; waves that are confined to an interface and decay exponentially as you move away from the interface [25, 26, 27, 24][2]. The incident evanescent wave from the subwavelength scale object drive a surface wave resonance, causing the divergence of the reflection and transmission coefficients. The divergences are removed by adding the second interface because the resonances excited on each interface are couple and work together to produce the amplification in Eq. 2.57.

2.4 Approaches

Why aren't there negative index materials? It turns out that the electric susceptibility is orders of magnitude larger than the magnetic susceptibility at optical frequencies. Earlier we discussed how the susceptibility relates the field in the material to the polarization or magnetization. We can also relate the polarization and magnetization to the average dipole moment of the constituent atoms

$$P = \epsilon_0 \chi_E E = N\langle d \rangle; \qquad M = \frac{\chi_M}{\mu_0} B = N\langle \mu \rangle \tag{2.58}$$

where N is the atomic/ionic density, d is the electric dipole moment and μ is the magnetic dipole moment NOT the permeability. The notation is sort of confusing in this context, but μ is the symbol that is often used for the magnetic dipole moment in the

[2]Reference [24] uses a definition of surface waves that leads them to conclude that (what they define as) surface waves are not the cause of evanescent wave amplification. This differs from other authors [16] and seems to be purely a difference of terminology and not anything physical. Besides this confusing point, [24] is a very good reference

literature. We can use these relations to get the susceptibilities in the form

$$\chi_E = \frac{N\langle d\rangle}{\epsilon_0 E}; \qquad \chi_M = \frac{N\langle \mu\rangle \mu_0}{B} \tag{2.59}$$

The average of the dipole moments can be approximated by considering a typical magnitude for the dipole operators multiplied by the coherence between the states involved in the response, acquired from the density matrix. A typical value for the electric dipole moment is the electron charge times the Bohr radius, $d = ea_0$. For the magnetic dipole moment, we can use the Bohr magneton, μ_B. The coherence is itself proportional to the dipole moment, as well as the driving field. Putting these things together gives us

$$\langle d\rangle = ea_0\rho_{coherence} \sim (ea_0)^2 E; \qquad \langle \mu\rangle = \mu_B \rho_{coherence} \sim \mu_B^2 B. \tag{2.60}$$

Using Eqs. 2.59 and 2.60, we can find the ratio of the susceptibilities

$$\frac{\chi_E}{\chi_M} = \frac{\langle d\rangle}{\epsilon_0 E}\frac{B}{\mu_0\langle \mu\rangle} = \frac{(ea_0)^2 E}{\epsilon_0 E}\frac{B}{\mu_0 \mu_B^2 B} = \frac{1}{\alpha^2} \tag{2.61}$$

where α is the fine structure constant. Eq. 2.61 shows us that a typical electric response is 5 orders of magnitude larger than a typical magnetic response. Since the permeability of a material is typically assumed to be equal to the free space value, any implementation of a negative index material will require a substantial increase in the magnetic response. This is the main challenge in producing a negative index material.

2.4.1 Metamaterials

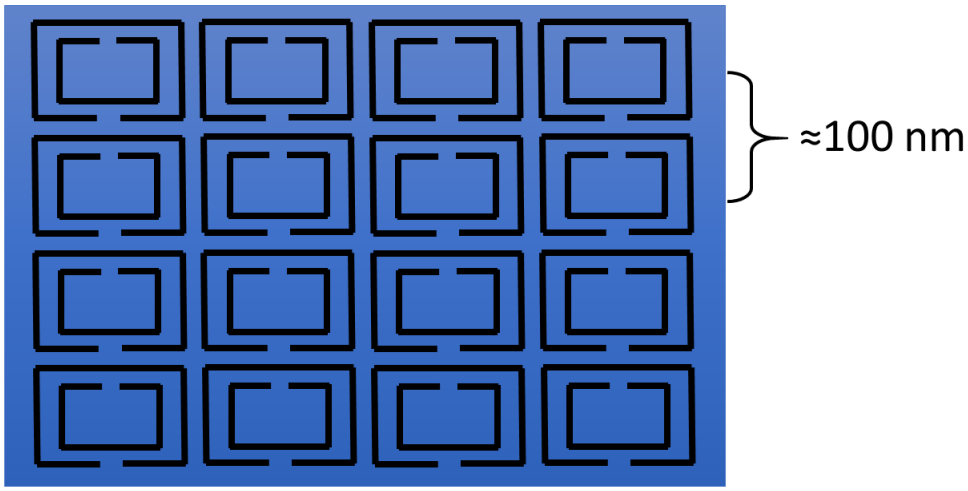

Figure 2.7: An example of a split-ring resonator metamaterial. The split rings have an inductance and capacitance giving them both a magnetic and electric response. This allows split-ring resonator metamaterials to have a negative index. Cutting edge metamaterials can create unit cell sizes on the scale of 100 nm. Fun aside: can you see the optical illusion in the figure?

A circuit can be engineered to have a large response to the magnetic field of a signal via its inductance. If we add in some capacitance, then we have a circuit that responds to both the electric and magnetic fields. If we were to then shrink this circuit down so that it was much smaller than the wavelength of the signal and create a large array of these circuits, then we would have an area of space with a large effective electric and magnetic response. This is the strategy that metamaterials have made use of in the pursuit of negative index materials.

An example of the canonical metamaterial geometry is shown in Fig. 2.7, called the split-ring resonator [28]. The loop structure gives the resonator its inductance and the gap gives it a capacitance, thus giving each unit cell an electric and magnetic response.

The responses can be engineered by changing the geometry of the unit cells: the gap size, loop size, wire thickness, etc. If the wavelength of the incident electromagnetic signal is much larger than the unit cells of the metamaterial, then the metamaterial will have an effective permittivity and permeability determined by the electric and magnetic responses of the unit cells. Although many metamaterials have been based on the split-ring resonator geometry, many other successful geometries have been developed as well [29, 30, 31].

The development of metamaterials has enjoyed great success. While the first metamaterials operated in the GHz range, modern metamaterials have pushed the boundaries of negative indices into the green range of the visible spectrum [32]. Despite these successes, metamaterials have several limitations. One is that as the metallic unit cell gets smaller, Ohmic losses increase, preventing the refracted light from penetrating too far into the material. There are also both practical and fundamental limitations to the maximum resonant frequency that a metamaterial can produce. From the practical viewpoint, the unit cell size, and thus the highest resonance frequency, can only be made so small. The cutting edge manufacturing techniques can produce unit cells on the order of 100 nm [33]. In addition to limiting the wavelengths at which a negative index occurs, the unit cell size also puts a limit on performance of certain applications such as the perfect lens; a perfect lens will not be able to resolve features smaller than the unit cell size [15, 16]. In addition, as the resonance frequency of the unit cells is pushed higher and higher, the resonance saturates [31]; the bandwidth decreases while the imaginary part of the index of refraction increases. This saturation leads to another limit on the frequency at which a negative index can be achieved based on the metamaterial geometry and the plasma frequency of the metal that it is constructed from.

The main goal that the work in this thesis is aimed at is producing an "atomic" metamaterial, an atomic crystal, such as a rare-earth doped crystal, in which the electric and magnetic responses have been manipulated in order to produce a negative index. Atomic

metamaterials have the potential to overcome the limitations of traditional metamaterials discussed above. Quantum interference techniques can be used to limit the absorption of an atomic system. In addition, the unit cell size is set by the unit cell of the crystal, typically on the order of 1 nm, allowing for negative indices to be observed at much higher frequencies than traditional metamaterials.

2.4.2 Atomic Approach: External Polarization and Magnetization

One of the important properties of a negative index material is that $\vec{k}$, $\vec{E}$, and $\vec{H}$ for a left-handed triad. We can produce these left-handed waves by forcing the vectors to for the left-handed triad by driving the polarization and magnetization of the system [34]. If we take a "normal" right-handed material and induce a polarization and magnetization in it we get

$$\vec{k} \times \vec{E} = \mu_0 \omega (\vec{H} + \vec{M}_{ext}) \tag{2.62}$$

$$\vec{k} \times \vec{H} = -\omega (\epsilon_0 \vec{E} + \vec{P}_{ext}) \tag{2.63}$$

where $\vec{M}_{ext} = -2\vec{H}$ and $\vec{P}_{ext} = -2\epsilon_0 \vec{E}$ are the magnetization and polarization that are driven by external sources. With these we get

$$\vec{k} \times \vec{E} = -\mu_0 \omega \vec{H} \tag{2.64}$$

$$\vec{k} \times \vec{H} = \epsilon \omega \vec{E} \tag{2.65}$$

which are the relations that give us a left-handed triad.

Since the challenge is to induce a magnetization, we want to know what polarization we would need to induce for whatever magnetization we are capable of producing. Consider a material with a very small magnetic, but nonzero so we can still induce some magnetization, response so that $\mu \approx \mu_0$. The ratio of the externally driven polarization

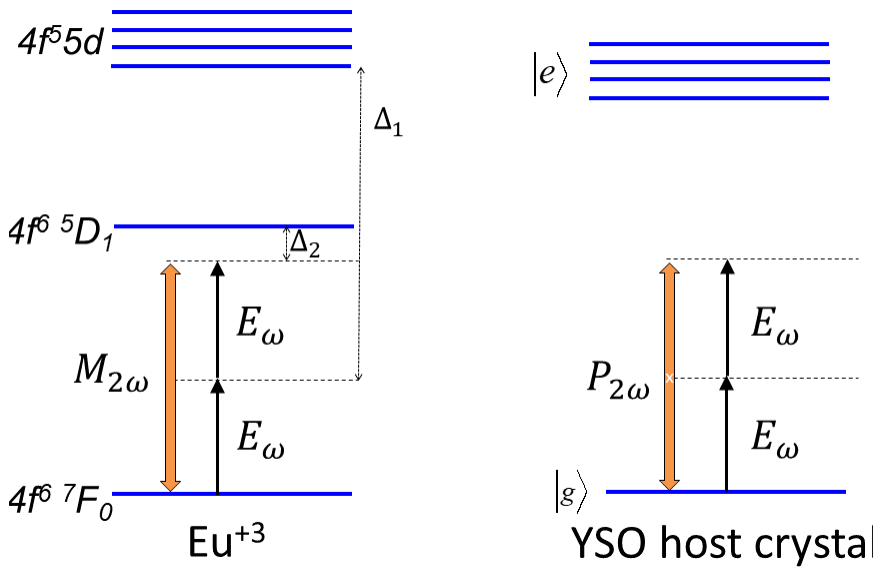

Figure 2.8: Left handed scheme in Eu. On the left is the level scheme to induce the magnetic response in the europium ions. This scheme would use the levels from our experiments in chapters 5 and 6. The right hand side shows our scheme to induce the necessary electric response. This response comes from the second order electric response of the host crystal. Taken from [34].

to the externally driven magnetization is then

$$\frac{|\vec{P}_{ext}|}{|\vec{M}_{ext}|} = \frac{n^2+1}{2cn}. \tag{2.66}$$

This externally driven scheme can be implemented in the way shown in Fig. 2.8 using the crystal that the experiments in this thesis were carried out in, europium doped yttrium orthosilicate (Eu:YSO). This scheme uses the 527 nm magnetic dipole $^7F_0 \rightarrow ^5D_1$ transition in the europium ions as the source of the magnetic response. The electric response would come from the bulk response of the host crystal. The scheme in Fig. 2.8 uses second order processes where 1055.5 nm light us used to externally polarize and magnetize the crystal, which in turn generates the 527 nm left-handed light.

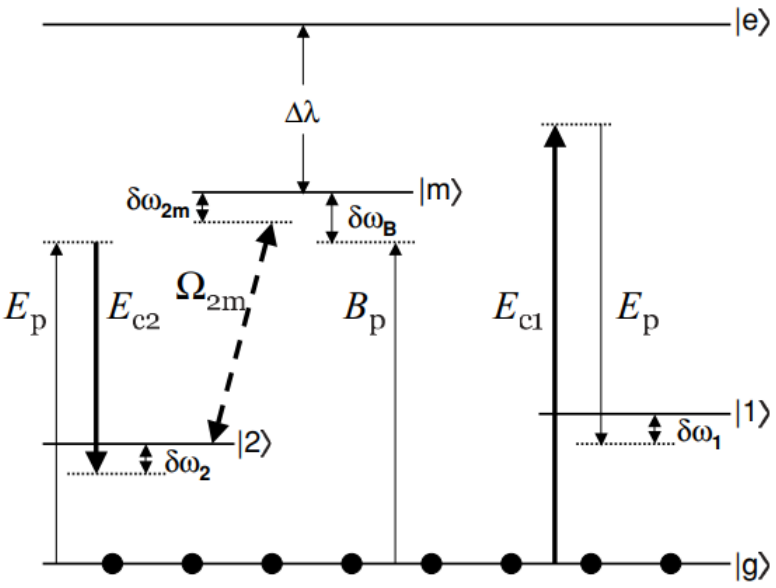

Figure 2.9: Energy level diagram of the chirality scheme. Because strong magnetic responses are hard to come by all on their own, it would be even harder to find a magnetic and electric response at the same frequency and of comparable strength. Therefore this scheme engineers an electric response via Raman transitions. The two Raman transitions, involving E_{c1} and E_{c2} produce an electric response with low absorption at the desired frequency. The magnetic response is derived from a two level transition that is enhanced by the crosscoupling beam Ω_{2m}. Taken from [35].

2.4.3 Atomic Approach: Chirality

Another possible scheme for a negative index atomic metamaterial is shown in Fig. 2.9 [35, 36, 37]. This scheme differs from the externally driven scheme in that the extra laser beams are used to set up a coherent state in the system that will then respond with a negative index when another beam is sent in.

At the center of this scheme is something called magneto-electric crosscoupling, or chirality [38, 39]. This means that instead of the polarization being purely induced by the electric field and the magnetization being produced solely by the magnetic field, the magnetic field can induce a polarization and the electric field can produce a magnetiza-

tion. In this way the magnetic response can be enhanced by the electric response. This is accomplished through the beam labeled Ω_{2m} in Fig. 2.9 which couples the magnetic transition $|g\rangle \rightarrow |m\rangle$ to the electric transition $|g\rangle \rightarrow |2\rangle$. A former student on this project, Dan Sikes, ran simulations for this scheme to find the how the index of refraction varied with frequency. Plots of the real and imaginary parts of the index of refraction versus frequency can be found in Fig. 2.10. Details of this scheme can be found in Dan's thesis [37].

Another important aspect of this scheme is that it contains an electric response that has been engineered to be at the same frequency as the magnetic response. This is accomplished by the two Raman transitions involving the beams E_{c1} and E_{c2}. The reason for having two Raman transitions is that one is absorptive, the one involving E_{c2}, and one is amplifying, the one involving $Ec1$. Having an absorptive and amplifying Raman transition gives control over the overall absorption in the system, and the fact that these are Raman transitions gives control over the frequency of the response [40, 41].

A drawback of this scheme is that it requires a larger magnetic dipole moment for the $|g\rangle \rightarrow |m\rangle$ transition than the externally driven scheme requires for left-handed waves. The possibility of implementing this scheme in terbium is explored towards the end of this thesis.

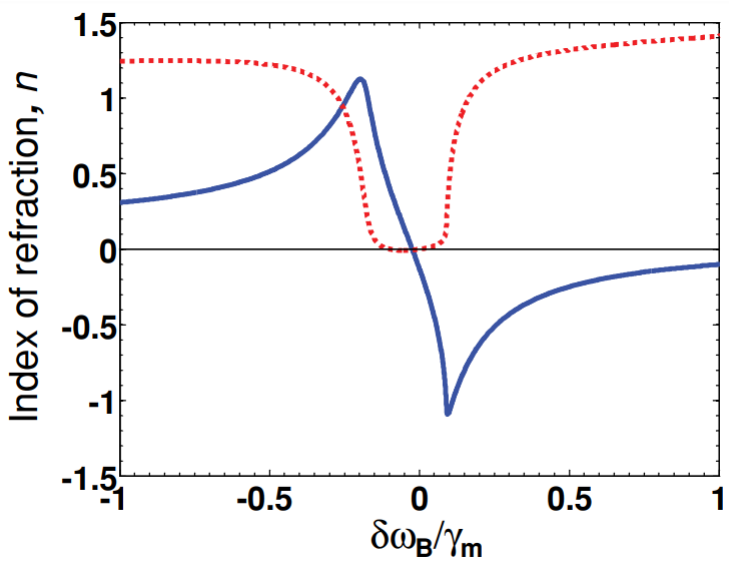

Figure 2.10: The real (blue, solid) and imaginary (red, dashed) parts of the index of refraction for an idealized atomic system using the chirality scheme shown in Fig. 2.9. Taken from Dan Sikes's thesis [37].

Chapter 3

Crystal Field Theory

Originally, I had planned to use this chapter as a place to go into some detail about the free ion Hamiltonian and how to construct its eigenstates, before talking about the effects of the crystal field. This was something that I thought would be useful for future students working on this project, particularly when trying to use the free ion states to calculate the effects of the crystal field. However, it was not clear to me how to start talking about this topic without the discussion going on for pages and pages and that it would be best to leave the details to the references[1]. There are many references on the subject [42, 43, 44, 45]. My goal here is to give a brief overview of the general properties of free ions that will hopefully give future students some direction when diving into the literature and be useful when considering the effects of the crystal field.

3.1 Free Ions

There are different ways to formulate the theory of the free ion. However, modern models are typically based on the work done by Racah in the 1940's [46, 47, 48, 49], where he formulated things in terms of group theory. This formulation greatly "simplified" the calculations and made it possible to analytically study multi-electron ions, such as rare

[1] "Really Zach, after that last chapter?"

H_1	Coulomb interaction
H_2	Spin-orbit interaction
H_3	Crystal interaction
H_4	External magnetic fields
H_5	Magnetic hyperfine interactions
H_6	Higher order magnetic terms

Table 3.1: Typical interactions included in the ionic Hamiltonian.

earth ions.

That being said, there are still a couple of ways that the Hamiltonian for a free ion is presented. The one that I think is easiest to understand is the one discussed by Judd [43]. The Hamiltonian that Judd uses includes many of the finer scale interactions and is written as

$$H = H_1 + H_2 + (H_3) + H_4 + H_5 + H_6. \tag{3.1}$$

The typical magnitude of the terms in the above equation decreases as you move to the right. These terms are described in Tab. 3.1. The crystal field term has been included in parenthesis as a reminder that we are currently considering free ions and to place its typical magnitude between the spin-orbit and hyperfine terms. Almost all of the contributions to the energy levels and transition strengths of the free ions come from the first two terms of Eq. 3.1 and will be the focus of this section.

The full form of the Coulomb Hamiltonian is

$$H_1 = -\sum_i \left[\frac{\hbar}{2m_e}\nabla_i + \frac{Ze^2}{r_i}\right] + \sum_{i<j}\frac{e^2}{r_{ij}}. \tag{3.2}$$

This Hamiltonian is generally handled by making the central field approximation (CFA). In the CFA, H_1 is written in terms of the nuclear Coulomb potential and another central field constructed for each electron by averaging over the position of all the other electrons. The noncentral part of H_1, the interactions between electrons, is then added as a

perturbation. The central part of the Hamiltonian is

$$H_{cent} = \sum_i \left[\frac{\hbar^2}{2m_e} \nabla_i + \frac{Ze^2}{r_i} + U(r_i) \right] \tag{3.3}$$

and the perturbing, noncentral part is

$$V_1 = H_1 - H_{cent} = \sum_{i<j} \left[\frac{e^2}{r_{ij}} - U(r_i) \right] \tag{3.4}$$

where the sums are over all the electrons in the ion.

The central potential $U(r)$ can be constructed through self-consistent field methods [42] and is done numerically. The electron interaction term, however, can be quite cumbersome to do numerically. This is where the group theory and other formulations come in. The $1/r_{ij}$ term can be expanded into spherical harmonics using the spherical harmonic addition theorem

$$\frac{1}{r_{ij}} = \sum_k \frac{r_<^k}{r_>^{k+1}} P_k(\cos(w)) \tag{3.5}$$

$$= \sum_k \frac{r_<^k}{r_>^{k+1}} \sum_{q=-k}^{k} (-1)^q C_{-q}^{(k)}(\theta_i, \phi_i) C_q^{(k)}(\theta_j, \phi_j) \tag{3.6}$$

$$= \sum_k \frac{r_<^k}{r_>^{k+1}} \sum_{q=-k}^{k} (-1)^q (C_{-q}^{(k)})_i (C_q^{(k)})_j. \tag{3.7}$$

The operators in this formula are single electron operators. The electron states in real atoms, though, are often multi electron states, such as the $4f$ states in europium ions. In order to compute the matrix elements of the operator in Eq. 3.5, we must break up these multi electron states into their single electron pieces. This is one place where group theory comes in. Using group theory, Eq. 3.5 can be broken up into two electron interaction terms, three electron interaction terms, and so on [43, 42].

The Hamiltonian for spin orbit coupling is

$$H_2 = \sum_{i=1}^{N} \frac{\hbar^2}{2m^2c^2r_i}\frac{dU(r_i)}{dr_i}\vec{s}_i \cdot \vec{l}_i = \sum_{i=1}^{N} \xi(r_i)\vec{s}_i \cdot \vec{l}_i. \tag{3.8}$$

Similar to the Coulomb interaction, the operators in Eq. 3.8 are single electron operators. Also similar to the Coulomb interaction, we can use operator techniques to evaluate the dot product term, which is the angular part of the problem. The radial part is parameterized for each configuration as

$$\zeta_{nl} = \int_0^\infty R_{nl}^2 \xi r dr \tag{3.9}$$

where R_{nl} is the radial part of the wavefunction for a particular configuration.

H_1 and H_2 are the interactions used by Robert Cowan's code [42], the atomic structure code we used to calculate wave functions and energies for our europium ions. The resulting eigenstates are states of definite total J and parity. These states then have the expected selection rules $\Delta J = 0, \pm 1$ except for $J = 0 \rightarrow J = 0$, transitions between configurations, $4f^6 \rightarrow 4f^5 5d^1$ in europium ions, are electric dipole transitions, and transitions within a configuration, $4f^6 \rightarrow 4f^6$ for europium ions, are magnetic dipole or electric quadrupole transitions.

The eigenstates of a free ion are generally not pure LS states. However, the lanthanides are still fairly close to the LS coupling regime, and there is typically one LS state that is a dominant component of the free ion state. The free ion state is labeled by this dominant component. For example, the $^7\mathrm{F}_0$ ground state of our europium ions is not a state with $L = 3$ and $S = 3$, but is instead

$$^7F_0 = 0.968|^7F_0\rangle + 0.0016|^5D_0\rangle + 0.1659|^5D_0'\rangle - 0.1815|^5D_0''\rangle \tag{3.10}$$

where the states on the right are pure LS states. The above decomposition was calculated

by Ofelt [1] by hand. The states outputed by Cowan's code have many more components, but those given in Eq. 3.10 and Ofelt's paper have the vast majority of the contributions.

Another thing to note about Eq. 3.10 is that there are three pure LS states labeled $|^5D_0\rangle$. Each of these pure LS states is still a combination of six single electrons. When the six-electron states are constructed from the single electron states, we want the final six-electron state should be an eigenstate of the J operator and antisymmetric under exchange of any two of the six electrons. As it turns out, there can be several ways to combine the six single-electron to get the same six-electron LS state. To distinguish between these different combinations, we introduce a new quantum number called the seniority number. The three $|^5D_0\rangle$ states each have a different seniority number denoted by $'$.

3.2 Crystal Fields

The crystal field is handled by expanding the potential experienced by the ion's electrons due to the surrounding crystal charge distribution into spherical harmonics. The potential

$$V = -\sum_{i}^{N} \frac{e_i \rho(\vec{R})}{|\vec{R} - \vec{r_i}|} d\tau, \tag{3.11}$$

where i is the label for the electrons in the ion and $\rho(\vec{R})$ is the crystal charge density at location $\vec{R}$ from the center of the ion, becomes

$$V = \sum_{i}^{N} \sum_{k} \sum_{q=-k}^{k} B_q^k C_q^{(k)}(\theta_i, \phi_i) \tag{3.12}$$

where

$$B_q^k = -e \int (-1)^q \rho(\vec{R}) C_{-q}^k(\theta, \phi) \frac{r_<^k}{r_>^{k+1}} d\tau. \tag{3.13}$$

[50, 51, 43, 44]. Another common formulation of the crystal field has the factor r^k in Eq. 3.13 separate from the definition of B_q^k and the field is parameterized as $A_q^k \langle r^k \rangle$ instead. Unfortunately, both B_q^k and A_q^k are referred to as crystal field parameters in the literature. The B_q^k and $A_q^k \langle r^k \rangle$ are related to each other by a constant numerical factor of the order 1-10. These relations can be found in [50].

Although the crystal field will perturb the energies of the states of the ions to some extent, the main effects we are interested in are the effects on transition strengths. Because the crystal reduces the spatial symmetry to that of the dopant cite, J is now technically not a good quantum number and there will be some amount of mixing of states with different J. As we will see later, this mixing can be used to explain discrepancies between our calculation of the dipole moment of the transition in our experiment and our measured value.

In addition, the crystal field is, in general, made up of even and odd components resulting in mixing of states with different parity. The result of this mixing is what are known as forced electric dipole transitions. These are transitions that are nominally between states of the same configuration, which we would expect to be magnetic and not electric, but the states have some small amount of another, opposite parity configuration mixed in allowing for the electric dipole nature of the transition.

3.3 Judd-Ofelt Theory

In this section is a derivation of the results of Judd-Ofelt theory [52, 53]. A lot of the sources in the literature don't have a lot of detail, so this explicit derivation will hopefully be useful for future students. The results, techniques, and formula are also relevant for

some of the effects we observe in our experiments.

The way the crystal field is often dealt with, and the way Judd and Ofelt dealt with it in their original formulation of Judd-Ofelt theory, is to split the field up into even and odd parity components

$$V_{crys} = V_{even} + V_{odd}. \tag{3.14}$$

Since the states of the free ion have definite parity, this splitting of the crystal field can be used to see which components of Eq. 3.12 are involved in different types of interactions. Although this is the original route of Judd and Ofelt, I took the route Wybourne [44] takes, which is to split the Hilbert space up into a single-configuration subspace and an ever-other-configuration subspace.

3.3.1 Introduction

Judd-Ofelt theory is an attempt to understand the presence of forbidden transitions in rare-earth doped crystals such as intraconfiguration electric dipole transitions. The theory does this by expanding the crystal perturbation into an even and an odd part. The even part mixes the free-ion energy levels within a configuration and the odd part mixes free-ion energy levels from different configurations. The intraconfiguration electric dipole transitions are caused by the odd part of the crystal field. Judd-Ofelt theory, as we will see, is a second order theory.

The rather audatious assumptions of Judd-Ofelt theory are:

1. All excited configuration states are degenerate

2. The energy separation between configurations is large compared to intraconfiguration levels. Therefore the wavefunction denominators from second order perturbation theory are equal.

These assumptions allow for a substantial simplification of transition strength calculations, as well as relatively easy to interpret results. Despite how drastic the assumptions might seem in some cases, Judd-Ofelt has enjoyed significant success in the 60 years since it was formulated [54, 55].

Much of this derivation is based on [44], however [55] is also a good reference ([42] is also chock-full of useful equations). In order to consider intra verses interconfiguration interactions, we will want to be able to split our Hilbert space up into two parts; one part is a single configuration, and the other part is all the other configurations. We begin by constructing the projection operators

$$P = \sum_n |g_n\rangle\langle g_n| \tag{3.15a}$$

$$Q = \sum_l |e_l\rangle\langle e_l| \tag{3.15b}$$

where $|g_n\rangle$ are the free-ion energy levels of the ground configuration and $|e_n\rangle$ are the free-ion energy levels of all the excited configurations. Together these give us

$$P \otimes I_Q + I_P \otimes Q = P + Q \tag{3.16}$$

where I_P and I_Q are identity operators with the same dimension as P and Q respectively and the last equality is for simplicity of notation.

We can use the operator in Eq. 3.16 with a perturbation, V, to get

$$(P+Q)V(P+Q) = PVP + QVQ + PVQ + QVP \tag{3.17}$$

where the first two terms on the right are intraconfiguration interactions and the second two are interconfiguration interactions. Judd-Ofelt theory is concerned with the second two terms.

3.3.2 Incorporating Double Perturbation Theory

There are two interactions to consider when working with Judd-Ofelt theory, the crystal perturbation and the transition inducing perturbation (laser beam). We will therefore have to make use of double perturbation theory. The second order transition matrix element between an initial state $|\psi_i^{(0)}\rangle$ and a final state $|\psi_f^{(0)}\rangle$ is given by

$$\sum_{m\neq i,k\neq f}\left[\frac{\langle\psi_f^{(0)}|D_\rho^{(1)}|\psi_m^{(0)}\rangle\langle\psi_m^{(0)}|V|\psi_i^{(0)}\rangle}{E_m^{(0)}-E_i^{(0)}}+\frac{\langle\psi_f^{(0)}|V|\psi_k^{(0)}\rangle\langle\psi_k^{(0)}|D_\rho^{(1)}|\psi_i^{(0)}\rangle}{E_k^{(0)}-E_f^{(0)}}\right]. \tag{3.18}$$

Now we replace V with the operator in Eq. 3.17. Since $D_\rho^{(0)}$ is odd for electric dipole transitions, we will only need to consider the interconfiguration parts of Eq. 3.17, giving us

$$\sum_l\left[\frac{\langle\psi_f^{(0)}|D_\rho^{(1)}|e_l\rangle\langle e_l|V|\psi_i^{(0)}\rangle}{E_l^{(0)}-E_i^{(0)}}+\frac{\langle\psi_l^{(0)}|V|e_l\rangle\langle e_l|D_\rho^{(1)}|\psi_i^{(0)}\rangle}{E_l^{(0)}-E_f^{(0)}}\right] \tag{3.19}$$

where, since $|\psi_f^{(0)}\rangle$ and $|\psi_i^{(0)}\rangle$ are in one configuration and $|e_l\rangle$ are in another, we do not have to worry about restricting the sum over l.

3.3.3 Incorporating the Judd-Ofelt Assumptions

When we incorporate the assumptions of Judd-Ofelt theory into Eq. 3.19, we can factor the denominators outside of the sum to get

$$\frac{1}{E_e-E_g}\sum_l\left[\langle\psi_f^{(0)}|D_\rho^{(1)}|e_l\rangle\langle e_l|V|\psi_i^{(0)}\rangle+\langle\psi_l^{(0)}|V|e_l\rangle\langle e_l|D_\rho^{(1)}|\psi_i^{(0)}\rangle\right] \tag{3.20}$$

Where E_e is the energy of the excited configuration and E_g is the energy of the ground configuration. We can now use the fact that the excited configurations form a complete basis of a subspace of the full Hilbert space and use the closure theorem to sum over the

excited states.The result is

$$\frac{\langle \psi_f^{(0)} | D_\rho^{(1)} V | \psi_i^{(0)} \rangle + \langle \psi_f^{(0)} | V D_\rho^{(1)} | \psi_i^{(0)} \rangle}{E_e - E_g} \tag{3.21}$$

3.3.4 Evaluating the Matrix Elements

The operators in Eq. 3.21 can both be expressed as tensor operators. Taking this view allows us to use the many useful identities that have been developed for evaluating such operators. We will make use of the identity for multiplying two tensor operators together

$$T_{q_1}^{(k_1)} W_{q_2}^{(k_2)} = \sum_{KQ} (-1)^{k_1 - k_2 - Q} [K]^{\frac{1}{2}} \begin{pmatrix} k_1 & k_2 & K \\ q_1 & q_2 & Q \end{pmatrix} \left[T^{(k_1)} \times W^{(k_2)} \right]_Q^{(K)} \tag{3.22}$$

where the T and W will eventually be replaced with the crystal field and dipole operator. We will also make use of the unit tensor operators. These operators are defined so that their reduced matrix element is 1 when certain selection rules are met and 0 otherwise, making them convenient for separating out specifics of an interaction and deriving general results. They are defined by

$$\langle n'' l'' || u^{(k)}(ll') || n''' l''' \rangle = \delta(n;, n'' l'') \delta(n' l', n''' l'''), \tag{3.23}$$

and an important property of theirs is

$$\left[u^{(k_1)}(4f, n'l') \times u^{(k_2)}(n'l', 4f) \right]_Q^{(K)} = (-1)^K [K]^{\frac{1}{2}} \begin{Bmatrix} k_2 & K & k_1 \\ f & l' & f \end{Bmatrix} u_Q^{(K)}(4f, 4f). \tag{3.24}$$

We can use Eqs. 3.15 and 3.17 to re-express the interconfigurational part of the crystal field perturbation,

$$V_{crys} = \sum_{k,q} B_q^k \sum_i r_i^k C_{q,i}^{(k)}, \tag{3.25}$$

as

$$QV_{crys}P = \sum_{kq} B_q^k \langle n'l'|r_i^k\rangle \langle l'||C^{(k)}||f\rangle u_{q,i}^{(k)}(n'l', 4f) \tag{3.26}$$

where i denotes one of the electrons in the potential, B_q^k are the crystal field parameters, and $\langle l'||C^{(k)}||f\rangle$ can be evaluated using

$$\langle \alpha l||C^{(k)}||\alpha' l'\rangle = \delta(\alpha,\alpha')(-1)^l[l,l']^{\frac{1}{2}} \begin{pmatrix} l & k & l' \\ 0 & 0 & 0 \end{pmatrix}. \tag{3.27}$$

The interconfigurational dipole moment operator becomes

$$PD_\rho^{(1)}Q = E\sum_i \langle 4f|r_i|n'l'\rangle \langle f||C^{(1)}||l'\rangle u_{\rho,i}^{(1)}(4f, n'l') \tag{3.28}$$

where E is the amplitude of the electric field. Combining Eqs. 3.26 and 3.28 gives us

$$D_\rho^{(1)}V_{crys} = \sum_{kq} B_q^k \sum_i \langle 4f|r_i|n'l'\rangle \langle n'l'|r_i^k|4f\rangle \langle f||C^{(1)}||l'\rangle \langle l'||C^{(k)}||f\rangle u_{\rho,i}^{(1)}(4f, n'l') u_{q,i}^{(k)}(n'l', 4f) \tag{3.29}$$

which, after applying Eqs. 3.22 and 3.24, becomes

$$\begin{aligned} D_\rho^{(1)} V_{crys} =& \sum_{kq} B_q^k \sum_i \langle 4f|r_i|n'l'\rangle \langle n'l'|r_i^k|4f\rangle \langle f||C^{(1)}||l'\rangle \langle l'||C^{(k)}||f\rangle \\ & \times \sum_{KQ} (-1)^{K+1-k-Q}[K] \begin{pmatrix} 1 & k & K \\ \rho & q & Q \end{pmatrix} \begin{Bmatrix} k & K & 1 \\ f & l' & f \end{Bmatrix} u_{Q,i}^K(4f,4f) \\ =& \sum_{kq} \sum_i \sum_{KQ} (-1)^{f+l'+K+1-k-Q}[f,l',K] \langle 4f|r_i|n'l'\rangle \langle n'l'|r_i^k|4f\rangle B_q^k \\ & \times \begin{pmatrix} f & 1 & l' \\ 0 & 0 & 0 \end{pmatrix} \begin{pmatrix} l' & k & f \\ 0 & 0 & 0 \end{pmatrix} \begin{pmatrix} 1 & k & K \\ \rho & q & Q \end{pmatrix} \begin{Bmatrix} k & K & 1 \\ f & l' & f \end{Bmatrix} u_{Q,i}^K(4f,4f). \end{aligned} \tag{3.30}$$

We can follow a similar procedure for the second term in the numerator of Eq. 3.21 to get

$$\begin{aligned} V_{crys} D_\rho^{(1)} =& \sum_{kq} \sum_i \sum_{KQ} (-1)^{f+l'+K+k-1-Q}[f,l',K] \langle 4f|r_i|n'l'\rangle \langle n'l'|r_i^k|4f\rangle B_q^k \\ & \times \begin{pmatrix} l' & 1 & f \\ 0 & 0 & 0 \end{pmatrix} \begin{pmatrix} f & k & l' \\ 0 & 0 & 0 \end{pmatrix} \begin{pmatrix} k & 1 & K \\ q & \rho & Q \end{pmatrix} \begin{Bmatrix} 1 & K & k \\ f & l' & f \end{Bmatrix} u_{Q,i}^K(4f,4f). \end{aligned} \tag{3.31}$$

We can then use the symmetry property of the 3-J symbols

$$\begin{pmatrix} j_1 & j_3 & j_2 \\ m_1 & m_3 & m_2 \end{pmatrix} = (-1)^{j_1+j_2+j_3} \begin{pmatrix} j_1 & j_2 & j_3 \\ m_1 & m_2 & m_3 \end{pmatrix} \tag{3.32}$$

and the fact that the 6-J symbols are symmetric under column interchange to rewrite Eq. 3.31 as

$$V_{crys}D_{\rho}^{(1)} = \sum_{kq}\sum_{i}\sum_{KQ}(-1)^{f+l'+K+1-k-Q}[f,l',K]\langle 4f|r_i|n'l'\rangle\langle n'l'|r_i^k|4f\rangle B_q^k \times (-1)^{2(f+l'+k+1)+K}\begin{pmatrix} f & 1 & l' \\ 0 & 0 & 0 \end{pmatrix}\begin{pmatrix} l' & k & f \\ 0 & 0 & 0 \end{pmatrix}\begin{pmatrix} 1 & k & K \\ \rho & q & Q \end{pmatrix}\begin{Bmatrix} k & K & 1 \\ f & l' & f \end{Bmatrix} u_{Q,i}^K(4f,4f). \tag{3.33}$$

We can now see that the only difference between Eqs. 3.30 and 3.33 is the phase factor $(-1)^{2(f+l'+k+1)+K}$. For the sum in Eq. 3.21 to be nonzero, K must be even. In addition, since we have already established that the interconfiguration interactions will only involve the odd components of the crystal field, k must be odd. Since $l' = 4$ and $f = 3$ for typical situations, the 3-J symbols further restrict the allowed values of K to less then 7, but since K must be even, the condition becomes $K \leq 6$.

One of the main results of Judd-Ofelt theory is to explain the existence of electric dipole transitions within a configuration. The operator in Eq. 3.33 is effectively a second order electric dipole operator. In addition, this operator can be written in terms of u_Q^K where K is 2, 4, or 6. This means that the selection rules for Judd-Ofelt electric dipole transitions requires $\Delta J \leq 6$, as opposed to the usual selection rule. For transitions involving states with $J = 0$, such as the $^7F_0 \rightarrow ^5D_1$ transition in europium ions, this selection rule is restricted to ΔJ =2, 4, or 6.

Chapter 4

Eu:YSO

The index of refraction depends on the density of resonantors and the linewidths of those resonators. In order to produce a negative index of refraction we need a high density, narrow linewidth, and both an electric and magnetic response. As we've discussed, strong magnetic transitions at optical frequencies are very rare. However, rare earth ions are known to have such transitions. The narrowest linewidths can be achieved with laser cooled atoms. However, despite their narrow linewidths, these vapors do not have a high enough density for our needs. In order to have densities high enough we need a solid. "But Zach," you might say, "how do you get narrow linewidths in a solid?" Fortunately for us, there is a special family of solids that not only have high densities, but also have linewidths not too far off from those achievable with atomic vapors: rare-earth doped crystals.

The rare earth metals are the lanthanide metals from the periodic table and have a partially filled $4f$ shell. Electrons in the $4f$ shell, or configuration, benefit us because their large angular momentum makes it possible for them to have strong magnetic transitions. Also, due to the large number of electrons that can occupy f configurations (14), some rare earths have thousands of transitions just within the $4f$ configuration [56]. Since all these transitions are between $n = 4$ and $l = f$ states, the electric response is

suppressed, making it all the more likely that one of those thousands of transitions will be a strong magnetic transition. In addition, due to the strong interaction between the electrons, many of these transitions within the $4f$ configuration are in the visible range, some even extending into the UV.

Although the $4f$ shell is the highest energy of the unexcited rare earths, some of the other configurations actually have larger spatial extents. An example of this can be seen in Fig. 4.1. The trends shown in Fig. 4.1 are typical of all the rare earths. When the rare earths are doped into a crystal they typically lose three electrons, one electron from the $4f$ shell and the two from the $6s$ shell. This still leaves the $5s$ and $5p$ shells laying beyond the $4f$ shell. The effect of this is that the $4f$ shell is shielded from much of the perturbation from the crystal and leaving the $4f$ configuration with exceptionally narrow transitions within the solid.

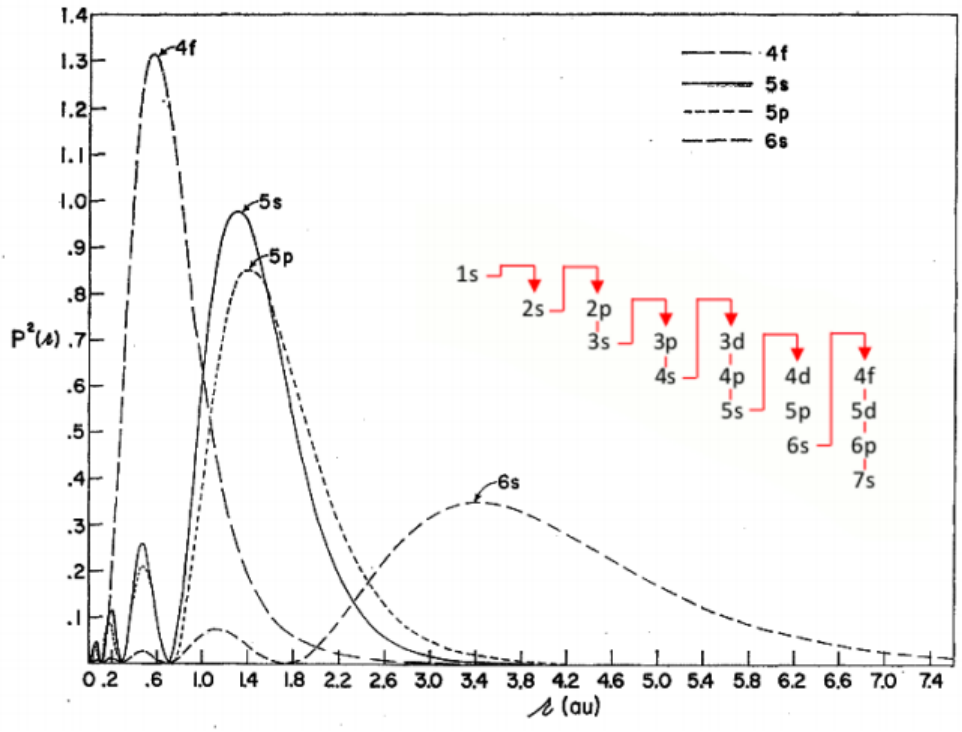

Figure 4.1: The radial charge density for Gd^{3+}. Although the scale for europium will be slightly different, the overall structure is the same. Reprinted figure with permission from [57] Copyright 1962 by the American Physical Society.

There are several reasons we chose the crystal Eu:YSO. We chose the dopant, Eu, because Zach Simmons, a previous student who worked on this project, used Cowan's code to identify a strong magnetic dipole transition from the ground state in the optical region, 527.5 nm. Although there are other rare earths with strong magnetic dipole transitions from the ground state, Eu:YSO had the advantage of already having been studied. While we were working on the Rabi flopping experiment, another group showed that the transition we were using was indeed a magnetic dipole transition [58], although they used a different host crystal. The crystal we are using, YSO, has drawn interest for quantum memory applications on a 580 nm forced electric dipole transition. Due to the reasons discussed above, this quantum memory transition has an extremely narrow linewidth and long coherence time. In addition, there had already been a study done on

the transition we are interested in, although they did not explore the magnetic nature of the transition.

In addition to these principle reasons, Eu:YSO has additional benefits. One is that replacing the Y with Eu produces only a small perturbation on the host crystal. Also, the crystal produces very small magnetic effects. ^{89}Y has a nuclear spin of 1/2 and a small nuclear magnetic moment of $\mu = -0.137\mu_N$. The magnetic isotope of Si has a small abundance, 4.7%, nuclear spin 1/2, and small nuclear moment of $\mu = -0.555\mu_N$. Oxygen has a negligible abundance of magnetic isotopes [59]. The lack of magnetic nature of the host crystal means that there should be even less perturbation from the crystal on our transition.

4.1 YSO Properties

4.1.1 General Properties

Another important property is the symmetry of the crystal. It's crystal symmetry is described by the monoclinic space group C_{2h}^6 [60]. The symmetry of the overall host is important to know because it will limit us in our ability to polarize the crystal. Monoclinic crystals do not have inversion symmetry and therefore cannot be used for SHG, at least not without any tricks. When we dope the YSO with Eu, the Eu replaces the Y. There are two inequivalent sites that the Eu can replace the Y, each with symmetry C_1 (i.e. no symmetry). This lack of symmetry is important because it means that there will basically be no degeneracy in the Eu's energy levels. It will also produce an anisotropic response when interacting with our laser [45].

Another important property of the two sites that we need to consider is their inequivalency. We will call the sites "site 1" and "site 2". The literature is not consistant as to which site is called site 1 and which is called 2. The convention that we use is followed by [61], [62], and [63], and the opposite labeling is used by [59] and [64]. It is

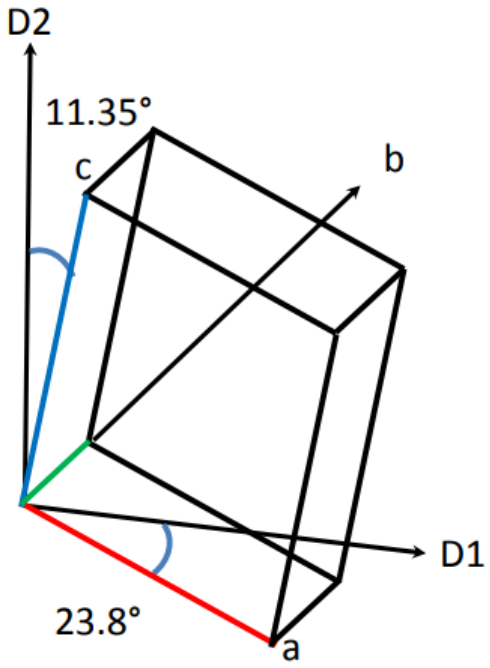

Figure 4.2: The crystallographic and optical axes of YSO. Image taken from [45].

important to be aware of this distinction and which labeling convention is being used. The inequivalency arises due to the different coordination number of the Eu ions (the number of oxygen atoms that they interact with). The coordination number of site 1 is 6 while the coordination number of site 2 is 7 [45].

The lattice parameters are reported in [60]. They are $a = 12.50$Å, $b = 6.72$Å, and $c = 10.42$Å. The angle between a and c is $\beta = 102.68°$and b is normal to both a and c. The optical axes are not completely aligned with the crystalographic axes. The c axis is 11.35°from $D2$ axis and the a axis is 23.8°from the $D1$ axis, both angles are in the same direction. The b crystalographic axis is in the same directions as the b optical axis.

4.1.2 Optical Properties

As previously mentioned, there are three distinct optical axes. These are summarized in Tab. 4.1. An important note is that the quantization axis of the Eu^{3+} ions is aligned with

Optical Axis	Principle Index	Orientation	Our Crystal
b	n_x	$\parallel \langle 010 \rangle$	10 mm
D_1	n_y	$\perp \langle 010 \rangle$	5 mm
D_2	n_z	$\perp \langle 010 \rangle$	4 mm

Table 4.1: The correspondence between the optical axes and our crystal was reported in our order quote from Scientific Materials Corp. The orientation and identity of the b axis as the n_x axis was reported in [65]. The correspondence between the D_1 and D_2 axes and the n_y and n_z axes was reported in the Scientific Materials data sheet, but it has been difficult to verify this elsewhere.

the D_2 axis.

Beach [65] also reported the Sellmeier coefficients for YSO for wavelengths between 435.8 nm - 643.8 nm. They used an Abbe refractometer and fit the data to the form

$$n^2 = A + \frac{B}{\lambda^2 + C} + D\lambda^2$$

where λ is in μm. The results of this experiment are reproduced in Tab. 4.2.

	A	B	C	D
n_x	3.0895	0.0334	0.0043	0.0199
n_y	3.1173	0.0283	-0.0133	0.00
n_z	3.1871	0.03022	-0.0138	0.00

Table 4.2: The results of the Sellmeier measurements found in Beach [65]

4.2 Eu Properties

4.2.1 The Free Ion

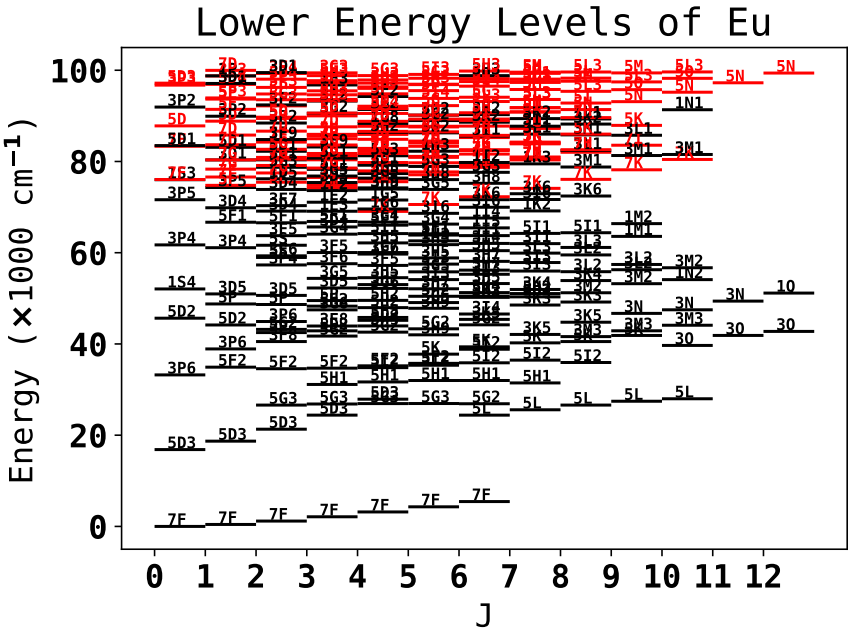

Figure 4.3: The lowest electronic energy levels of free Eu^{3+} calculated with Cowan's code. The black levels are from the lowest configuration, $4f^6$, and the red levels are from the first excited configuration, $4f^5\ 5d^1$

The $4f^6$ shell of the europium ion has thousands of energy levels. Specifically, since Eu^{+3} has six electrons in the fourteen available $4f$ states, there are $\binom{14}{6} = 3003$ states just within the $4f$ configuration. Many of these states, along with some from the $4f^5 5d^1$ configuration, can be seen in Fig. 4.3.

The highest energy states of the $4f^6$ configuration extend well into the UV. However, we are concerned with the very lowest few energy levels, shown in Fig. 4.4. The transition we are interested is the ${}^7F_0 \rightarrow {}^5D_1$ transition at 527 nm. The transition ${}^7F_0 \rightarrow {}^5D_0$ at 580 nm has drawn a lot of attention for quantum memory applications.

Europium occurs in two stable isotopes, one with atomic weight 151 and another

at 153. These isotopes also differ in their nuclear magnetic dipole moment and electric quadrupole moment which are summarized in Tab. 4.3. The experiments discussed later in this thesis involve the hyperfine structure of europium. The hyperfine splitting, when doped into the crystal is dominated by the quadrupole interaction leading to the 153 isotope to have larger hyperfine splittings [66].

	^{151}Eu	^{153}Eu
Nuclear Magnetic Dipole Moment (μ_N)	3.47	1.53
Nuclear Quadrupole Moment (fm^2)	90.3	241.2

Table 4.3: The nuclear magnetic dipole moment and quadrupole moment of the Eu isotopes [67].

4.2.2 In YSO

Although the $4f$ shell is largely shielded from the crystal field by the $5s$ and $5p$ electrons, the crystal field does still affect the $4f$ energy levels; in many cases these effects are critical to understanding the behavior of the system. Although the overall symmetry of the crystal is C_{2h}^6, the symmetry of the dopant sites is C_1 [68]. With such a low symmetry, all crystal field coefficients with $k \leq 6$ are expected to be nonzero which will have important consequences for transition strengths.

Linewidths and Decay

In the free ion, Cowan's code calculates the decay rate of the $^5D_1$ state to be less than 10 Hz and it decays directly to the ^7F manifold. The picture in the crystal is very different,

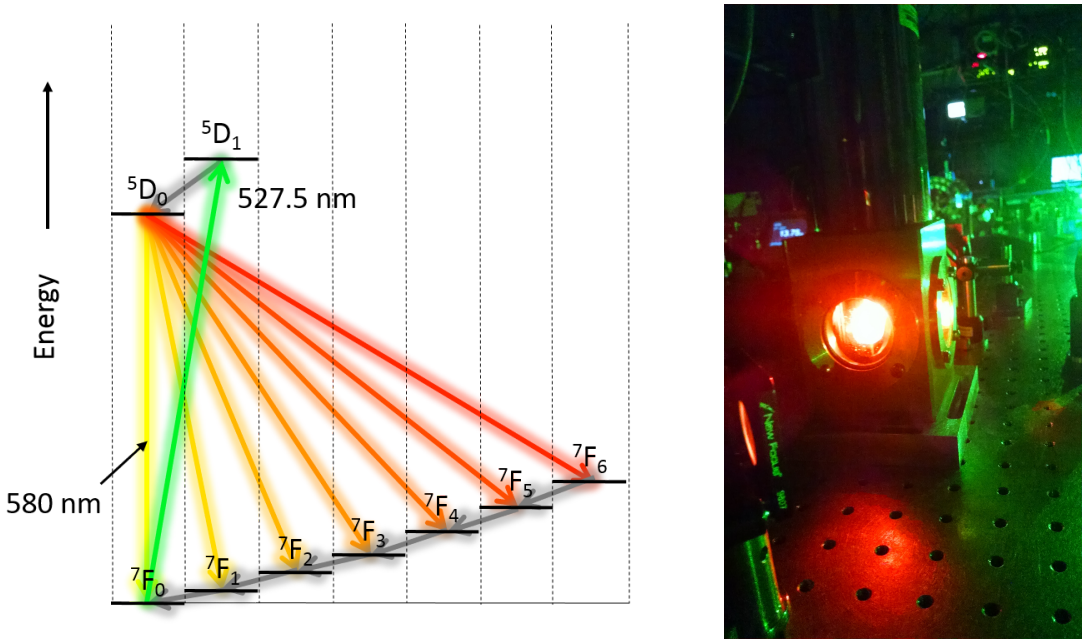

Figure 4.4: On the left are the electronic energy levels of Eu^{3+} and their decay channels that are relevant to our experiment. The green arrow represents the exciting beam, the dark gray arrows represent nonradiative decay, and the yellow to red arrows represent radiative decay. On the right is the actual green beam and fluorescence from our crystal.

and the decay mechanism are depicted in Fig. 4.4. The crystal opens up a new, phonon-mediated, non-radiative, decay channel from the $^5D_1$ state down to the $^5D_0$ state. The $^5D_0$ state then decays radiatively down to the ^7F manifold. The ions are return to the ground $^7F_0$ state from the other ^7F states through some more non-radiative transitions. These decay mechanisms result in bright orange fluorescence when our crystal is excited with a green, 527 nm, beam, shown on the right of Fig. 4.4. Previous students in the Yavuz group, Nick Brewer and Zach Simmons, measured the decay rates in this decay channel through fluorescence spectroscopy [45, 69]. They did this by sending in a short green pulse and monitoring the time dependence of the fluorescence. The results are shown on the left side of Fig. 4.5. The increase in fluorescence is due to the decay from $^5D_1$ to $^5D_0$. The decrease in decay occurs as the $^5D_0$ state empties out into the ^7F manifold. The results of this experiment determined the lifetime of the $^5D_1$ state is 33 μs

and the lifetime of the $^5D_0$ state is on the order of 1 ms. Although 33 μs is not as small as the 0.1 seconds predicted by Cowan's code for the free ion, it is still exceptionally long for a transition in a solid.

It is important to note that the linewidth experiments shown in Fig. 4.5 were done with the crystal at 4.5 K. These linewidths have a strong temperature dependence and are substantially wider at room temperature. However, once the crystal is below 7-8K, the linewidths bottom out. See Chapter 5 in Zach's thesis [45] and the references within for more information about this temperature dependence.

Although the individual europium ions have a homogeneous linewidth of 33 kHz, corresponding to the $^5D_1$ state's 33 μs lifetime, we must also take into account the inhomogeneous linewidth. Each ion in the crystal sees a slightly different perturbation from the crystal due to imperfections in the crystal. The result of this is that, instead of a 33 kHz wide absorption line, we observe a composite 1.6 GHz absorption line [70], seen on the right side of Fig. 4.5. We made the measurements shown on the right in Fig. 4.5 by sweeping our laser over the transition and monitoring the absorption.

The $^7F_0 \rightarrow ^5 D_0$ Transition

You might be looking at this transition with a bit of incredulity. We have already discussed how many of the transitions between states within the $4f^6$ configuration are allowed because of their magnetic nature. We have also discussed how there can be electric dipole transitions within this configuration according to Judd-Ofelt theory.

However, this appears to be a $J = 0 \rightarrow J = 0$ transition which is not allowed for magnetic dipole transitions or electric dipole transitions, forced or otherwise. To understand this transition, we must remember that the state labels are not actually pure LS states, but rather superpositions with the label coming from the dominant LS term. In the free ion, all the other components of the state will have the same J as the dominant term due to spherical symmetry. However, the crystal breaks this symmetry and can mix J states.

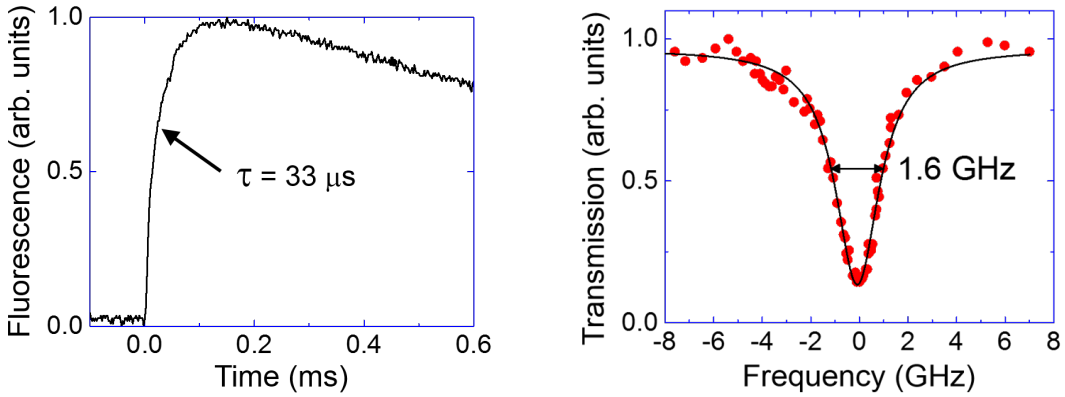

Figure 4.5: (left) Fluorescence measurement of the homogeneous linewidth. The increase in the fluorescence signal is indicative of the $^5D_1$ lifetime, and the decrease in fluorescence is can be used to find the $^5D_0$ lifetime. (right) The inhomogeneous linewidth. Both of these plots were taken with the crystal at 4.5 K. The linewidths are substantially larger at room temperature.

Just like how Judd-Ofelt theory uses the odd components of the crystal field expansion to explain electric dipole transitions via mixing with excited configuration states, we can use the even components to mix states within the same configuration with different J values. This is the case with the $^7F_0 \rightarrow ^5 D_0$ transition. In this case, the B_0^2 crystal field component mixes the nearby $^7F_2$ state into the $^7F_0$ state, thus allowing for a forced electric dipole transition.

The general case of this mixing mechanism was first discussed by Wybourne [71], and it's application to the ^{5}D$_0 \rightarrow ^7$F$_0$ transition in europium ions was first investigated by Tanaka [72]. This transition has since found applications in quantum memory protocols due to its very narrow linewidth [73] and long coherence times [63, 74]

Stark Splitting

The upper state of our transition, ^{5}D$_1$, in Eu has total angular momentum $J = 1$. Due to the presence of the crystal electric field, this level is split into three nondegenerate

Stark levels. The wavelengths and wavenumbers for transitions to these states from the $^7F_0$ state are given in Tab. 4.4 for both YSO sites. The transition that we will be using in our experiment is the lower state at site 2. This is because the spectroscopy done in [61] shows this to be the strongest transition. The next closest state, the lower state for site 1, is 113 GHz away, so there is not much danger of interfering with any of the other Stark levels, from either site.

Stark Levels		
Level	Site 1 (nm, cm^{-1})	Site 2 (nm, cm^{-1})
Upper	525.73, 19021	525.85, 19017
Middle	526.45, 18995	526.40, 18997
Lower	527.64, 18952.223	527.54, 18955.977

Table 4.4: Wavelength and wavenumber for the three Stark levels at each site in YSO [61].

Hyperfine Structure

The lower stark level of site 2 of the $^5D_1$ state and the ground state, $^7F_0$, are each split into three hyperfine levels corresponding to $m_I = \pm 1/2$, $\pm 3/2$, and $\pm 5/2$, and can be found in Fig. 4.6. Note that the scale of this splitting is substantially smaller than the splitting of the m_J states. In addition, although the decay rate from the $^5D_1$ state to the $^7F_0$ state is on the order of 1 ms, the decay rates between hyperfine levels of the $^7F_0$ state are on the order of days [59].

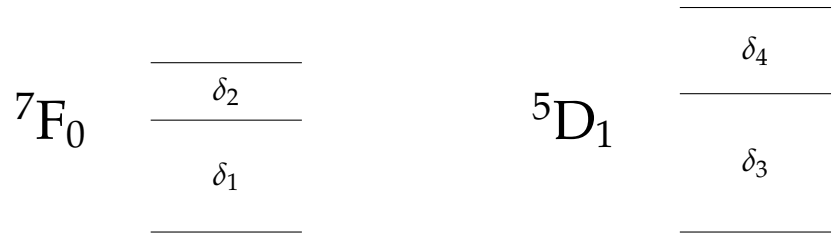

Figure 4.6: The levels on the left are the $^7F_0$ hyperfine states with splitting δ_1 and δ_2. The levels on the right are the $^5D_1$ hyperfine states with splitting δ_3 and δ_4. All values are in MHz.

The magnitude for each of these splittings for each isotope at each site can be found in Tab. 4.5. Due to numerous perturbations including magnetic and quadrupole interactions [63, 66], these are not eigenstates of the nuclear magnetic dipole moment operator. The mixing of the pure m_I states results all nine possible transitions from the $^7F_0$ state to the $^5D_1$ state to be allowed. The relative strengths of these transitions for the $^5D_0$ state were determined by Lauritzen [64]. Although we can use Lauritzen's results as an approximation for our transition, due to the similarities between the $^5D_0$ and $^5D_1$ states, the ordering of the upper state splittings, δ_3 and δ_4, is not known. This is because the inhomogeneous linewidth is much broader than the hyperfine splittings and thus makes it difficult to isolate the splittings.

	Site 1		Site 2	
Splitting	^{151}Eu	^{153}Eu	^{151}Eu	^{153}Eu
δ_4	57	144	43	114
δ_3	57	148	71	183
δ_2	34.5	90	29.5	76.4
δ_1	46.2	119	57.3	148

Table 4.5: Frequency splittings of the hyperfine levels of the $^7F_0$ and $^5D_1$ states for both isotopes and crystal sites in MHz. The data for the upper states came from [61] and the data for the lower states can be found in [62]. Additional information about the lower states in site 1 can be found in [64] and [63].

Chapter 5

Magnetic Response and Rabi Flopping

Although we had strong evidence to think that the ${}^7F_0 \rightarrow {}^5D_1$ transition is a magnetic dipole transition, we did not know how strong of a transition it was. Zach had done some work with Cowan's code and another code, RELIC (Rare Earth Level Intensity Calculation), and the two programs gave matrix elements that differed by an order of magnitude. In addition, we are well aware of the fact that the crystal field can have substantial effects on transition strengths, as is the case with the ${}^7F_0 \rightarrow {}^5D_0$ transition. Therefore, we needed to measure the dipole moment ourselves.

In addition to not having a good idea of the magnitude of the dipole moment, the chirality scheme requires establishing coherence between the two states involved in the magnetic dipole transition. The level of coherence will also depend on the magnitude of the dipole moment. Coherence had never been observed on a magnetic dipole transition at optical frequencies before, so this would add some novelty to our experiments.

A good experiment that can determine the dipole moment of our transition and demonstrate coherence between the two states is Rabi flopping. We have already talked about the susceptibility, which is a steady state quantity that depends on the dipole moment. Rabi flopping is a transient phenomenon that occurs on the way to the steady state susceptibility.

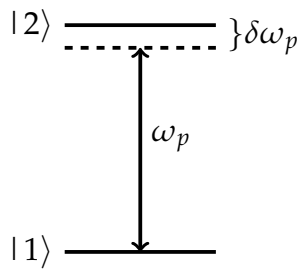

Figure 5.1: A Simple Rabi flopping energy level diagram. The probe beam has frequency ω_p and has a detuning from resonance of $\delta\omega_p = (\omega_2 - \omega_1) - \omega_p$.

Rabi Flopping Toy Model

To better understand Rabi flopping, let's consider a two level system with no decay interacting via a magnetic dipole interaction with a monochromatic beam, shown in Fig. 5.1. The Hamiltonians of the free system and the perturbing beam are

$$\hat{H}_{free} = \begin{pmatrix} \hbar\omega_1 & 0 \\ 0 & \hbar\omega_2 \end{pmatrix} \qquad \hat{H}_{int} = \hbar \begin{pmatrix} 0 & B\mu\cos(\omega_p t) \\ B\mu^*\cos(\omega_p t) & 0 \end{pmatrix} \tag{5.1}$$

where B is the magnetic field, assumed to be real for simplicity, μ is the magnetic dipole moment of the transition and ω_p is the frequency of the beam. For electric dipole interactions, we would simply substitute B and μ for their electric counterparts.

Transforming to the interaction picture and adopting the rotating wave approximation (RWA), the full Hamiltonian becomes

$$\boxed{\hat{H}_{I,RWA} = \hbar \begin{pmatrix} 0 & \frac{\Omega}{2} \\ \frac{\Omega^*}{2} & \delta\omega_p \end{pmatrix}} \tag{5.2}$$

$\Omega = \frac{B\mu}{\hbar}$ is the Rabi frequency and $\delta\omega_p = (\omega_2 - \omega_1) - \omega_p$ is the beam detuning from resonance.

Any arbitrary state of the system can be given by $|\Psi\rangle = c_1(t)|\psi_1\rangle + c_2(t)|\psi_2\rangle$ where

$|\psi_1\rangle$ and $|\psi_2\rangle$ are the ground and excited eigenstates of the free Hamiltonian, respectively, and $c_1(t)$ and $c_2(t)$ are their time dependent amplitudes. Putting this state and the Hamiltonian in Eq. 5.2 into the Schrödinger equation, we get

$$i\hbar \begin{pmatrix} \dot{c_1} \\ \dot{c_2} \end{pmatrix} = \hbar \begin{pmatrix} 0 & \frac{\Omega}{2} \\ \frac{\Omega^*}{2} & \delta\omega_p \end{pmatrix} \begin{pmatrix} c_1 \\ c_2 \end{pmatrix} \tag{5.3}$$

If we assume the system starts in the ground state by setting $c_1(t = 0) = 1$ and $c_2(t = 0) = 0$, then the particular solutions to Eq. 5.3 are

$$c_1(t) = e^{-i\frac{\delta\omega_p}{2}t} \left(\cos\left(\frac{\tilde{\Omega}t}{2}\right) + \frac{i\delta\omega_p}{\tilde{\Omega}} \sin\left(\frac{\tilde{\Omega}t}{2}\right) \right) \tag{5.4}$$

and

$$c_2(t) = -i\frac{\Omega}{\tilde{\Omega}} e^{-i\frac{\delta\omega_p}{2}t} \sin(\frac{\tilde{\Omega}t}{2}) \tag{5.5}$$

where $\tilde{\Omega} = \sqrt{\Omega^2 + \delta\omega_p^2}$.

The excited state population of our two-level system can be seen in Fig. 5.2. There, we see that the peak population in the excited state decreases as the detuning of the beam increases. We also see that the frequency of the oscillations increases as $\delta\omega_p$ increases.

The simplest way to measure the dipole moment, μ, of this transition is to tune the beam so that $\delta\omega_p = 0$ and the frequency of oscillation is equal to the Rabi frequency, $\tilde{\Omega} = \Omega$. Then we measure the frequency of oscillations as the intensity of the beam is varied. Since $\Omega \propto B$ and $B \propto \sqrt{I}$, we expect the oscillation frequency to vary as $\Omega \propto \mu\sqrt{I}$.

If there is no decay in the system, the transient effects will obviously not go away. We can incorporate decay into the two level model and find our way to the steady state

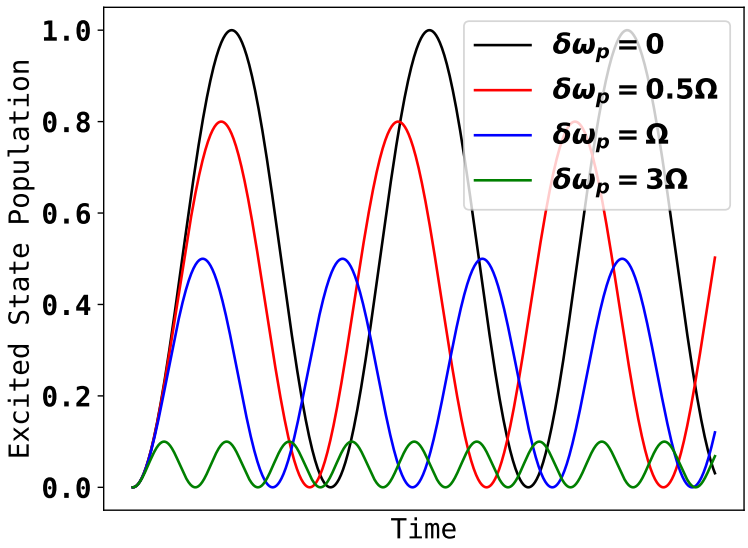

Figure 5.2: The excited state population for our two-level, non-decaying example. As $\delta\omega_p$ becomes larger, the peak excited state population decreases and the oscillation frequency increases.

solution by adding a phenomenological decay rate to the Hamiltonian

$$\hat{H} = \hbar \begin{pmatrix} 0 & \frac{\Omega}{2} \\ \frac{\Omega^*}{2} & \delta\omega_p - i\Gamma \end{pmatrix}. \tag{5.6}$$

This sort of phenomenological model causes the population to decay out of the system. The result is that the oscillations in Fig. 5.2 are modified by an exponential decay envelope.

We can find the steady state solution by using the Liouville-Von Neumann equation,

$$\dot{\rho} = -\frac{i}{\hbar}[\hat{H}, \rho] \tag{5.7}$$

with our two-level Hamiltonian with the phenomenological decay. This gives us

$$\dot{\rho} = -\frac{i}{\hbar}\begin{pmatrix} \rho_{21}\Omega - \rho_{12}\Omega^* & (\rho_{22}-\rho_{11})\Omega - (i\Gamma - \delta\omega_p)\rho_{12} \\ (\rho_{11}-\rho_{22})\Omega^* + (i\Gamma - \delta\omega_p)\rho_{21} & \rho_{12}\Omega^* - \rho_{21}\Omega \end{pmatrix} \tag{5.8}$$

‘ By setting the time derivative to zero, we find the steady state coherence to be

$$\rho_{12} = \frac{(\rho_{22}-\rho_{11})\Omega}{i\Gamma - \delta\omega_p}. \tag{5.9}$$

5.0.1 Rabi Flopping Setup and Procedure

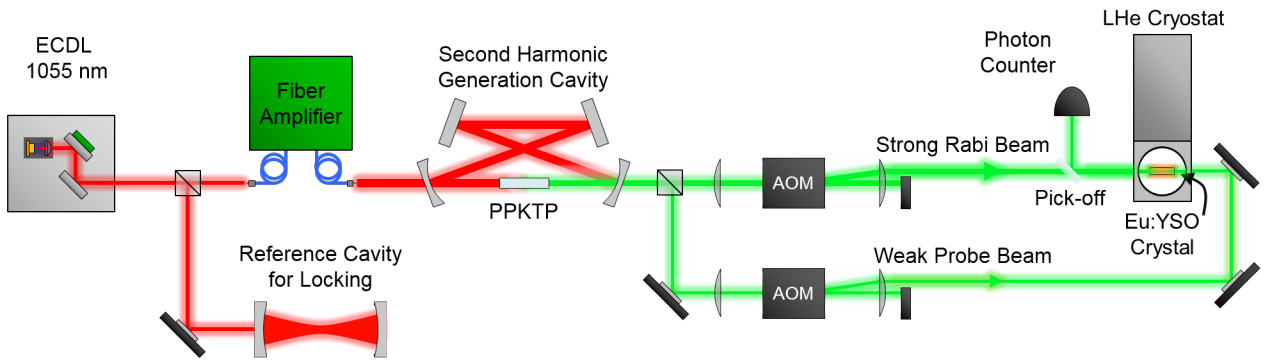

Figure 5.3: The experimental setup for our Rabi flopping experiment

To access the $^7F_0 \rightarrow {}^5D_1$ transition in our experiment, we start with a costum-built infrared external cavity diode laser (ECDL) set up in the Littrow configuration [75]. The output of the ECDL has a wavelength of 1055 nm with a linewidth of about 0.5 MHz and optical power of 25 mW. Part of the output of the ECDL is picked off and sent to an ultra-low expansion (ULE) cavity that serves as a frequency reference. The ULE is also used for the Pound-Drever-Hall locking method [76] which ultimately gives us an absolute frequency stability of 50 kHz. More information on the locking system can be found in Zach Simmon’s thesis [45].

The ECDL output is then amplified to an optical power exceeding 5 W using a fiber

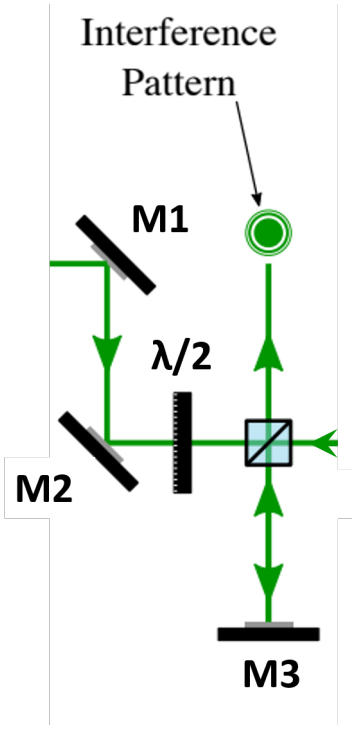

Figure 5.4: The setup used to overlap the Rabi and probe beams. The Rabi beam, coming in from the right, was retroreflected onto itself using the mirror M3. Then, M1 and M2 were used to overlap the probe beam with the Rabi beam. The beams were considered overlapped when a bull's eye interference pattern could be seen.

amplifier. We frequency-double the fiber amplifier output using cavity-based second harmonic generation with a 2-cm-long periodically-poled nonlinear crystal (PPKTP) with a poling period adjusted for phase matching at 1055 nm and temperature controlling with a temperature stability at the level of 1 mK. The SHG from the PPKYP crystal was enhanced by putting the PPKTP crystal in a ring cavity. One of the mirrors of this SHG cavity was mounted on a piezoelectric transducer which is used to lock the SHG cavity to the amplifier output using the Hansch-Couillaud method [77]. Using this set-up we are able to produce green light at a wavelength of 527.5 nm with an optical power exceeding 1.5 W. More information on our SHG setup cam be found in Nick Brewer's thesis [69].

The green output from the doubling cavity is then split into two beams. Each beam

goes through an acousto-optic modulator (AOM) for frequency and timing control. The AOMs have a center frequency of 80 MHz. The beams are focused through the AOMS with a waist of 400 μm giving them a turn-on-time of about 50 ns.

We use a 3-mm-long Eu:YSO crystal which is housed in a continuous-flow liquid helium cryostat, and cooled to a temperature of 4.5 K. The crystal is cut such that light propagates along the b crystallographic axis and the magnetic-field of the laser is aligned with the D_1 axis. The maximum power of the coupling beam at the cryostat is 300 mW, and its waist is 56 μm. The total power in the coupling beam was monitored with a calibrated photodiode. Since the beam profile of the coupling beam is Gaussian, the coupling beam's spatial intensity profile will induce a spatially varying Rabi frequency in the crystal. In order to sample the center part of the coupling beam where the Rabi frequency is most uniform, we focus the probe beam, which has a power of less than 1 pW, down to 18 μm.

The probe and coupling beam are sent into the cryostat in a counterpropagating configuration. This was done so that a pickoff could be used to select the probe beam for detection and minimize background from the coupling beam. In order to ensure the counterpropagating beams were overlapped, we used the setup in Fig. 5.4. First we used the mirror to retroreflect the coupling beam and ensure that it was overlapped with itself. Then, we used separate mirrors not shown in the diagram to walk the probe beam until we saw a bull's eye interference pattern, indicating the two beams were overlapped.

The pulse sequence we used is shown in Fig. 5.5. With the cryostat at 4.5 K, the sequence starts with a powerful Rabi pulse. The length of this pulse is varied from shot to shot and lasts from 0 - 2 μs. 15 μs after the end of the Rabi pulse is a 5 μs probe pulse. Ideally, we would send in the probe pulse immediately after the Rabi pulse. However, there is some fluorescence that occurs after the Rabi pulse is turned off that we do not fully understand. We add in the 15 μs delay to avoid detecting this fluorescence. After each shot we reset the atoms by increasing the temperature of the cryostat to 20

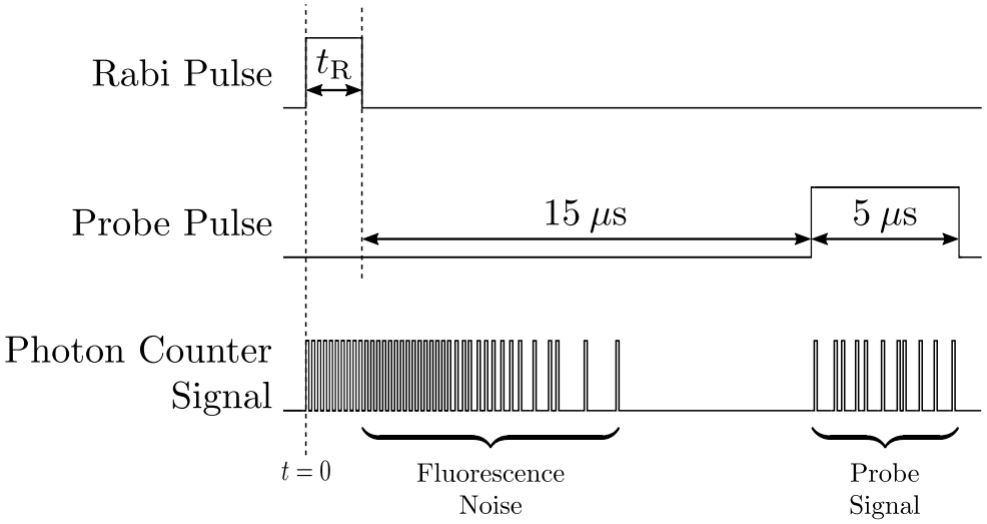

Figure 5.5: The Rabi flopping pulse sequence. Taken from [69].

K and then bringing the temperature back down to 4.5 K using the computer controlled temperature controller for the cryostat.

The timing of the experiment was coordinated by a computer controlled pulse generator. The pulse generator was used in conjunction with RF switches to control the timing of the AOMs. The RF generators that drove the AOMs were also computer controlled, which allowed us to control the power of the beams. The signal was monitored with a photon counting module which was gated with the pulse generator. The signal from the photon counter was monitored on an oscilloscope, and the data was read from the scope to the computer via GPIB.

5.0.2 Results

We proceed with a discussion of our Rabi flopping measurements [70]. With the ions starting in the ground state $^7F_0$ (equally populating the three hyperfine levels), we apply a Rabi flopping laser pulse of certain duration to the ions. Due to the interaction with the Rabi flopping laser, the ionic population starts to flow coherently back and forth between the ground and excited levels. Depending on the duration of the Rabi pulse,

the ions may be left in any one of the levels or in a superposition of the two at the end of the pulse. After the Rabi flopping laser is turned-off, we turn-on a counter-propagating weak probe pulse and measure the transmission of the probe through the crystal with a photon-counter. Using this set-up, the Rabi flopping of the ions is then revealed by the transmission of the probe laser beam, through stimulated absorption and emission.

Fig. 5.6 shows the normalized transmission of the probe laser through the crystal as the duration of the Rabi pulse is varied. For each pulse duration, each data point is an average of ten experiments with the error bar denoting the standard deviation of the set. We observe a clear Rabi flopping cycle with a flopping frequency approaching 1 MHz. The Rabi flopping quickly dephases after about two cycles due to two main reasons: (i) We perform this experiment using the whole inhomogeneously broadened ensemble. As a result, the Rabi laser is only resonant with a small fraction of ions. Off-resonant atoms flop at faster rates but with a much reduced contrast which contributes to the dephasing of the Rabi cycle. (ii) Since we do not perform any optical pumping between hyperfine levels, Rabi flopping happens simultaneously between each ground and excited hyperfine level combination, i.e., there are nine different simultaneous excitations. The spread of the magnetic-dipole matrix element between respective transitions also contributes to the fast dephasing of the Rabi cycle [64].

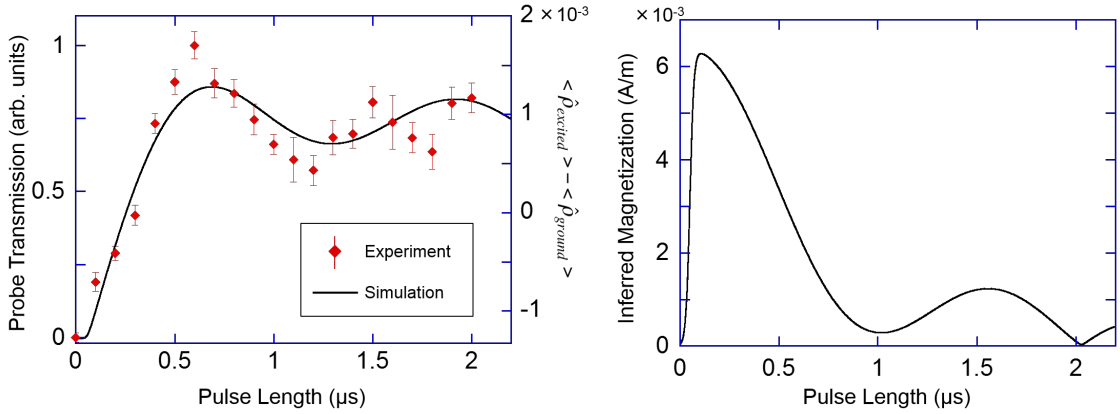

Figure 5.6: The transmission of the probe laser beam through the crystal as the duration of the Rabi pulse is varied. We observe a clear Rabi cycle with a frequency approaching 1 MHz. The Rabi oscillation quickly dephases due to a number of processes such as the variation of the magnetic-dipole matrix element among various hyperfine transitions. The solid line is a numerical simulation that solves the density matrix for a large number of atoms whose whose absolute transition frequencies are spread through the inhomogeneous profile, causing different hyperfine transitions to be resonant with the laser. The lower plot shows the inferred magnetization from the same simulations. See text for details.

Because we observe only about two cycles, there is significant uncertainty in the observed Rabi frequency from a single flopping experiment. For accurate measurement of the magnetic dipole matrix element, we perform the Rabi flopping measurement of Fig. 5.6 at various Rabi pulse intensities. Fig. 5.7 shows the observed Rabi frequency as a function of laser intensity for 23 Rabi flopping measurements. For each measurement, the vertical error bar represents the uncertainty of the deduced Rabi frequency for that specific flopping experiment. The insets show six specific Rabi flopping experiments as the laser intensity is varied from 5630 W/cm^2 to 1510 W/cm^2. From the square-root fit to the observed data values (the solid line in the main plot) we deduce the magnetic-dipole matrix element to be $\mu = (0.063 \pm 0.005)\mu_B$ for the magnetic field oriented along

the quantization axis of the crystal (the D_1 crystallographic axis).

As we discussed before, the $4f$ electronic configuration of rare-earth ions are typically in the intermediate coupling regime, i.e., neither LS-coupling nor jj-coupling accurately describes the wavefunctions. Using intermediate-coupled wavefunctions of the free ion and well-known methods of Racah algebra, calculations give a theoretical value of $\mu = 0.096\mu_B$ for the magnetic dipole matrix element. The calculated theoretical value is therefore within 50% of the measured experimental value of the matrix element. At the end of this chapter we discuss a possible explanation for the discrepancy between our measured value and this calculated value.

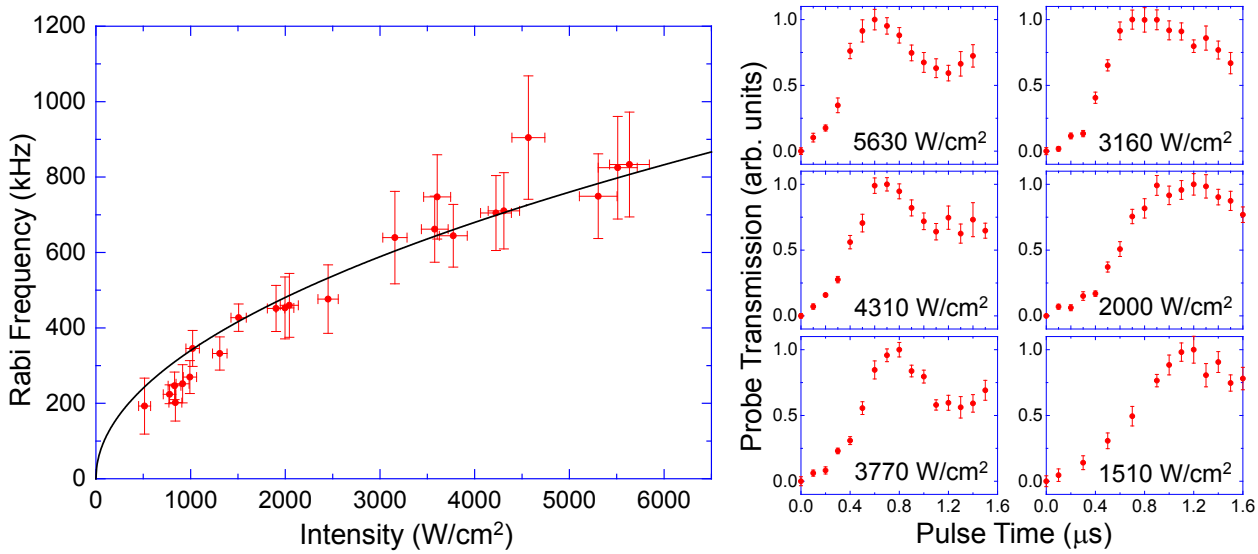

Figure 5.7: The observed Rabi flopping frequency as the laser intensity is varied for 23 different Rabi flopping experiments. From the square-root fit to the data points (the solid line), we deduce a magnetic-dipole matrix element of $\mu = (0.063 \pm 0.005)\mu_B$. The insets show six specific flopping experiments (probe transmission vs Rabi pulse duration) as the laser intensity is varied from 5630 W/cm^2 to 1510 W/cm^2.

Using the measured value of the magnetic-dipole matrix element, we performed density matrix simulations of the system. For this purpose, we take 80,000 ions, spread their transition frequencies between ± 0.5 GHz to incorporate the inhomogeneous profile, nu-

merically solve the time-domain evolution of the density matrix for each ion using the Liouville equation

$$\dot{\rho} = -\frac{i}{\hbar}[\hat{H}, \hat{\rho}] - \frac{1}{2}\{\hat{\Gamma}, \hat{\rho}\}, \tag{5.10}$$

and calculate the ensemble-averaged response. For the time-domain evolution, we include all six hyperfine levels of the $^7F_0 \rightarrow {}^5D_1$ transition, using the relative magnitudes of the dipole matrix elements from [64], as well as the $^5D_0$ level; i.e., the size of the density matrix $\hat{\rho}$ is 7×7. Our model takes into account (i) interaction with the laser pulse, (ii) non-radiative relaxation from the $^5D_1$ level to $^5D_0$ level at a rate Γ (homogeneous linewidth), and (iii) the spread of the transition frequencies due to the inhomogeneous broadening. See Nick's thesis for more details on the simulations [69].

The solid line on the left in Fig. 5.6 shows the calculated difference between the population of the excited hyperfine levels and the ground hyperfine levels, $< \hat{\rho}_{excited} > - < \hat{\rho}_{ground} >$ (we use the notation $< ... >$ to mean average over the inhomogeneously broadened ensemble), as the Rabi pulse duration is varied. The numerical simulation accurately produces the frequency and the contrast observed in the Rabi flopping experiment. In the plot on the right in Fig. 5.6, we calculate the inferred magnetization of the ensemble, by extracting the coherences (the off-diagonal density matrix elements) from the same numerical simulations, $M = N < \hat{\rho}_{off-diagonal} > \mu$ (the quantity N is the ionic density). The ensemble-averaged magnetization reaches a peak value of $M = 5.5 \times 10^{-3}$ A/m and then sharply drops. This peak magnetization is equivalent to a current loop of area 1 cm^2 with a current of 1 mA running through it, but the current is oscillating at 570 THz.

We can use our measured value of the magnetic dipole moment to extrapolate the magnetic susceptibility of this transition. The results are shown in Fig. 5.8. This extrapolation was done by taking the susceptibility formula in Eq. 2.59 with the specific form

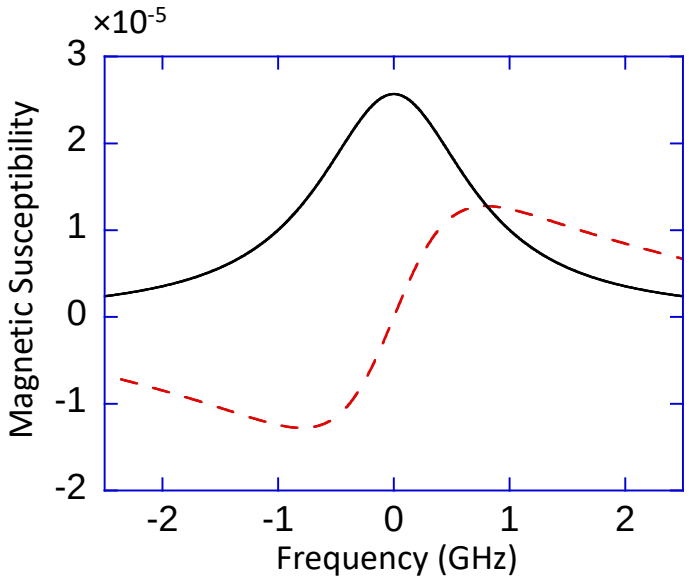

Figure 5.8: The susceptibility we inferred from our measurements and simulations.

of the coherence for Rabi flopping, Eq. 5.9, as the homogeneous linewidth. Then, this homogeneous lineiwdth is convolved over the inhomogeneous linewidth to give the plot in Fig. 5.8.

Although this susceptibility is small, it is still enough to produce left-handed waves with the externally driven scheme. With our measured value of the magnetization, the relation

$$\frac{|\vec{P}|}{|\vec{M}|} = \frac{N^2+1}{2cn}, \tag{5.11}$$

and the results of [34], an external polarization of $\vec{P}_{ext} \approx 2 \times 10^{-11}$ C/m^2 would produce left-handed waves with intensity on the order of 100 nW/cm^2. This level of polarization is well within the realm of possibility of a typical host crystal with a second order response, and the left-handed wave intensity is also reasonable to detect. In addition, the chirality scheme only needs a mangetic susceptibility of about 10^{-2} to produce a nega-

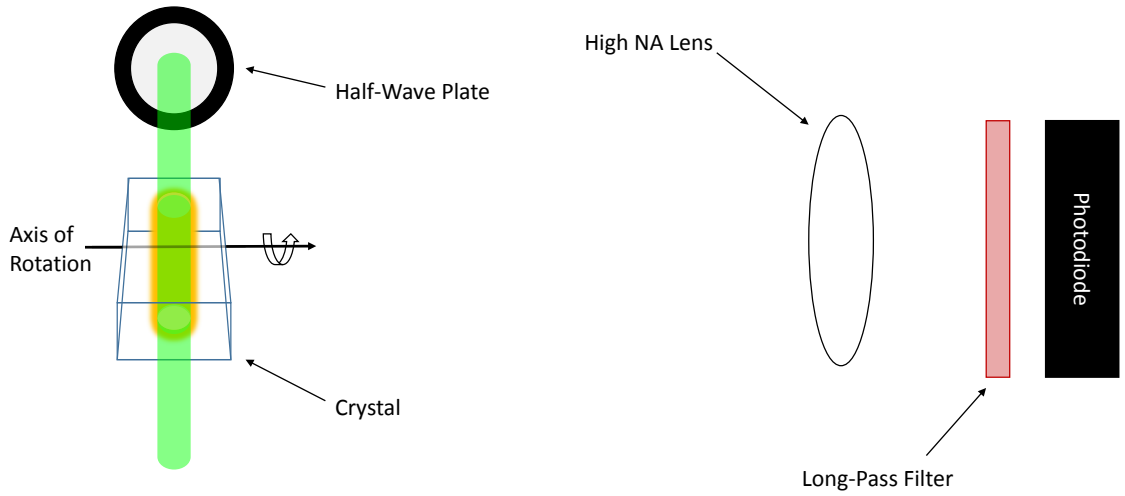

Figure 5.9: The setup that we used to verify the magnetic nature of our transition. The half-wave plate was used to align either the electric or magnetic field with the axis of rotation of the crystal which is also one of the crystal's optical axes. As the crystal is rotated, the field that is parallel to the axis of rotation remains aligned with that optical axis, while the other field changes its orientation. The fluorescence was then collected with a high NA lens and a long-pass filter was used to cut out any scattered green light.

tive index of refraction. Although we are not at that level either, the magnetic response can be enhanced by either finding a stronger transition or increasing the ionic density.

5.0.3 Magnetic Dipole Verification

We next discuss how we have verified that the electrons interact with the magnetic field of the laser during the $^7F_0 \rightarrow {}^5D_1$ excitation. We note that we cannot use the method outlined in Ref. [58]. This is because our experiment uses a $\sim$mm scale crystal, and as a result, we cannot utilize the unique magnetic-field profile of a tightly focused radially

polarized laser.

Instead, we have studied angle dependent fluorescence from the crystal with light propagating along each crystallographic axis and for two orthogonal polarizations (S and P polarized). This measurement was performed using a thicker crystal with dimensions 4 mm$\times$5 mm$\times$10 mm and outside the cryostat (i.e., at room temperature) so that we had access to all propagation axes of the crystal. The main idea behind this measurement is depicted in the schematic shown in Fig. 5.9 and results are shown in Fig. 5.10 and 5.11. Consider S polarized light propagating along a certain axis of the crystal, as shown in part (a) of Fig. 5.10. The laser excites the crystal and we record the total fluorescence using a high-numerical-aperture lens and a photo-detector (not shown in Fig. 5.10). If the excitation is due to interaction with the magnetic-field, as the crystal is rotated along the axis shown, we would expect a change in the amount of excitation (and therefore the amount of fluorescence recorded). This is because, the crystal is highly anisotropic and as the crystal is rotated, the angle between the magnetic field and the crystallographic axes would change. For this geometry, we would not expect variation in the fluorescence if the excitation is due to the electric-field since its orientation with respect to all axes remains unchanged. For P polarized light [part (b) in Fig. 5.10], the roles of the electric and magnetic fields would be reversed. The plot in Fig. 5.10 shows this measurement for light propagating along the D_1 axis of the cystal with the crystal rotated around the b axis. The measurement conclusively shows that the fluorescence changes when the direction of the B-field is varied and therefore proves the magnetic-dipole nature of the excitation.

We have performed the angle-dependent fluorescence measurements with light propagating along the other axes of the crystal. Similar to the measurements of Fig. 5.10, for light propagating along a specific crystal axis, we record the total fluorescence as the crystal is rotated for two polarizations of light. These measurements are shown in the below figure. For each propagation axis, the fluorescence changes when the direction of

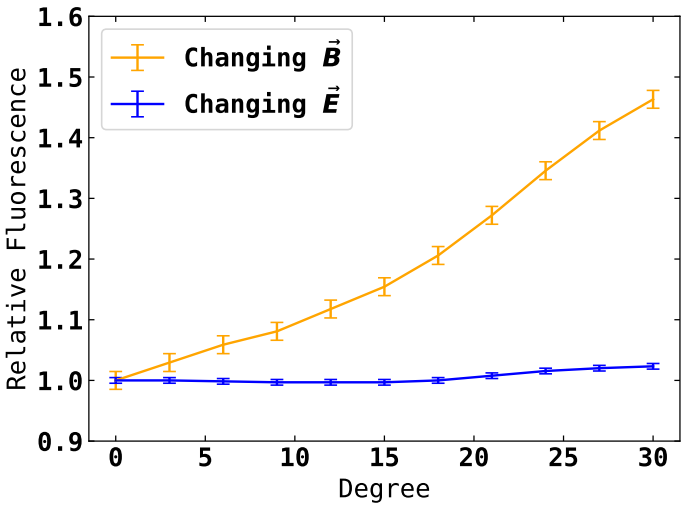

Figure 5.10: Fluorescence from the crystal as a function of the angle of incidence for S-polarized (changing $\vec{B}$ orientation), and P-polarized (changing $\vec{E}$ orientation) light. The beam is propagating along the D_1 axis and the crystal is rotated around the b axis. The fluorescence signal is normalized to take into account both the change in the Fresnel reflection losses from the surfaces and the path-length change of the beam as the crystal is rotated. The large increase in the fluorescence for S-polarized light is due to a change of the direction of the angle of the magnetic field with the crystallographic axes. In contrast, when the angle of the electric field is varied (P-polarized), there is negligible change in the fluorescence. This shows that during $^7F_0 \rightarrow {}^5D_1$excitation, light interacts with the magnetic field of light instead of the electric field.

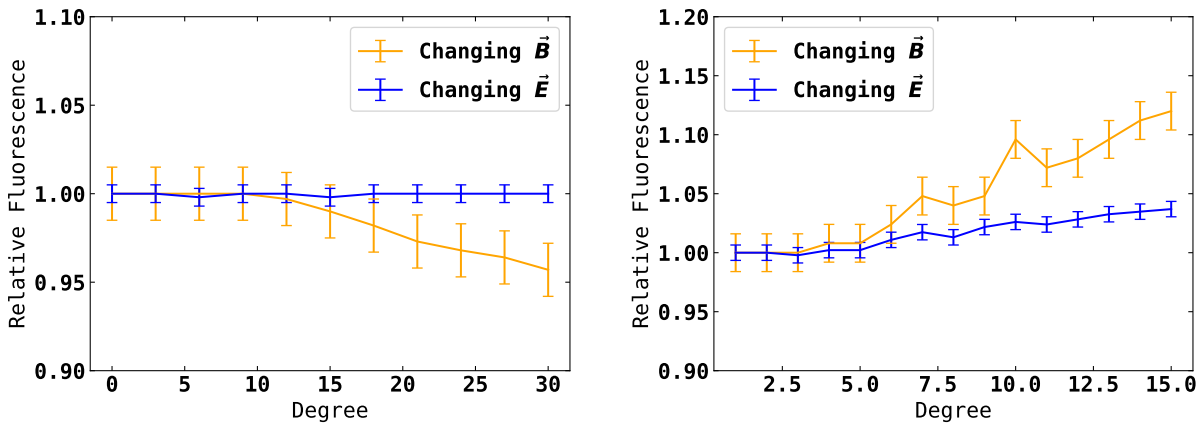

Figure 5.11: Total fluorescence from the crystal as a function of the angle of incidence for light propagating along the D_2 axis and rotation around the b axis (left) and propagation along the b axis and rotation around the D_1 axis (right) of the crystal. Similar to Fig. 5.10, S - polarization corresponds to the changing $\vec{B}$ orientation and P - polarization corresponds to changing $\vec{E}$ orientation.

the magnetic field is changing, and stays relatively constant when the direction of the electric field is varied. The data points for part (c) and (d) in Fig. 5.11 suffer from the technical limitations due to long propagation distance in the crystal.

5.1 Calculation of the Magnetic Dipole Moment

We can get an idea for a theoretical value of the magnetic dipole moment of our transition by using the tensor operator methods. We can start with the states calculated by Ofelt [1]

$$|^7F_0\rangle = 0.9680|^7F_0\rangle_{LS} + 0.0016|^5D_0\rangle_{LS} + 0.1659|^5D_0'\rangle_{LS} - 0.1815|^5D_0''\rangle_{LS} \tag{5.12a}$$

$$|^5D_1\rangle = -0.2096|^7F_1\rangle_{LS} - 0.2066|^5D_1\rangle_{LS} + 0.7162|^5D_1'\rangle_{LS} - 0.5561|^5D_1''\rangle_{LS}. \tag{5.12b}$$

The subscript LS in Eqs. 5.12 denote eigenstates of the LS basis and $'$, $''$ denote seniority number. If one uses Cowan's code [42] to find the states, there will be more LS terms. However, their amplitudes will be very small and will contribute very little to the final result. This was checked computationally. These states, along with the magnetic dipole operator

$$\hat{\mu} = -\mu_B(J + S), \tag{5.13}$$

where we have assumed $g = 2$, can be used with the Wigner-Eckart theorem

$$\langle \alpha J M_J | T_q^{(k)} | \alpha' J' M_J' \rangle = (-1)^{J - M_J} \begin{pmatrix} J & k & J' \\ -M_J & q & M_J' \end{pmatrix} \langle \alpha J || T^{(k)} || \alpha' J' \rangle \tag{5.14}$$

and

$$\begin{aligned} \langle SLJ || (J+S)^{(1)} || S'L'J' \rangle =& \delta_{SLJ,S'L'J'} \sqrt{J(J+1)(2J+1)} \\ &+ \delta_{SL,S'L'} (-1)^{S+L+J+1} \sqrt{(2J+1)(2J'+1)S(S+1)(2S+1)} \begin{Bmatrix} L & S & J \\ 1 & J' & S \end{Bmatrix} \end{aligned} \tag{5.15}$$

to give us a magnetic dipole moment of

$$\mu = -0.0955 \mu_B \tag{5.16}$$

This is obviously pretty different than the $0.063 \pm 0.005 \mu_B$ that we got from our Rabi flopping experiments.

The calculations above, however, use the free-ion states. These states do not account for crystal field effects which will modify the LS expansion amplitudes and potentially mix in new LS states.

5.1.1 J-Mixing and the Eu^{3+} Dipole moment discrepancy

The main affect caused by the crystal field that is not accounted for by other perturbations is known as J-mixing. The states of the free ion are calculated with full spherical symmetry. Therefore, J is still a good quantum number. However, when the ion is placed in the crystal field, the spherical symmetry is broken and is reduced to that of the point group of the dopant cite. As we have discussed, the crystal field effects can be incorporated into the Hamiltonian as a perturbation. For the $4f \rightarrow 4f$ transitions in rare earth ions, the expansion is

$$V = \sum_{k=0,even}^{6} \sum_{q=-k}^{k} B_q^k C_q^k. \tag{5.17}$$

The nonzero values of B_q^k are determined by the crystal field symmetry.

The effects of the crystal field can be incorporated into the transition strength by using second order double perturbation theory. The two second order contributions are

$$\langle \psi_g^{(1)} | D_\rho^{(1)} | \psi_e^{(0)} \rangle = \sum_{n \neq g} \frac{\langle \psi_g^{(0)} | V_{crys} | \psi_n^{(0)} \rangle \langle \psi_n^{(0)} | D_\rho^{(1)} | \psi_e^{(0)} \rangle}{E_n^{(0)} - E_g^{(0)}} \tag{5.18a}$$

$$\langle \psi_g^{(0)} | D_\rho^{(1)} | \psi_e^{(1)} \rangle = \sum_{n \neq e} \frac{\langle \psi_g^{(0)} | D_\rho^{(1)} | \psi_n^{(0)} \rangle \langle \psi_n^{(0)} | V_{crys} | \psi_e^{(0)} \rangle}{E_n^{(0)} - E_e^{(0)}}. \tag{5.18b}$$

where the $|\psi^{(0)}\rangle$ states are the states of the free ion with J as a good quantum number. $|\psi_g^{(0)}\rangle$ is the initial state, $|\psi_e^{(0)}\rangle$ is the final state, and $|\psi_n^{(0)}\rangle$ are the intermediate states that will be mixed into the initial and final states of the transition. $D_\rho^{(1)}$ is the dipole moment operator with rank 1 and polarization ρ.

The matrix matrix elements can be evaluated using the Wigner-Eckart theorem. For Eq. 5.18a we have

$$\begin{aligned}
\langle \psi_g^{(0)} | V_{crys} | \psi_n^{(0)} \rangle &= \langle SLJM_J | V_{crys} | S''L''J''M_J'' \rangle \\
&= (-1)^{J-M_J} \begin{pmatrix} J & k & J'' \\ -M_J & q & M_J'' \end{pmatrix} \langle SLJ || V_{crys} || S''L''J'' \rangle \\
\langle \psi_n^{(0)} | D_\rho^{(1)} | \psi_e(0) \rangle &= \langle S''L''J''M_J'''' | D_\rho^{(1)} | S'L'J'M_J' \rangle \\
&= (-1)^{J''-M_J''} \begin{pmatrix} J'' & 1 & J' \\ -M_J'' & \rho & M_J' \end{pmatrix} \langle S''L''J'' || D_\rho^{(1)} || S'L'J' \rangle
\end{aligned} \tag{5.19}$$

Putting these together gives us

$$\begin{aligned}
\langle \psi_g^{(0)} | V_{crys} | \psi_n^{(0)} \rangle \langle \psi_n^{(0)} | D_\rho^{(1)} | \psi_e(0) \rangle = (-1)^{J+J''-M_J-M_J''} &\begin{pmatrix} J & k & J'' \\ -M_J & q & M_J'' \end{pmatrix} \begin{pmatrix} J'' & 1 & J' \\ -M_J'' & \rho & M_J' \end{pmatrix} \\
&\times \langle SLJ || V_{crys} || S''L''J'' \rangle \langle S''L''J'' || D_\rho^{(1)} || S'L'J' \rangle .
\end{aligned} \tag{5.20}$$

The matrix elements for Eq. 5.18b are

$$\begin{aligned}
\langle \psi_g^{(0)} | D_\rho^{(1)} | \psi_n^{(0)} \rangle &= \langle SLJM_J | D_\rho^{(1)} | S''L''J''M_J'' \rangle \\
&= (-1)^{J-M_J} \begin{pmatrix} J & 1 & J'' \\ -M_J & \rho & M_J'' \end{pmatrix} \langle SLJ || D_\rho^{(1)} || S''L''J'' \rangle \\
\langle \psi_n^{(0)} | V_{crys} | \psi_e(0) \rangle &= \langle S''L''J''M_J'''' | V_{crys} | S'L'J'M_J' \rangle \\
&= (-1)^{J''-M_J''} \begin{pmatrix} J'' & k & J' \\ -M_J'' & q & M_J' \end{pmatrix} \langle S''L''J'' || V_{crys} || S'L'J' \rangle
\end{aligned} \tag{5.21}$$

which together gives us

$$\langle \psi_g^{(0)}|D_\rho^{(1)}|\psi_n^{(0)}\rangle\langle\psi_n^{(0)}|V_{crys}|\psi_e(0)\rangle = (-1)^{J+J''-M_J-M_J''}\begin{pmatrix} J & 1 & J'' \\ -M_J & \rho & M_J'' \end{pmatrix}\begin{pmatrix} J'' & k & J' \\ -M_J'' & q & M_J' \end{pmatrix} \times \langle SLJ||D_\rho^{(1)}||S''L''J''\rangle\langle S''L''J''||V_{crys}||S'L'J'\rangle. \tag{5.22}$$

We can get additional restrictions on the crystal field terms by considering the 3-J terms in Eqs. 5.20 and 5.22. Using the rules of 3-J symbols, the restrictions are

$$\begin{pmatrix} J & k & J'' \\ -M_J & q & M_J'' \end{pmatrix}\begin{pmatrix} J'' & 1 & J' \\ -M_J'' & \rho & M_J' \end{pmatrix}$$

$$J'-1 \le J'' \le J'+1 \qquad M_J'' = M_J' + \rho \tag{5.23a}$$

$$J''-J \le k \le J''+J \qquad q = M_J - M_J'' \tag{5.23b}$$

$$J'-J-1 \le k \le J+J'+1 \qquad q = M_J'' - M_J' - \rho \tag{5.23c}$$

for Eq. 5.20 and

$$\begin{pmatrix} J & 1 & J'' \\ -M_J & \rho & M_J'' \end{pmatrix}\begin{pmatrix} J'' & k & J' \\ -M_J'' & q & M_J' \end{pmatrix}$$

$$J-1 \le J'' \le J+1 \qquad M_J'' = M_J - \rho \tag{5.24a}$$

$$J''-J' \le k \le J''+J' \qquad q = M_J'' - M_J' \tag{5.24b}$$

$$J-J'-1 \le k \le J+J'+1 \qquad q = M_J - M_J' - \rho \tag{5.24c}$$

for Eq. 5.22. The unprimed quantities correspond to the ground state, the primed quantities correspond to the excited states, and the double prime states are the states that are being mixed in by the crystal field.

For YSO, the dopant cite has C_1 symmetry. With such low symmetry, we would expect all of the crystal field parameters with $k < 6$ to be nonzero. However, we can plug in the relevant parameters from $^7F_0$, $^5D_1$, and linearly polarized light into Eqs. 5.23 and 5.24 to get

$$\begin{pmatrix} 0 & k & J'' \\ 0 & q & M_J'' \end{pmatrix} \begin{pmatrix} J'' & 1 & 1 \\ M_J'' & 0 & 0 \end{pmatrix} \quad \& \quad \begin{pmatrix} 0 & 1 & J'' \\ 0 & 0 & M_J'' \end{pmatrix} \begin{pmatrix} J'' & k & 1 \\ M_J'' & q & 0 \end{pmatrix}. \tag{5.25}$$

We see from Eq. 5.25 that the only allowable values for k are 0 and 2 and that the only allowable value for q is zero. This means that the only state that can be mixed in (to second order) is the $^7F_2$ state.

The crystal field parameter B_q^k are typically on the order of a few hundred inverse centimeters [50]. If we take a value of $B_0^2 = 500$ cm^{-1} and the fact that $^7F_2$ is 1173 cm^{-1} above $^7F_0$, according to Cowan's code, with Eqs. 5.18 to find a new value of the magnetic dipole moment of

$$\mu = -0.0694\mu_B. \tag{5.26}$$

Of course there are numerous effects within the crystal that could also be affecting the dipole moment and an actual measurement of the crystal field parameters for YSO would be needed to be conclusive. However, this calculation shows that, with typical values of the crystal field parameters, we can get our dipole moment calculation much closer to our measured value.

Chapter 6

Magnetic Response and Susceptibility

6.1 Manipulating the Magnetic Response Through Linear Optics: Spectral Hole Burning

As we have already discussed, although the (homogeneous) linewidth of an individual europium ion in YSO is 33 kHz, each ion experiences a slightly different Stark shift. This variation causes a variation in the center frequencies of the homogeneous lines. The result of this variation is a composite linewidth, called the inhomogeneous linewidth, composed of the 33 kHz lines of all the ions in our crystal with their center frequencies shifted here and there around the center of the inhomogeneous line.

The experiments described in the previous chapter were performed using the entire inhomogeneous line. The linewidth of the inhomogeneous broadening is 1.6 GHz, substantially wider than the homogeneous linewidth and the europium hyperfine splittings. The fact that the inhomogeneous line is wider than the hyperfine splitting makes it impossible to use a single beam at a single frequency to address transition from a particular ground hyperfine state to a particular excited hyperfine state. From here on, I will refer to all the $^7F_0$ hyperfine states as just the ground states and the $^5D_1$ hyperfine states as just the excited states since these are the only electronic levels being addressed by our

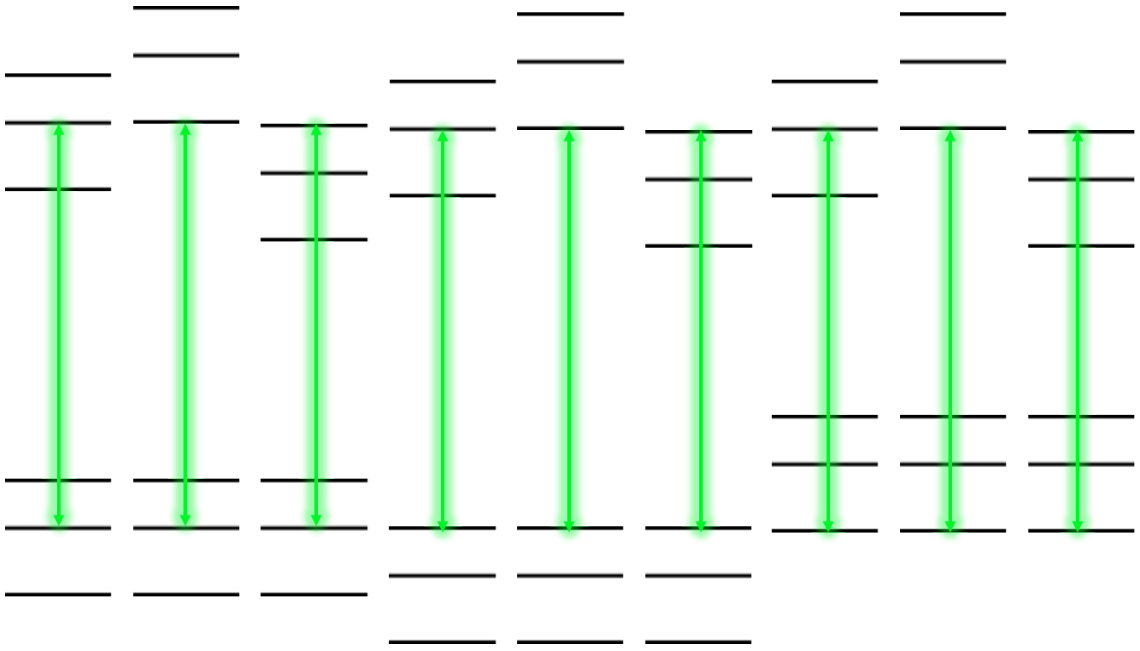

Figure 6.1: All the transitions induced by a single laser beam in Eu:YSO. Each set of six states is referred to as an ion class. All the ions in an ion class experience a similar Stark shift and therefore has similar transition frequencies between the ground and excited states. Because the inhomogeneous broadening is wider than the hyperfine splittings in europium, a single beam will end up addressing nine different ion classes, one ion class for each possible transition.

lasers.

The transitions induced by a single laser beam can be seen in Fig. 6.1. Each of the nine sets of six energy levels is referred to as an ion class and correspond to transitions in different europium ions. The thing that defines an ion class is that each member ion of the class experiences a similar Stark shift and will therefore have the same set of transition frequencies between the ground and excited states. Since this set of frequencies changes from ion to ion, when a single beam is turned on at a fixed frequency, this beam will end up addressing the nine ion classes shown in Fig. 6.1 corresponding to the nine possible combinations of ground and excited states.

If the beam in Fig. 6.1 is intense enough and left on for a long enough time, the

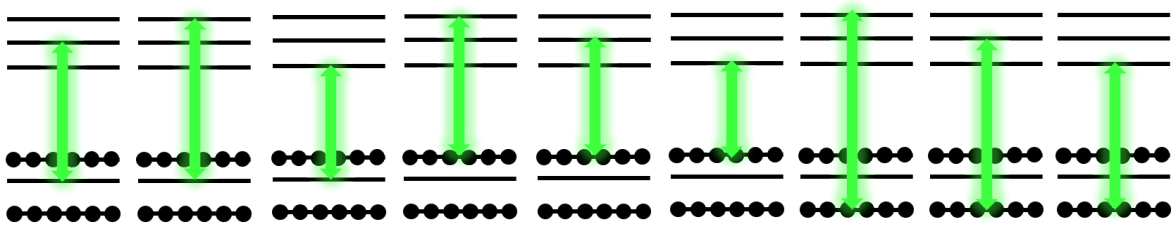

Figure 6.2: After a single beam at a fixed frequency has interacted with the nine ion classes, the nine ground states that were addressed by the beam will have been emptied out and the population pumped to the other two ground states in each ion class. In the figure above, we have a single beam whose frequency is being swept over a single ion class with one ground state empty and the other two with excess population. Whenever the empty ground state is connected to an excited state by the beam there will be a drop in absorption; when a ground state with excess population is connected to an excited state there will be additional absorption.

ground state of each ion class that is addressed by the beam will be emptied out and the population will be pumped to the other two ground states of that ion class. Because the ground state lifetimes in Eu:YSO are very long at cryogenic temperatures, this population distribution will persist. Now, lets consider a single ion class with this population distribution and sweep the frequency of a single beam over it. This scenario is shown in Fig. 6.2. When the sweeping beam connects the emptied state to one of the three excited states there will be an decrease in absorption of the beam. However, when the sweeping beam connects one of the states with excess population to an excited state there will be increased absorption. The result is that this ion class will produce spectral holes, or reductions in absorption, at three frequencies and spectral antiholes, or increases in absorption, at six more frequencies for a total of nine spectral features. Since each of the nine ion classes will produce nine spectral features, we will have a total of 81 spectral features[1]. Since there are two isotopes of europium in our crystal with different hyperfine

[1]Some of these features wind up at the same frequencies so the total number of unique frequencies is slightly less than 81.

splittings, there turns out to be double the number of spectral features. All the possible spectral features for our crystal are shown in Fig. 6.3. All ion classes will produce a spectral hole at the frequency of the fixed frequency beam, known as the burning beam. This hole is the one at zero detuning in Fig. 6.3 and is referred to as the spectral hole.

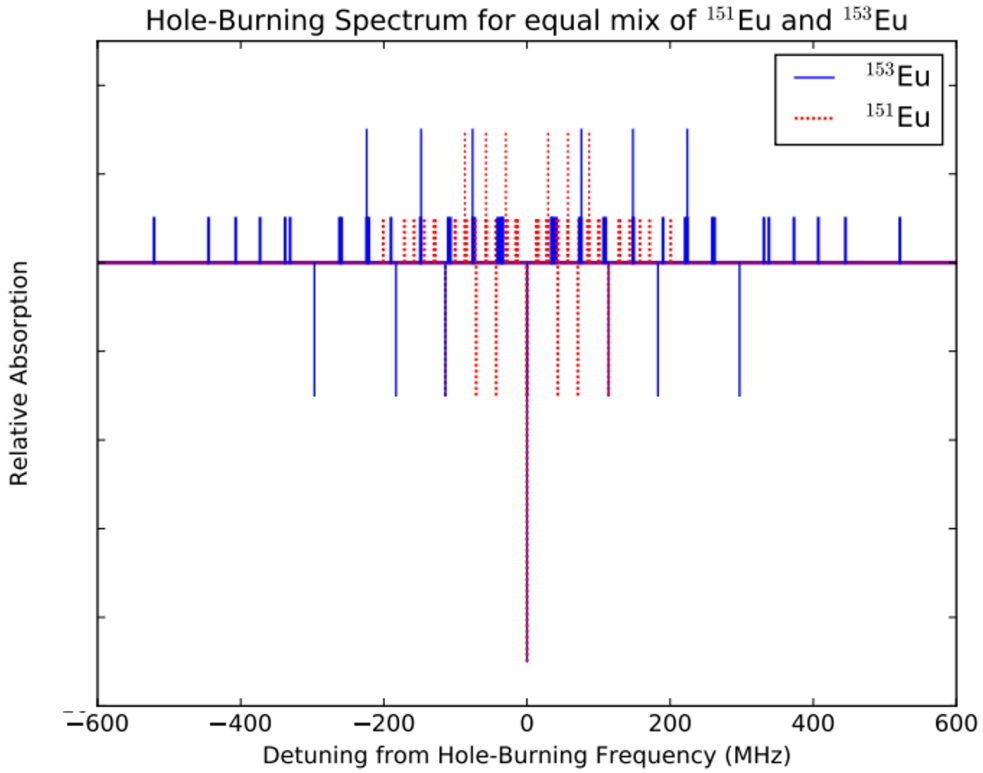

Figure 6.3: All the spectral features produced by a single beam for our crystal with roughly equal amounts of the two stable europium isotopes. The peaks correspond to antiholes and the dips are holes. The larger peaks/dips correspond to spectral features from different ion classes that have the same frequency. This plot assumes equal transition strengths and branching ratios for all transitions and decay paths. If this were not the case, then the holes and antiholes would lose the uniformity according to the relative transition strengths and decay paths [64].

An example of a real spectral hole can be seen in Fig. 6.4. Note that we have been saying spectral hole despite the fact that all of our data shows the spectral holes as peaks. This is because we got use to using the terminology from the literature and never

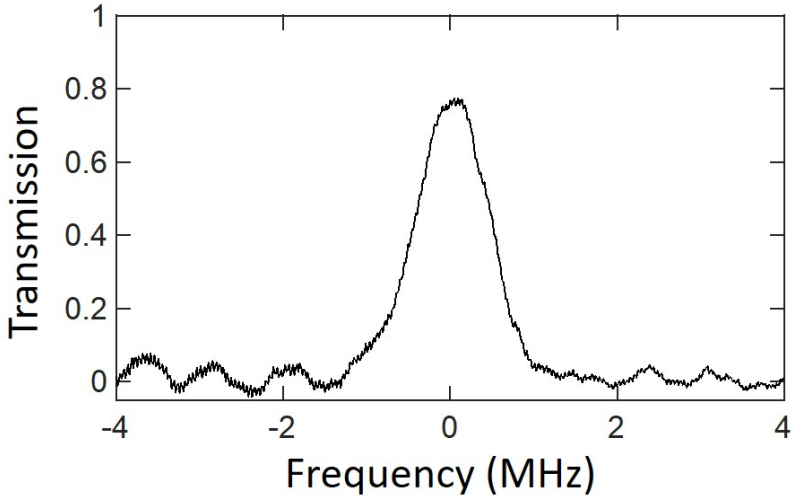

Figure 6.4: Example of the transmission of the spectral hole. Zero detuning corresponds to the frequency of the beam that burned the hole.

bothered to change it. I will continue that tradition throughout this thesis. To produce this figure, a beam, called the burning beam, was turned on at a single frequency. Then, the frequency of a much weaker beam was swept over the hole and the transmission was monitored. In practice these two beams were the same beam, and the power and frequency of the beam was controlled with an AOM.

The depth and width of of the spectral hole can be controlled by the intensity of the burning beam and the burn time. Examples of the variation of the depth and width of the spectral holes versus burn time can be seen in Fig. 6.5. The data in Fig. 6.5 was taken with a burning beam intensity of 40 mW/cm^2. The timescales in the plots can be varied by changing the intensity of the burning beam.

Instead of using a beam with a high intensity or burn for a really long time, broad spectral features can be produced by burning a spectral trough. An example of a spectral trough can be seen in Fig. 6.6. This spectral trough was produced by sweeping the burning beam's frequency over 14 MHz. Although this technique can produce broad spectral features, the width must not extend to the closest antiholes, or else the burn

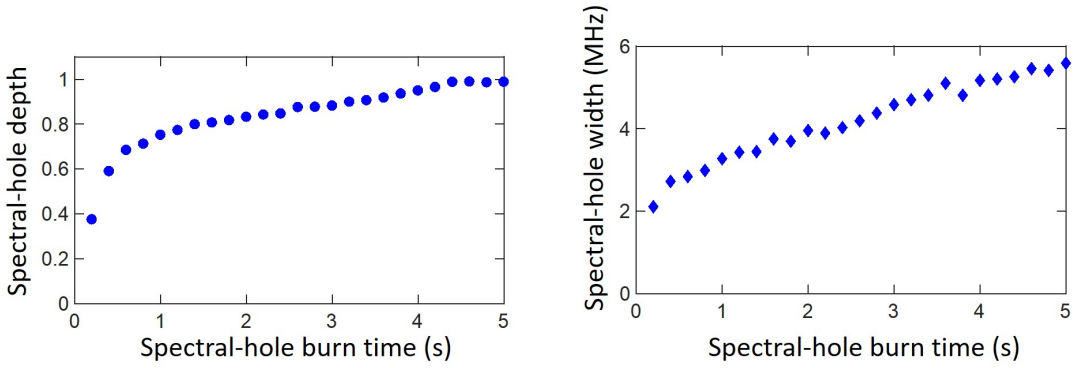

Figure 6.5: The spectral hole depth and width versus burn time. This data was taken with a burning beam intensity of 40 mW/cm^2. The timescales can be changed by changing the intensity of the burning beam.

beam will pump population back into the trough as it sweeps.

Nilsson's Ion Class Selection Procedure

We can go from burning a spectral hole to isolating a single ion class for experiments using a procedure called ion-class selection (ICS) introduced by Nilsson as a way to use rare-earth ions such as Eu:YSO [78] and Pr:YSO [79] in quantum memory applications. In fact, Eu:YSO has had quantum memory protocols demonstrated in it with coherence times of up to six hours [80]. However, the Eu:YSO transition that has been used was the electric dipole $^7F_0 \rightarrow ^5D_0$ transition.

ICS is able to isolate a single ion class by exploiting the fact that none of the hyperfine splittings in an ion class are equal. This means that we can use three beams with the proper frequencies to address a particular ion class. This is depicted in Fig. 6.7 where the beams will be referred to as the probe beam (green), the coupling beam (blue), and the repump beam (red). The naming of the beam is suggestive of the typical names of the beams involved in EIT with the addition of the repump beam to control the population. We can see from Fig. 6.7 that only one ion class has all three ground states addressed by the beams. All the other ion classes have at least one ground state that is

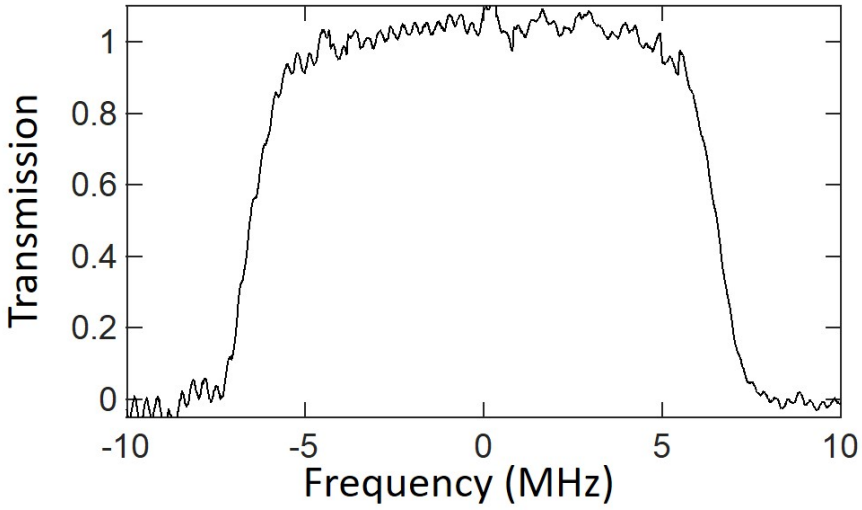

Figure 6.6: An example of a spectral trough. This trough was burned by sweeping the burn beam's frequency over 14 MHz using an AOM.

not addressed. This unaddressed state will accumulate population, taking that ion class out of the picture. In order for this procedure to be successful, there must be at least two of the upper states involved. The particular states we have chosen were chosen so that the probe and coupling beams would share an upper state in preparation for our EIT experiments.

Each of the beams involved in ICS will interact with nine ion classes, many of which are not shown in Fig. 6.7. To check that truly only one ion class is selected, take a look at the tables in Appendix A.3. Consider the coupling beam in Fig. 6.7 which is 76.4 MHz below the probe beam. We can look at the ion class of the spectral features produced by the coupling beam at +76.4 MHz. We can do the same thing for the repump beam. Comparing these two ion classes shows will show that there is a unique ion class selected from the point of view of the coupling beam, and this ion class is the same ion class selected from the point of view of the probe beam or of the repump beam.

Now that we know that selecting an ion class is possible, how do we actually do it? The first step of Nilsson's procedure is to turn all three beams on and sweep out a trough

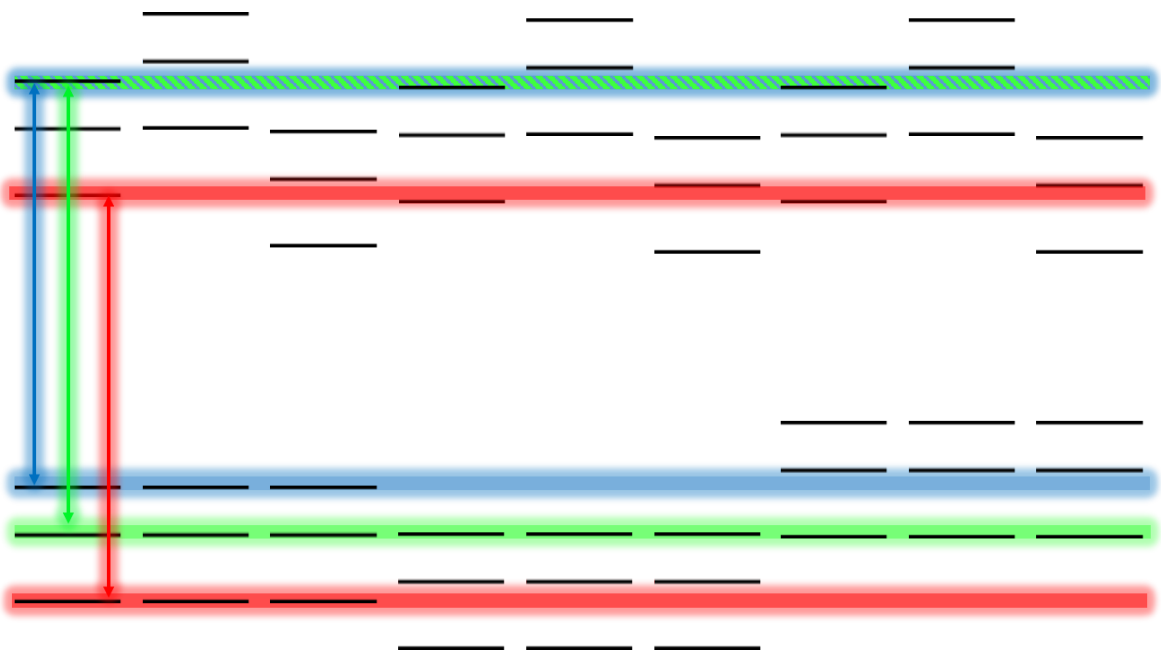

Figure 6.7: The three beams used to select a single ion class. The beams are called the probe beam (green), coupling beam (blue), and repump beam (red). The ion class all the way to the left is the only ion class that has all of its ground states addressed by the beams. All other ion classes have at least one unaddressed ground state that winds up accumulating all the population of that ion class.

with each beam. This step isolates the ion classes over a broader frequency span, thus reducing interference from ion classes that are nearby in frequency. Because all three beams are on at the same time, the population of the selected ion class will be roughly evenly distributed among the three ground states, depending on the beam intensities, transition strengths, and branching ratios.

The second step of Nilsson's procedure involves sweeping the probe and coupling beams while the repump beam is off. This transfers the population in the ground states addressed by the probe and coupling beams to the ground state addressed by the repump beam. The result is a spin polarized state in the ions of the selected ion class.

The last step of Nilsson's procedure is to transfer population from the repump

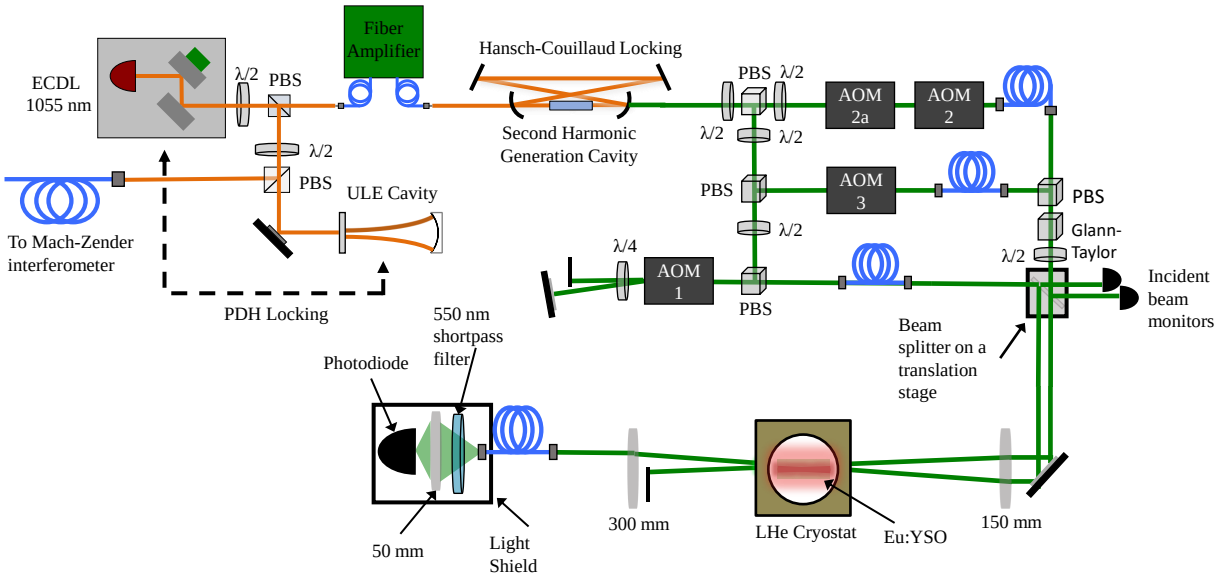

Figure 6.8: The experimental schematic. We begin with a 1055 nm ECDL locked to a ULE reference cavity and whose linewidth is monitored by a Mach-Zender interferometer. The beam is then amplified by a fiber amplifier, and frequency doubled in a PPKTP based ring cavity. The 527.5 nm light output is split into three beams, the probe, coupling, and repump beam. The timing, power, and frequency of the three beams are controlled by AOMs. The coupling and repumper beams are then overlapped while the probe beam propagates parallel to them but displaced by 2 mm. The parallel beams are then focused into the crystal at a small enough angle that they are overlapped within the 1 cm crystal. After the crystal, the coupling and repumper beams are blocked. The probe beam is sent through a fiber into an enclosed box to block scattered light. After leaving the fiber, the probe beam is passed through a 550 nm shortpass filter to block fluorescence from the crystal and then focused onto a photodiode for detection. ECDL: external-cavity diode laser, PBS: polarizing beam splitter, ULE: ultra-low expansion, PDH: Pound-Drever-Hall, AOM: acousto-optic modulator, $\lambda/2$: half-wave plate, $\lambda/4$: quarter-wave plate.

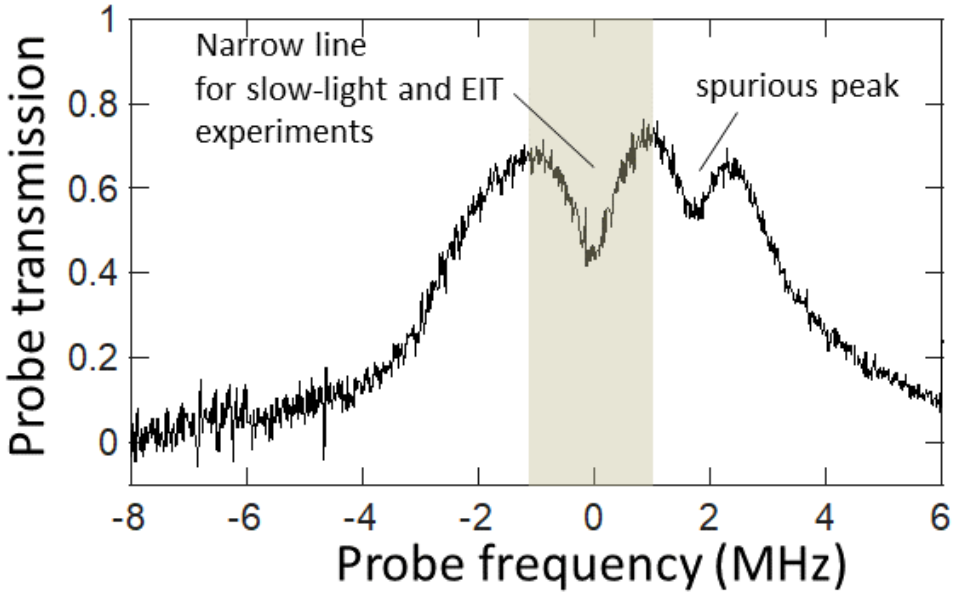

Figure 6.9: The result of Nilsson's ion-class selection procedure; an absorption peak due to a single ion class in a transmission window in the inhomogeneous line. The highlighted peak was then used for EIT and slow light experiments. There is also a spurious peak on the right, suggesting that there might be some unidentified crystal perturbations splitting the probe state.

ground state back to the probe ground state at a single frequency. This is done by turning on the repump and coupling beam at a fixed frequency with the probe beam off. The proper frequency spacing between the repump and coupling beam can be found by considering the spacings between the ground and excited states addressed by each beam.

The experimental setup we used for ion-class selection is shown in Fig. 6.8, and is very similar to the setup we used for Rabi flopping. However, in this setup, the green output from the doubling cavity is split into three beams which we call the probe, the coupling, and the repumper. These three beams are used for ion-class selection, optical pumping, and EIT. Each beam goes through an acousto-optic modulator (AOM) for precise frequency and timing control, which is computer controlled just like the

Rabi flopping experiment. The probe beam AOM uses a double-passed configuration to achieve a wider tuning range of the probe frequency with relatively little variation of its power. Each beam is spatially filtered through a single mode fiber (not shown in Fig. 6.8) before they are combined and focused inside the Eu:YSO crystal. The spot size of the beams at the focus is $W_0 = 45$ μm ($1/e^2$ intensity radius). The probe laser crosses the other two beams at an angle of 15 mrad for ease of detection after the crystal. We use a 10-mm-long Eu:YSO crystal which is housed in a continuous-flow liquid helium cryostat to cool to a temperature of 4.5 K. Cooling is needed to reduce phonon-induced relaxation rates which critically determines homogeneous optical linewidths.

The detectors in Fig. 6.8 are set up to give us absolute transmission for the probe beam. In order to do this, we detuned the laser at the ECDL by several tenths of a nanometer while the cryostat was at 4.5 K in order to get signals on the incident and transmitted probe photodiodes. This gave us a conversion factor between the incident and transmitted beam for 0% absorption by the crystal because all the losses are due to losses from mirrors, lenses, or reflections off of surfaces. We can then use this conversion along with the incident and transmitted signals during the experiment to get the absolute transmission of the probe beam. The photodiodes monitoring the probe beam are high-speed photodiodes in order to capture the details of the short EIT pulses.

The results of Nilsson's procedure can be seen in Fig. 6.9. There we see an absorption peak due to a single ion class in a transmission window. This peak was then used for our EIT and slow light experiments, which are described later in this chapter. Fig. 6.9 also shows a spurious peak to the right of the selected peak. This peak suggest that there are some unidentified perturbations that are splitting the two-fold degeneracy of the probe ground state. I would speculate that this splitting is due to some crystal field mixing, however the origins of this peak will be left for future investigations.

6.2 Manipulating the Magnetic Response Through Nonlinear Optics: Electromagnetically Induced Transparency

6.2.1 Introduction

Electromagnetically induced transparency (EIT) is, like spectral hole burning, is a way to manipulate the susceptibility. However, unlike spectral hole burning, and Rabi flopping for that matter, EIT is a three-level nonlinear process where the susceptibility at the frequency of interest is modified by the presence of a beam at another frequency. The susceptibility modification of EIT is accomplished through interference between different excitation/decay channels that end in the same state.

EIT was first observed by Steve Harris's group in strontium vapor [81] and then lead vapor later that year [82]. These experiments built upon the theoretical work done by Harris's group [83, 84], as well as others' work relating to population trapping [85] and distortion of autoionizing states [86, 87]. Separately, Tewari and Agarwal [88] theoretically studied EIT as a way to enhance nonlinear generation by controlling dispersion and absorption. EIT has since been demonstrated in many systems including rare-earth doped crystals such as Pr:YSO [89, 90] and even Eu:YSO [91] (these experiments used electric dipole transitions).

EIT has several interesting phenomenon associated with it. As we will see in the next section, the EIT susceptibility curve contains very steep slopes. These slopes can result in extremely low group velocities. One the first of these slow light experiments was even able to reduce the group velocity to 17 m/s [92]. These experiments were then pushed even further to produce "stopped" light [93] in which the incident probe pulse is mapped onto a linear combination of two of the EIT states by slowly turning off the coupling beam. The probe beam can be retrieved by slowly turning the coupling beam back on. Stopped light has also been observed in rare-earth doped crystals [94]

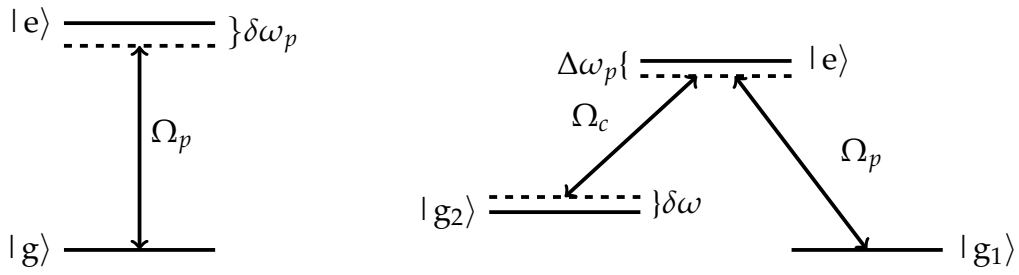

Figure 6.10: On the left we have a two level system interacting with a probe beam with an intensity characterized by a Rabi frequency of Ω_p and detuned from the excited state of ω_p. We can modify the susceptibility of the system at the frequency of the probe beam by adding in another state, denoted by $|g_2\rangle$ on the right, and another beam, called the coupling beam and denoted by Ω_c on the right. $\Delta\omega_p$ is the same single photon detuning as on the left and $\delta\omega$ is the two- photon Raman detuning. Both ground states on the right have nonzero dipole moments with the excited state. However, transitions between the two ground states are forbidden.

and has been explored for use in quantum memory applications [95]. In addition to stopped light, there is also stationary light. Stationary light occurs when there are two counterpropagating coupling beams that set up a standing wave pattern in the system. This standing wave pattern sets up a periodic structure in the material, resulting in photonic bandgaps that can be controlled with the coupling beams. If one of these bandgaps is turned on while the probe pulse is in the system, then the probe pulse can become trapped. Stationary light was first explored theoretically in [96] and then observed in rubidium atoms shortly after [97]. These stationary light pulses can be made to interact with each other [98], and these interactions can be set up in such a way that they can be modeled as Dirac spinors [99, 100, 101].

6.2.2 Theory of EIT

We saw in the two level case that when the beam is turned on the population begins sloshing between the ground and excited states; the system undergoes Rabi flopping. Over time, the decay processes cause the sloshing to settle down and the system approaches a steady state with most population in the ground state and a little bit in the excited state.

Our analysis of two level systems ignored interactions with any other energy levels. However, if we include a third state and a second beam, shown in Fig. 6.10, something interesting happens. The second beam, called the coupling beam, will cause sloshing between the excited state and the third state. This sloshing between the excited state and third state will interfere with the probe beam induced sloshing between the excited state and the first state, resulting in a modification of the response of the system to the probe beam.

The Hamiltonian for the free three level system is

$$\hat{H}_{free} = \begin{pmatrix} \hbar\omega_{g_1} & 0 & 0 \\ 0 & \hbar\omega_{g_2} & 0 \\ 0 & 0 & \hbar(\omega_e - i\Gamma_e/2) \end{pmatrix} \tag{6.1}$$

where Γ_e is the decay rate from the excited state out of the system. The two ground states do not decay, which is a good approximation for the hyperfine levels of our europium ions. The interactions between the two beams and the three level system are given by

$$\hat{H}_{int} = -\hbar \begin{pmatrix} 0 & 0 & B_p\mu_{g_1e}\cos(\omega_p t) \\ 0 & 0 & B_c\mu_{g_2e}\cos(\omega_c t) \\ B_p\mu_{eg_1}\cos(\omega_p t) & B_c\mu_{eg_2}\cos(\omega_c t) & 0 \end{pmatrix} \tag{6.2}$$

where B_p, ω_p, B_c, and ω_c are the magnetic field amplitudes and frequency of the probe

and coupling beam, respectively, and μ_{ij} is the magnetic dipole moment between states i and j. Note that the dipole moment between the two ground states is zero, which is also (approximately) the case in europium ions. When we combine Eqs. 6.1 and 6.2, transform to the interaction picture, and make the rotating wave approximation, we get

$$\hat{H}_{I,RWA} = -\hbar \begin{pmatrix} 0 & 0 & \frac{\Omega_p}{2} \\ 0 & \delta\omega & \frac{\Omega_c}{2} \\ \frac{\Omega_p}{2} & \frac{\Omega_c}{2} & \Delta\omega_p - i\Gamma_e/2 \end{pmatrix} \tag{6.3}$$

where $\Delta\omega_p = (\omega_e - \omega_{g_2}) - \omega_p$ is the single photon detuning between g_1 and the excited state, and $\delta\omega = (\omega_2 - \omega_1) - (\omega_p - \omega_c)$ is the two photon detuning between the two ground states.

Something interesting happens with this Hamiltonian when the beams are resonant. If we take $\Delta\omega_p = \delta\omega = 0$, the eigenvalues and eigenvectors, in the free atom basis, of Eq. 6.3 are

$$\lambda_0 = 0, \quad \begin{pmatrix} \frac{\Omega_c}{\Omega} \\ \frac{-\Omega_p}{\Omega} \\ 0 \end{pmatrix}; \qquad \lambda_\pm = -\frac{i\Gamma}{2} \pm \tilde{\Omega}, \quad \frac{1}{\sqrt{2}} \begin{pmatrix} \frac{\Omega_p}{\lambda_\pm} \\ \frac{\Omega_c}{\lambda_\pm} \\ 1 \end{pmatrix} \tag{6.4}$$

where $\Omega = \sqrt{\Omega_p^2 + \Omega_c^2}$ and $\tilde{\Omega} = \sqrt{-\Gamma^2/4 + \Omega^2}$. In the rotating wave approximation, one of the eigenvalues is zero. The state with this eigenvalue is called the dark state because transitions to the excited state do not occur, rendering a system in this state transparent. This state is a superposition of the two free atom ground states with a set phase relation between them. The particular amplitudes and phases in the dark state are what allow the sloshing discussed above to produce total destructive interference.

We can find the steady state susceptibility using the same method that we used for

the two level system. We first plug Eq. 6.3 into

$$\dot{\rho} = -\frac{i}{\hbar}[H, \rho]. \tag{6.5}$$

After carrying out the matrix multiplication and setting the time derivatives to zero, we make the assumption that the probe beam is weak, or, in other words, the population remains in $|g_2\rangle$ ($\rho_{g_1g_1} \approx 1$, $\rho + g_1g_2 \approx \rho_{ee} \approx 0$). See Appendix C for more details. Solving for ρ_{g_1e} gives us

$$\rho_{g_1e} = \frac{2\delta\omega\Omega_p}{4\delta\omega\Delta\omega_p - 2i\delta\omega\Gamma_e - \Omega_c^2} \tag{6.6}$$

In a real system, there will be dephasing between the two ground states. This dephasing will end up making the destructive interference between the sloshing from the two ground states less efficient and reduce the darkness of the dark state. The dark state will still be dark, but dephasing makes it impossible to completely eliminate absorption. We can incorporate dephasing, and close the system while we're at it, by using

$$\dot{\rho} = -\frac{i}{\hbar}[\hat{H}, \rho] + \sum_i \Gamma_i D[c_i]\rho \tag{6.7}$$

instead of Eq. 6.5, where the sum is over all the decay channels. D is known as the Lindblad superoperator, an operator that acts on operators, and can be expressed as

$$D[c]\rho = c\rho c^\dagger - \frac{1}{2}\{c^\dagger c, \rho\} \tag{6.8}$$

The c's are operators that can represent dephasing or are operators that cause population that has decayed to be added back into the system (Appendix C). If we make the same assumptions about EIT that we did before ($\rho_{g_1g_1} \approx 1$, $\rho_{g_2g_2} \approx \rho_{ee} \approx 0$) and follow the steps in Appendix C to solve for the steady state solution for ρ_{g_1e}. The result is very

similar to Eq. 6.6 except $\delta\omega$ is replaced with $\delta\omega - i\gamma_{g_2}/2$, where γ_{g_2} is the dephasing rate of $|g_2\rangle$, and Γ_e is replaced by $\gamma_e = \Gamma_{eg_1} + \Gamma_{eg_2} + \Gamma_e$, where Γ_{ei} is the decay rate from $|e\rangle$ to ground state i and Γ_e is the dephasing rate of $|e\rangle$. Putting all this together gives us the coherence between $|g_1\rangle$ and $|e\rangle$

$$\rho_{g_1 e} = \frac{2\delta\omega\Omega_p - i\gamma_{g_2}\Omega_p}{4\delta\omega\Delta\omega_p - \gamma_{g_2}\gamma_e - \Omega_c^2 - 2i(\gamma_{g_2}\Delta\omega_p + \delta\omega\gamma_e)}. \tag{6.9}$$

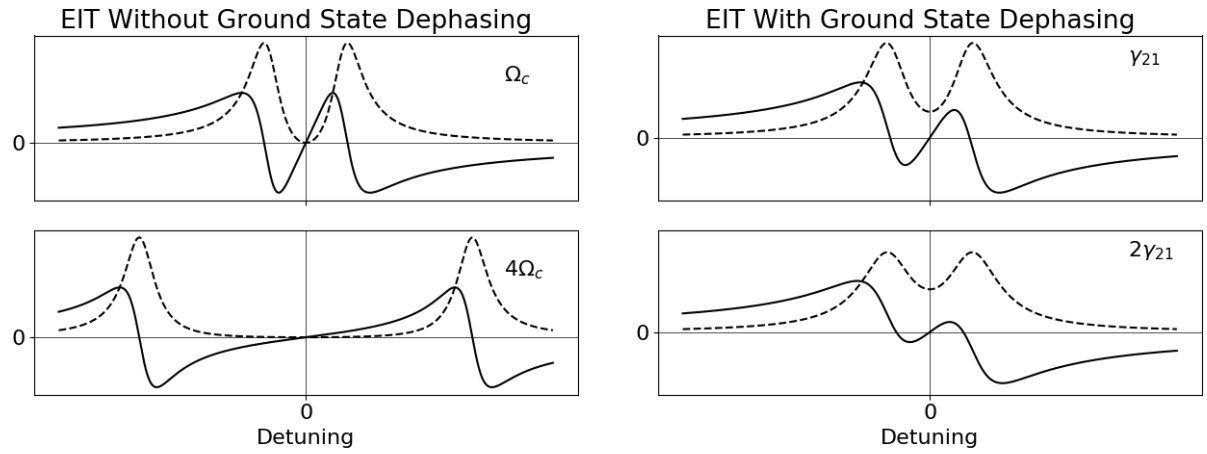

Figure 6.11: Examples of the EIT susceptibility with no ground state dephasing and different coupling beam Rabi frequencies (left) and the same coupling beam Rabi frequency but different ground state dephasing (right). The dashed lines are the imaginary parts of the susceptibility and the solid lines are the real parts. The dip in the imaginary part at zero detuning corresponds to an increase in transparency. The steep slope in the real part is what causes slow light.

Fig. 6.11 shows the significant ways in which the EIT susceptibility depends on the coupling beam Rabi frequency and the dephasing rates. The left two plots show that the main effect of the coupling beam is to split the two level susceptibility into two peaks. Analogies have been drawn between this splitting and the splitting that occurs when two classical oscillators are coupled together. This analogy has been used to come up with

examples of "classical EIT" [102]. There are two important take aways from the effects of the coupling beam intensity. One is that, at zero detuning, the imaginary part of the susceptibility goes to zero, which results in the absorption of the probe beam going to zero as well. Although in our discussion of the dark state we set both $\Delta\omega_p$ and $\delta\omega$ to zero, it can be shown that zero absorption only requires that the two photon detuning be zero. Typically, EIT experiments are carried out by fixing the frequency of the coupling beam and sweeping the probe frequency. This sets a fixed relationship between $\Delta\omega_p$ and $\delta\omega$ which is typically tuned so that the single and two photon detunings are zero at the same probe frequency.

The other important take away from the left side of Fig. 6.11 is the steepness of the real part of the susceptibility at zero detuning. As we discussed earlier, the group velocity of a wave packet depends on the slope of the index of refraction. The steepness of the real part of the susceptibility and the lack of absorption around this steep section has been used for coherent slow light experiments. The slowness of the light can be controlled by changing the coupling beam intensity. As the intensity of the coupling beam decreases, the steepness of the real part of the susceptibility increases and the slower the packet will move. Of course, as the coupling beam intensity decreases, the transmission window decreases as well, limiting the possible bandwidth of the slow moving packet. However, reducing the couping intensity until it reaches zero has been used to "stop" light. In these stopped light experiments, the state of the probe beam is mapped onto $|g_2\rangle$ as the coupling beam is slowly turned off (see Eq. 6.4 as $\Omega_c \rightarrow 0$). The information can be retrieved by turning the coupling beam back on. Slow/stopped light has been incorporated into quantum memory protocols.

The important take away from the right side of Fig. 6.11 is that dephasing between the two ground states reduces the darkness of the dark state. The more dephasing there is the more absorption of the probe beam will be observed. In any real system, there will be dephasing between the ground states, including Eu:YSO, and this will be one of

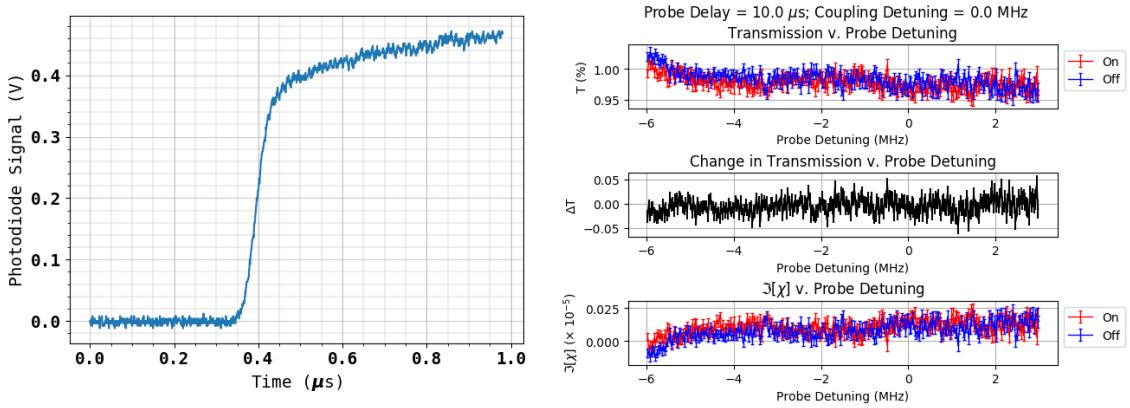

Figure 6.12: The turn-on time of the probe AOM (left) and the background noise on the probe signal due to the coupling beam (right). The background measurement was done by recording the probe signal with the coupling beam on and off. These measurements were taken at room temperature to avoid any influence from the sharp cryogenic transitions.

the limitations of our EIT experiments.

Adiabatic Turn On

The typical starting point for an EIT experiment has the population of the system in $|g_1\rangle$. To successfully observe EIT, one must get from the state $|g_1\rangle$ to the dark state. If the two beams are suddenly turned on, the components of $|g_1\rangle$ that overlaps with the bright states (the two states in Eq. 6.4 that are not the dark state) will undergo Rabi flopping until these states decay into the dark state and EIT is observed.

A quicker, more efficient way to get to the dark state starts with turning on the coupling beam by itself. By finding the eigenvectors and eigenvalues of Eq. 6.3 under these conditions, we would find that one of the eigenvectors is the same as $|g_1\rangle$. This is known as coherent population trapping. By slowly turning on the probe beam, the system will adiabatically transition from the coherently trapped state to the EIT dark state. This adiabatic process is aided by the fact that the probe beam is weak. Despite having to

turn on the probe beam slowly, this process is typically faster than waiting several decay times for the Rabi oscillations of the bright states to die away. See Appendix C for more details about adiabatic turn on.

6.2.3 EIT Experiment

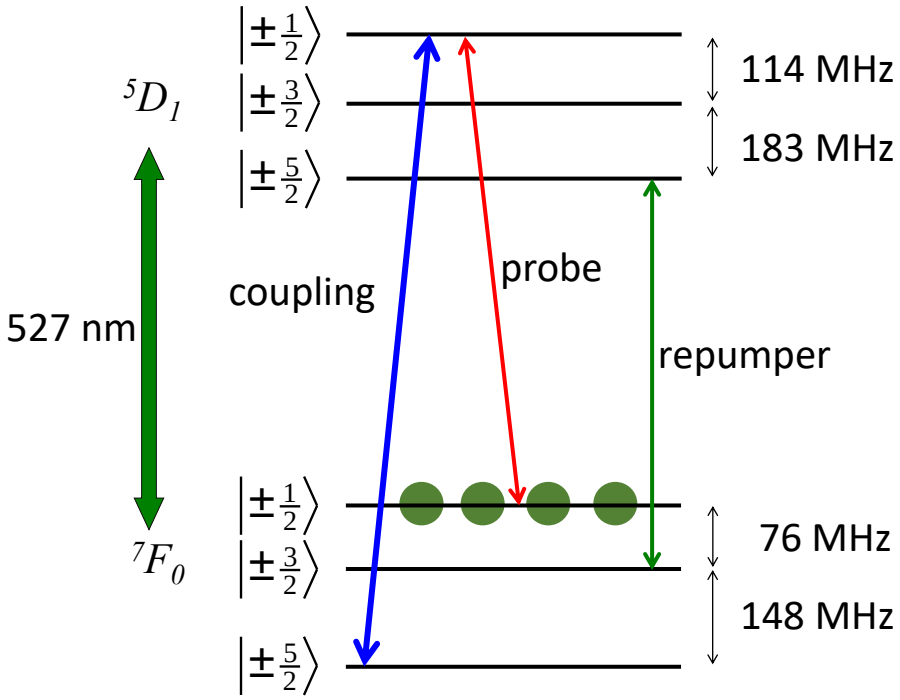

Figure 6.13: The energy levels and beams that we used for our EIT experiment. The ordering of the upper hyperfine splittings is not known.

The setup in Fig. 6.8 was also used for our EIT experiment and the energy levels involved can be seen in Fig. 6.13. In order to successfully observe EIT, the rise time of the probe AOM cannot exceed the limit required for adiabatic turn on. The rise time of the AOM is shown on the left side of Fig. 6.12. There we see that the probe beam's steepest rise takes place over about 75 ns when the power rises by about 60 % of the maximum value. The power in the probe beam was about 30 μW and that of the coupling beam was 23 mW. Taking these values and using C.28, we see that the probe beam rise time is 4-5

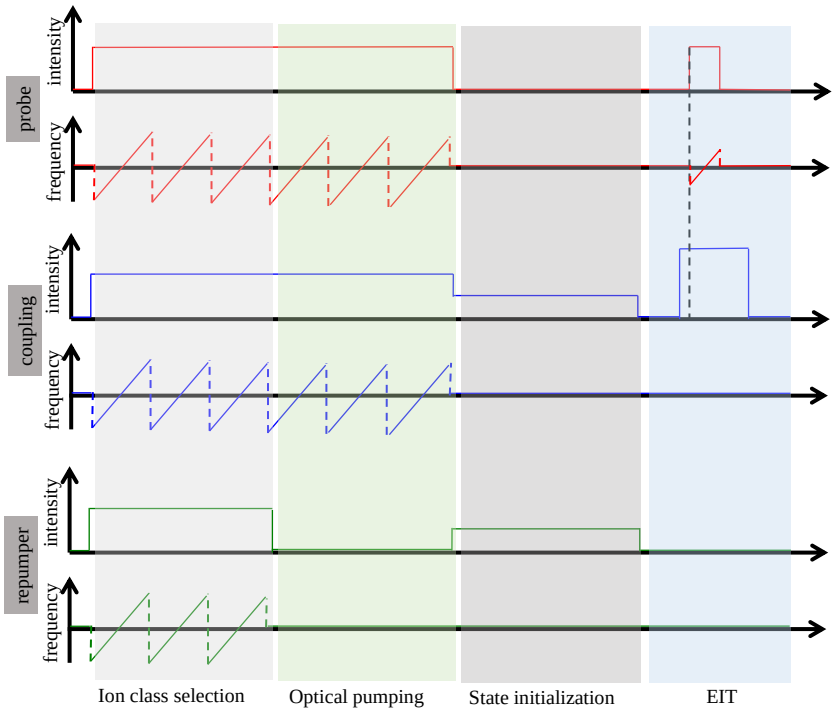

Figure 6.14: The pulse sequence used for EIT. The x axis is not to scale; Nilsson's procedure, which constitutes the first three sections (ion class selection, optical pumping and state initialization) take on the order of 1 minute, and the EIT section takes on the order of 100 μs. This pulse sequence was repeated many times to obtain an average signal.

times larger than the lower limit, allowing us to observe EIT.

The right side of Fig. 6.12 shows the background due to the coupling beam on the probe signal. The probe signal is small to begin with, and on top of that we are looking for a relatively small change in that signal. In order to be able to observe this small change, we need to make sure that the coupling beam background on the probe signal is small enough so that it doesn't was out the EIT signal. In Fig. 6.12, we see that the probe signal with the coupling beam on (red data) is right on top of the probe signal with the coupling beam off (blue data). In addition, the difference between these two signals is approximately constant across the frequency range we are looking at.

For EIT, with the ions selected and initialized to the $|\pm 1/2\rangle$ hyperfine state, we turn

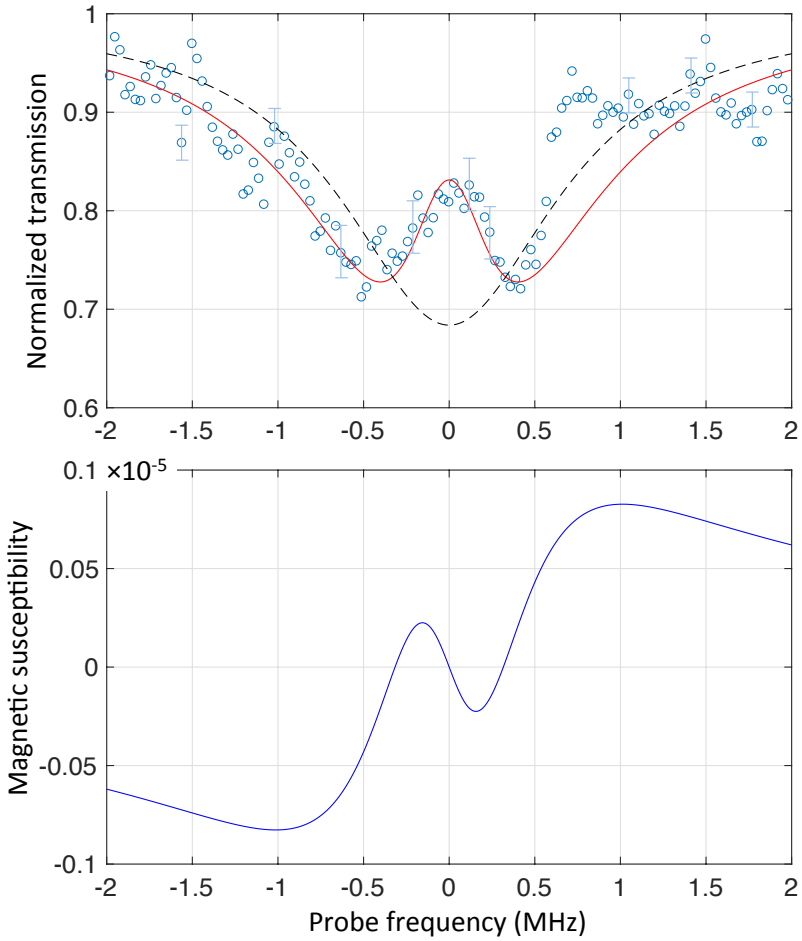

Figure 6.15: Normalized probe transmission with the coupling laser beam (shown as data points) and without it (shown as a dashed line). With the coupling laser, there is splitting of the line (Autler-Townes splitting), with slight but observable increase in the transmission at line center. The solid red line is a fit to the data points using the well-known EIT-lineshape. The bottom plot is the calculated real part of the magnetic susceptibility under the conditions of EIT.

on both probe and coupling laser pulses. To allow adiabatic preparation of the dark state, we turn on the coupling laser beam before the probe, and then measure the transmission of a weak probe laser pulse through the crystal. Similar to the transmission experiment of Fig. 6.9, we use a 40-μs-long probe laser pulse, and chirp the probe frequency during the pulse so that the whole frequency response is obtained in a single experiment. The full pulse sequence for a single EIT shot is shown in Fig. 6.14.

Fig. 6.15 shows normalized probe transmission with and without the coupling laser beam. As expected, with the coupling laser, there is a splitting of the line (Autler-Townes splitting), with slight but observable increase in the transmission at line center. The solid red-line is a fit to the data points using the well-known EIT-lineshape for the susceptibility [103]:

$$\chi_M = \frac{N\mu^2}{\epsilon_0 \hbar} \frac{\delta\omega + i\gamma}{(\delta\omega + i\gamma + i\Gamma/2)(\delta\omega + i\gamma) - |\Omega_C|^2} \quad . \tag{6.10}$$

Here, we have taken the coupling laser beam to be exactly resonant between the relevant levels. Γ is the population decay rate of the excited level, and γ is the dephasing rate between the two ground hyperfine states. The quantity $\delta\omega$ is the frequency detuning of the probe laser beam from the excited level (which is also the two photon Raman detuning since the coupling laser is assumed to be resonant), and Ω_C is the Rabi frequency of the coupling laser beam. The best fit gives a coupling laser Rabi frequency of $\Omega_C = 2\pi \times 350$ kHz and a Raman dephasing rate of $\gamma = 2\pi \times 150$ kHz. The physical mechanism for this large Raman dephasing rate is currently an open question.

The bottom plot in Fig. 6.15 is the calculated change in the real part of the magnetic susceptibility due to EIT. We can modify the real part of χ_M by $\approx 10^{-6}$. These experiments extend previous EIT and quantum coherence experiments that were observed in rare-earth doped crystals to interactions with the magnetic field of light.

The data of Fig. 6.15 is obtained using a coupling laser power of 23 mW (beam

intensity of 723 W/cm^2 at the focus). Using the inferred value of the coupling laser Rabi frequency from the fit ($\Omega_C = 2\pi \times 350$ kHz), we calculate the magnetic-dipole matrix element for the specific hyperfine transition to be $\mu = (0.10 \pm 0.01)\mu_B$ (μ_B is the Bohr magneton). This is reasonably consistent with the hyperfine-averaged matrix element measurements of our previous Rabi flopping experiments [70].

6.3 Slow Light

Using the selected ensemble, we have been able to observe linear group velocity reduction. Fig. 6.16(a) shows the propagation of a 1/4 μs-long probe laser pulse whose frequency is detuned by 0.8 MHz from the peak of the narrow absorption resonance. In addition to significant reshaping of the pulse, we observe a group delay of 127 ns while propagating through the crystal. This group delay corresponds to a group velocity of $v_g = 7.8 \times 10^4$ m/s, which is 3800 times slower than the speed of light in free space. Note that this group delay is not that which is typically associated with EIT. Rather, it is due to the large dispersion of the two level linear transition. We also performed this slow-light experiment with 5 μs pulses. Fig. 6.16(b) shows that there is much less distortion to the longer pulse. This and the longer delay time are likely due to the narrower bandwidth of the longer pulse. To our knowledge, this is the first observation of group velocity reduction using interaction with the magnetic field of light.

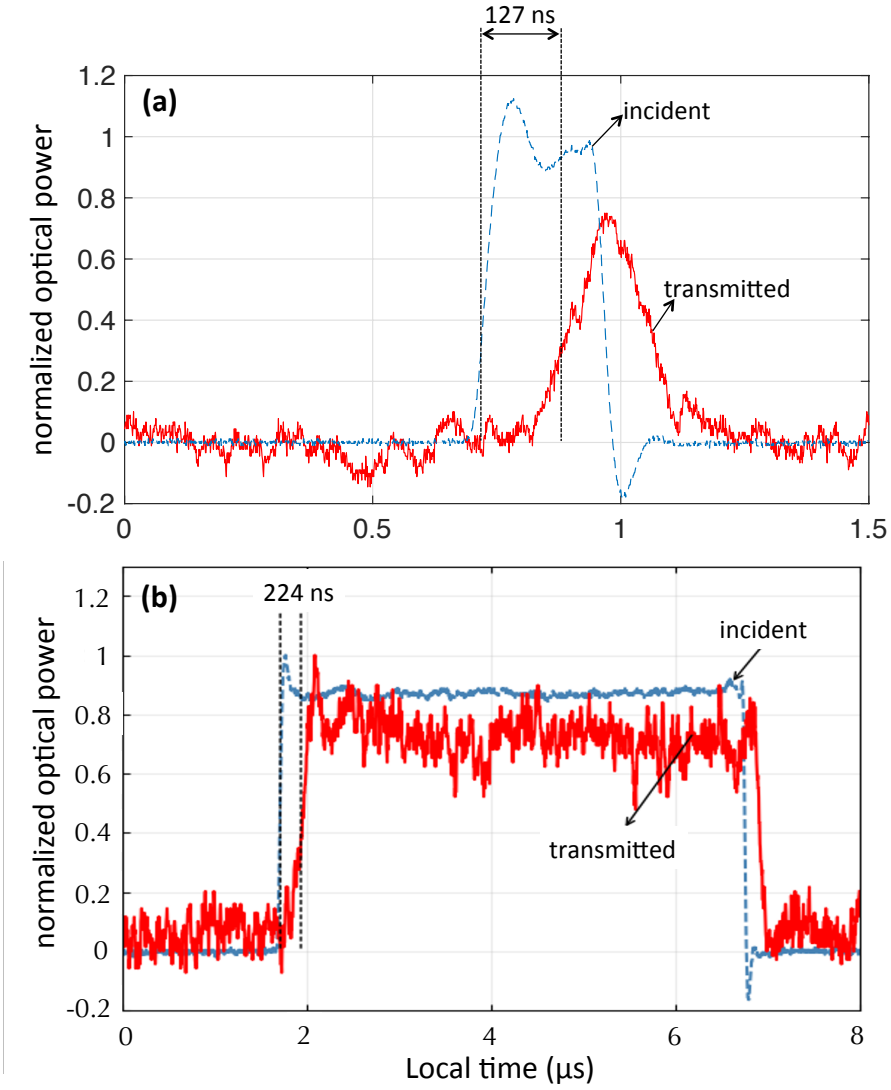

Figure 6.16: (a) The propagation of a 1/4 μs-long probe laser pulse whose frequency is detuned by 0.8 MHz from the narrow absorption resonance. We observe a group delay of 127 ns while propagating through the crystal, corresponding to a group velocity of $v_g = 7.8 \times 10^4$ m/s$\approx c/3800$.

(b) The propagation of a 5 μs-long probe pulse with the same detuning. The longer pulse shows little distortion, however we consistantly observed longer delays for the longer pulses. This is likely due to the narrower bandwidth of the longer pulses.

Chapter 7

Future Work

7.1 Host Crystal

We have shown that Eu:YSO has a magnetic response at optical frequencies and we have shown that this response can be manipulated. The next steps will then be to determine what sort of electric response can be added in in order to implement our externally driven scheme. This scheme laid out in [34, 69] acquires its electric response from the nonlinear electric response of the host crystal.

Because large magnetic responses are so rare at optical frequencies, the focus at the beginning of this project was on the magnetic response. This lead us to Eu:YSO, which was expected to have a large magnetic response and had previous work to build on. Unfortunately, YSO is not conducive to the second harmonic generation required for the externally driven scheme. For second harmonic generation to be possible, the crystal must have a nonzero second order susceptibility $\xi^{(2)}$. Similar to selection rules for atomic transitions, we can use the symmetry of the crystal to determine which elements of the second order susceptibility tensor will be zero or nonzero. If the crystal's symmetry group contains an inversion center, i.e. if the crystal is centrosymmetric, then all the elements of the second order susceptibility tensor will be zero and there will be no

second harmonic generation [104]. Unfortunately, YSO is centrosymmetric.

Our first idea to work around the lack of second order response was to produce what are known as electric field induced second harmonics, or EFISH. This method creates an effective second order response out of the third order response. By using a DC field as one of the three fields in the third order response, the inversion symmetry of the crystal is broken. This effective second order response can be written as

$$\chi^{(2)}_{eff}(2\omega) = \chi^{(3)}(2\omega;\omega,\omega,0)E_{DC}. \tag{7.1}$$

This response would then generate second harmonic light with an intensity of

$$I = \frac{4(\chi^{(2)}_{eff})^2(2\omega)^2 I^2_{fund} L^2}{n_1 n_2 n_3 \epsilon_0 c^3} \tag{7.2}$$

where L is the length of the crystal, I_{fund} is the intensity of the fundamental beam with frequency ω, and n_i are the principle indices of refraction for the anisotropic crystal [104]. Unfortunately, with a typical third order response and a reasonable amount of power in the fundamental beam (even the 10 W output of our fiber amplifier), EFISH does not result in a practical level of polarization.

Another, more promising approach would be to simply use another host crystal. We have seen that, despite having all crystal field parameters nonzero, YSO's crystal field perturbation on the europium dopant does not ruin the magnetic nature of the $^7\mathrm{F}_0 \rightarrow ^5\mathrm{D}_1$ transition. Since the crystal field parameters of different crystals are typically of the same order, we could reasonably expect that just about any other host crystal would preserve the magnetic nature of our transition of interest. This opens up the possibility of using a different host crystal with an inversion center.

Another benefit of switching to another host crystal is the possibility of switching to what is known as a stoichiometric crystal. Although rare-earth doped crystals have very small inhomogeneous broadenings when compared to other solids, the fact that the

inhomogeneous line is much broader than the homogeneous line results in a substantial reduction in the effective density of dopant ions. owever, it has been demonstrated that using rare earths in these stoichiometric crystals can result in inhomogeneous linewidths as narrow as 25 MHz [105]. Thus, if our laser beam were to address all ions within 1 MHz of line center, then a stoichiometric crystal would allow us to address a substantially higher density of ions than a standard doped crystal, assuming the total ion concentrations are the same.

7.2 Eu

In order to refine our measurements and better plan out future experiments, it will be useful to have a better understanding of europium's hyperfine structure in YSO. One way to accomplish this is through a method known as Raman-heterodyne spectroscopy [106, 63].In Raman-heterodyne spectroscopy, the hole burning laser beam is accompanied by a variable frequency RF field. The frequency of the RF field is swept over the inhomogeneous linewidth. At specific frequencies corresponding to the hyperfine splittings of the ground or excited states, the RF and optical beams will be tuned to a two-photon resonance and Raman scattering will occur. The Raman generated optical light is then detected on a high-speed detector along with the incident optical light, and the beam frequency between the two can be used to indicate Raman resonance. Such a technique can be used to identify the ordering of the upper state hyperfine splitting. It would also provide us a way to probe the hyperfine structure in a way that would allow us to study the spurious peak shown in Fig. 6.9.

In addition to identifying the order of the upper state splittings Raman-heterodyne spectroscopy can be used to measure other properties of the hyperfine states. Longdell

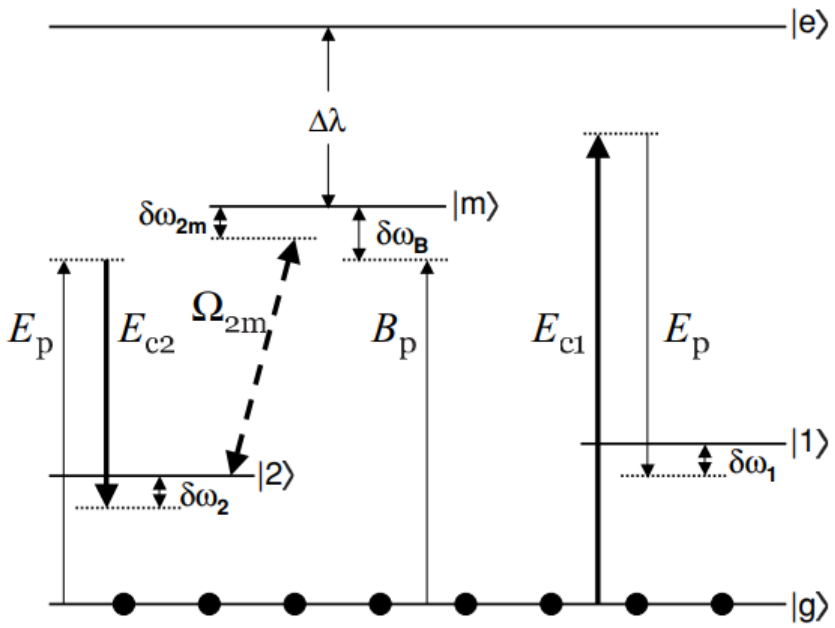

Figure 7.1: The energy level diagram and fields of the chirality scheme.

[106] models the static hyperfine interactions as

$$H = \vec{B} \cdot \mathbf{M} \cdot \vec{I} + \vec{I}\mathbf{Q}\vec{I} \tag{7.3}$$

where $\vec{B}$ is an external magnetic field, $\vec{I}$ is the nuclear spin vector, $\mathbf{M}$ is an effective Zeeman tensor, and $\mathbf{Q}$ is an effective quadrupole tensor. By adding Helmholtz coils to our experiment and measuring the Raman-heterodyne spectrum as the magnitude and direction of the magnetic field are varied, we can determine all the parameters of $\mathbf{M}$ and $\mathbf{Q}$ as well as their orientation. This information can then be used to find the calculate the mixing of the eigenstates of the nuclear magnetic moment operator as well as transition amplitudes between ground and excited hyperfine states.

7.3 Tb

Another future direction for the project could be to investigate the feasibility of implementing the chirality scheme in a terbium doped crystal. According to Cowan's code, the $^7F_6 \rightarrow ^5F_5$ transition in Tb has a larger magnetic dipole reduced matrix element than the $^7F_0 \rightarrow ^5D_1$ transition in Eu. In addition, the $4f7\ 5d1$ configuration of Tb is closer in energy to the $4f8$ configuration than the $4f5\ 5d1$ configuration in Eu is to the $4f6$. If we are able to use this transition to produce a negative index of refraction, it would be the shortest wavelength, 282 nm, at which a negative index was observed by a fairly large margin.

At the core of the chirality scheme is the idea of coupling together the electric and magnetic responses, altering the polarization and magnetization:

$$P = \epsilon_0 \chi_E E + \frac{\xi_{EB}}{c\mu_0} B \tag{7.4}$$

$$M = \frac{\xi_{BE}}{c\mu_0} E + \frac{\chi_M}{\mu_0} B \tag{7.5}$$

where the ξ are the magneto-electric cross-coupling coefficients. A system with this sort of cross-coupling will have an index of refraction

$$n = \sqrt{\epsilon\mu - \frac{(\xi_{EB} + \xi_{BE})^2}{4}} + \frac{i}{2}(\xi_{EB} - \xi_{BE}). \tag{7.6}$$

See Dan Sikes's thesis for a detailed derivation [37]. By coherently adjusting the χ's and the ξ's, we can obtain a negative index of refraction with a much weaker magnetic response than we would need with no cross-coupling [38, 39].

The response of the chirality scheme can be expressed in terms of the following four

paramters [35, 36]

$$\alpha_{EE} = 2\hbar a_p + \frac{\hbar|b_1|^2|E_{C1}|^2}{\delta\omega_1 + i\gamma_1} + \frac{\hbar|b_1|^2|E_{C1}|^2}{\left(\delta\omega_2 - i\gamma_2 - \frac{|\Omega_{2m}|^2}{4(\delta\omega_B - i\gamma_m)}\right)} \tag{7.7}$$

$$\alpha_{BB} = \frac{|\mu_{gm}|^2}{\hbar(\delta\omega_B - i\gamma_m)} + \frac{|\mu_{gm}|^2}{4\hbar(\delta\omega_B - i\gamma_m)^2\left(\delta\omega_2 - \frac{|\Omega_{2m}|^2}{4(\delta\omega_B - i\gamma_m)} - i\gamma_2\right)}|\Omega_{2m}|^2 \tag{7.8}$$

$$\alpha_{EB} = \frac{b_2\mu^*_{gm}}{(\delta\omega_B - i\gamma_m)\left(\delta\omega_2 - i\gamma_2 - \frac{|\Omega_{2m}|^2}{4(\delta\omega_B - i\gamma_m)}\right)}\Omega_{2m}E_{C2} \tag{7.9}$$

$$\alpha_{BE} = \frac{b^*_2\mu_{gm}}{(\delta\omega_B - i\gamma_m)\left(\delta\omega_2 - i\gamma_2 - \frac{|\Omega_{2m}|^2}{4(\delta\omega_B - i\gamma_m)}\right)}\Omega^*_{2m}E^*_{C2}. \tag{7.10}$$

These parameters can be combined along with

$$\kappa = 1 - N\frac{1}{3\epsilon_0}\alpha_{EE} - N\frac{\mu_0}{3}\alpha_{BB} - N^2\frac{\mu}{9\epsilon_0}(\alpha_{EB}\alpha_{BE} - \alpha_{EE}\alpha_{BB}) \tag{7.11}$$

to give the susceptibilities and cross-coupling coefficients

$$\chi_E = N\frac{1}{\kappa\epsilon_0}\left(\alpha_{EE} + \left[N\frac{\mu_0}{3}(\alpha_{EB}\alpha_{BE} - \alpha_{EE}\alpha_{BB})\right]\right) \tag{7.12a}$$

$$\chi_M = N\frac{\mu_0}{\kappa}\left(\alpha_{BB} + \left[N\frac{1}{3\epsilon_0}(\alpha_{EB}\alpha_{BE} - \alpha_{EE}\alpha_{BB})\right]\right) \tag{7.12b}$$

$$\xi_{EB} = N\frac{\mu_0 c}{\kappa}\alpha_{EB} \tag{7.12c}$$

$$\xi_{BE} = N\frac{\mu_0 c}{\kappa}\alpha_{BE} \tag{7.12d}$$

where κ and the terms in square brackets are the local field corrections.

The detuning terms $\delta\omega$ in the α parameters include AC Stark shifts induced by the

intense beams E_{c1} and E_{c2}. It is assumed that the beams can be adjusted such that the Raman Stark shifts can be compensated for and so that $\delta\omega_B = \delta\omega_2 = -\delta\omega_1$.

The linewidths, represented by the γ's, also contain effects from the intense Raman beams. They are each broadened by a factor of

$$\Im\left[\frac{C|E|^2}{2}\right] \tag{7.13}$$

where C is the Raman coupling coefficient, represented by a_p, b_1, and b_2 in the α parameters, and is given by

$$C = \frac{1}{2\hbar^2}\sum_e \frac{d_{ge}d_{ef}^*}{\omega_{ge} - \omega_p - i\Gamma_e}. \tag{7.14}$$

The sum in Eq. 7.14 is over all the excited states involved in the Raman transition. In the case of terbium, this sum would be over the states of the excited configuration. ω_{ge} is the frequency of the electric dipole transition to the excited configuration, ω_p is the frequency of the probe beam, Γ_e is the unbroadened linewidth of the excited state, d_{ge} is the dipole moment between the ground and excited state, and d_{ef} is the dipole moment between the excited state and the final state, which might be $|g\rangle$, $|1\rangle$, or $|2\rangle$. All of the information needed to compute Eq. 7.14, except for the probe frequency, is outputted by Cowan's code.

7.3.1 Implementation in Tb

The lowest energy levels of Tb^{3+} are shown in Fig. 7.2. On the left are all the energy levels below 100000 cm $^{-1}$ above the ground state. The excited configuration is shown in red. This Figure shows that, although most of the excited configuration states are very far detuned from the ground state, there are a few outliers that are relatively low energy when compared to Eu^{3+}. On the right are the lowest few energy levels of the ground

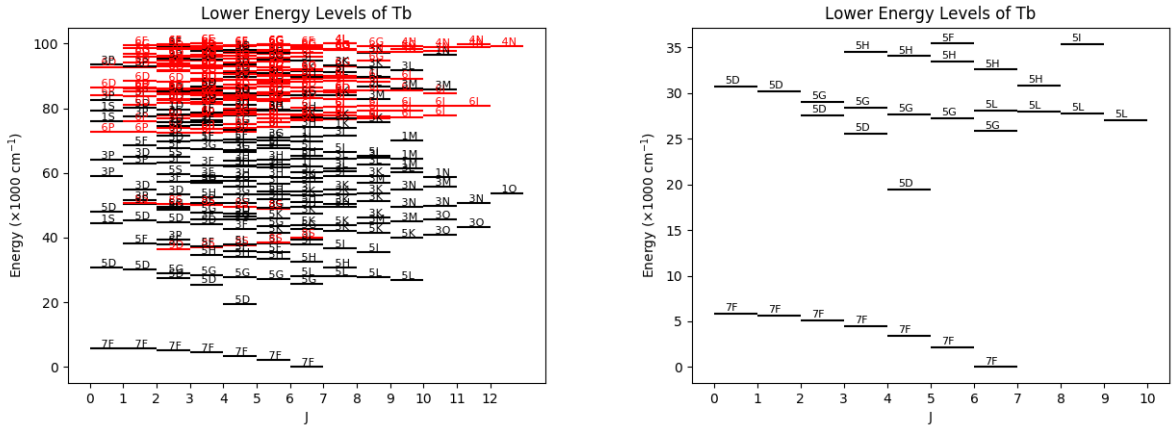

Figure 7.2: The lowest levels of the free terbium ion calculated with Cowan's code.Energy levels below 100000 cm^{-1} for the free terbium ion calculated with Cowan's code. The $4f^8$ configuration states are black and the $4f^7 5d^1$ configuration states are shown in red.

configuration. The states we are interested in are the $^7\text{F}_6$ and $^5\text{F}_5$ states.

Implementation of the chirality scheme in Tb is shown in Fig. 7.3. The magnetic transition would be between the $^7\text{F}_6 \rightarrow ^5\text{F}_5$ transition with a wavelength of 282 nm. Based on the output of Cowan's code (not including any crystal field mixing), the magnetic dipole moment is $\mu = -0.09\mu_B$. The highly detuned electronic states that will be used as the upper state in the Raman transitions, corresponding to state $|e\rangle$ in Fig. 7.1, are the states of the $4f^7 5d^1$ configuration. The relevant Raman coefficients are assumed to be the same and are $C = 3.6 \times 10^{-6} + 6.0 \times 10^{-12} i$, also based on calculations from Cowan's code. The lower states of the Raman transition, states $|1\rangle$ and $|2\rangle$ in Fig. 7.1, would be hyperfine states of the $^7\text{F}_6$ state.

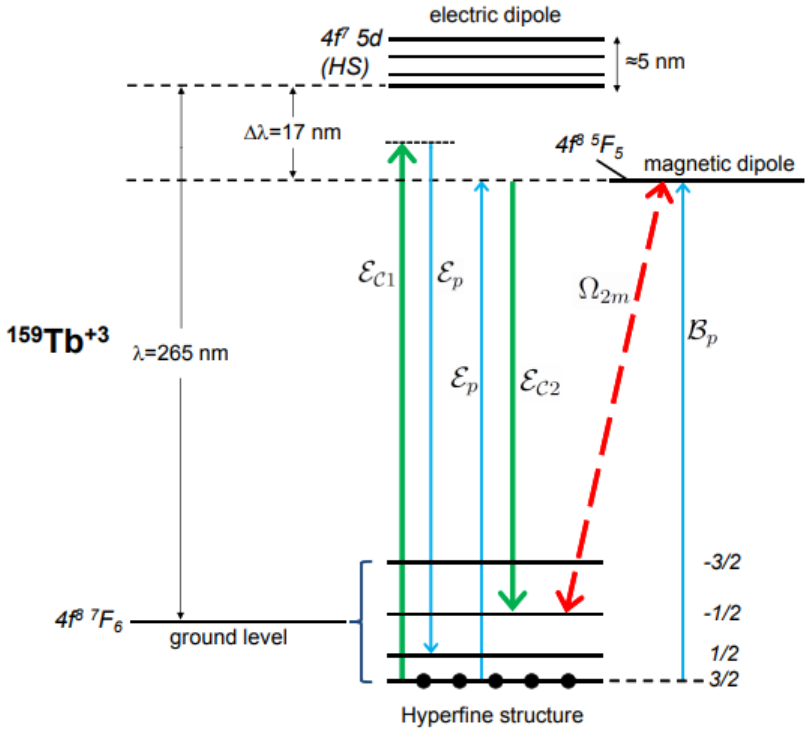

Figure 7.3: Our chirality scheme from Fig. 7.1 implemented in terbium ions, Tb^{+3}. The states of the $4f^7 5d^1$ configuration take the place of $|e\rangle$, states $|1\rangle$ and $|2\rangle$ are hyperfine states of the $^7F_6$ state, and the $^7F_6 \rightarrow {}^5F_5$ at 282 nm takes the place of the magnetic transition. Image taken from [37].

In order to run a realistic simulation, we must include an inhomogeneous broadening, as was done in [35, 36]. However, the dipole moments and Raman coefficients used in those references are larger than those of terbium and allow for lower ionic densities and broader inhomogeneous linewidths. Unfortunately, for rare-earth doped crystals, in order to get an inhomogeneous linewidth small enough to implement the chirality scheme, we would need to use very low densities [107, 108, 109]. However, rare-earth ions in what are called stoichiometric crystals are known to have very narrow inhomogeneous broadenings, on the order of 25 MHz, at very high densities, around 4×10^{27} m^{-3} [105, 110].

For the simulations presented here, we use the parameters mentioned above obtained

from Cowan's code, along with an inhomogeneous linewidth of 25 MHz and a terbium density of 4×10^{27} m^{-3}. The linewidth of the upper Raman state was set to 322 MHz (also from Cowan's code). There is also an inhomogeneous broadening associated with the hyperfine states that must be taken into account. These broadenings don't have much of an impact on our previous work because they are typically much smaller than the optical inhomogeneous linewidth [111, 112, 113]. However, for our chirality scheme simulations, we set the hyperfine, or Raman, inhomogeneous broadening to 50 kHz. Our beam intensities are $I_{C1} = 11.175$ MW/cm^2, $I_{C2} = 18$ MW/cm^2, and $\Omega_{2m} = 2\pi \times 2.5$ MHz.

An example index versus frequency sweep using these parameters can be seen in Fig. 7.4. There we see that the scheme produces a narrow transmission window (imaginary part is near zero) around a region where the index of refraction dips below zero. Although the index does not reach -1 in the transmission window, it is exciting that we can get a negative index at all. So called near-zero index materials such as this have gotten a lot of attention recently due to their interesting properties [114, 115] and applications [116].

For our spectral hole burning and EIT experiments, we were able to make use of just a small part of Eu:YSO's inhomogeneous linewidth, effectively reducing the linewidth of our system. Such a narrowing comes with a trade off though because only a small fraction of the europium ions were in the distilled peak we used for our experiments. Would such a trade off be worth it in our chirality scheme?

A potential answer to this question lies in Fig. 7.5. The two plots in the figure use only a fraction of the inhomogeneous linewidth, as well as a corresponding fraction of the ion density in the crystal. For example, if we are only using a 5 MHz inhomogeneous linewidth, we would run the simulation with only one fifth of of the ions. Although this simulates an inhomogeneous line with a square profile, it should still give us an idea of what effects ion-class distillation will have on the chirality scheme.

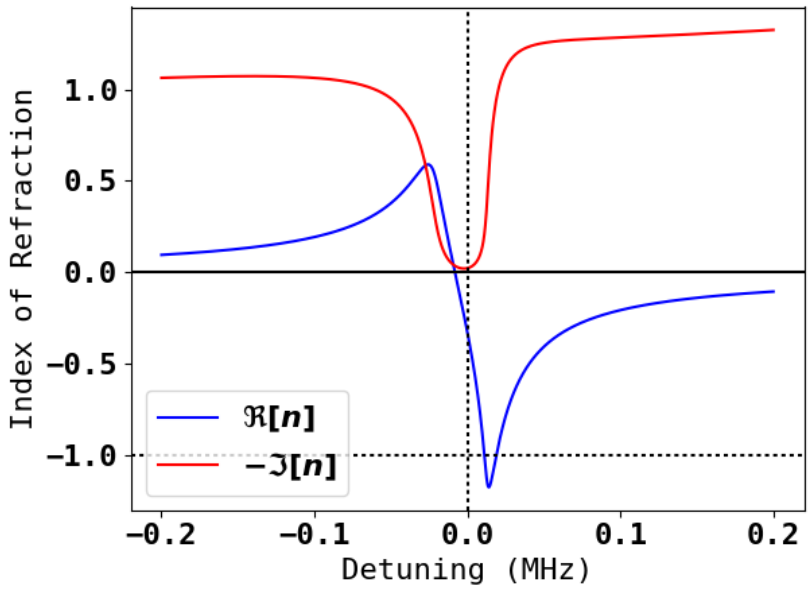

Figure 7.4: Index of refraction frequency sweep in Tb^{+3} in a stoichiometric crystal. The parameters used to make this plot were taken from Cowan's code and from typical values for stoichiometric crystals. See text for details.

The parameters used for the two plots were the same However, the left plot shows the real and imaginary part of the index of refraction when the real part is at a minimum and the right plot shows the real and imaginary parts when absorption is at a minimum. We see that we can, in fact, achieve an index of negative on. However, this comes at the cost of high absorption. On the other hand, if we focus on where absorption is low, we can still achieve a negative index suitable for near-zero index material applications. Based on these plots, it seems that the increased density has a greater benefit than decreased linewidth. We can compare these plots with the plot in Fig. 7.6 where we have not made any density adjustments. There we see, as we would expect, that if only the inhomogeneous linewidth is decreased, then a more negative index of refraction is achievable.

Although these results show that it might be possible to produce a negative index of refraction with low absorption using terbium ions, there are some important points to

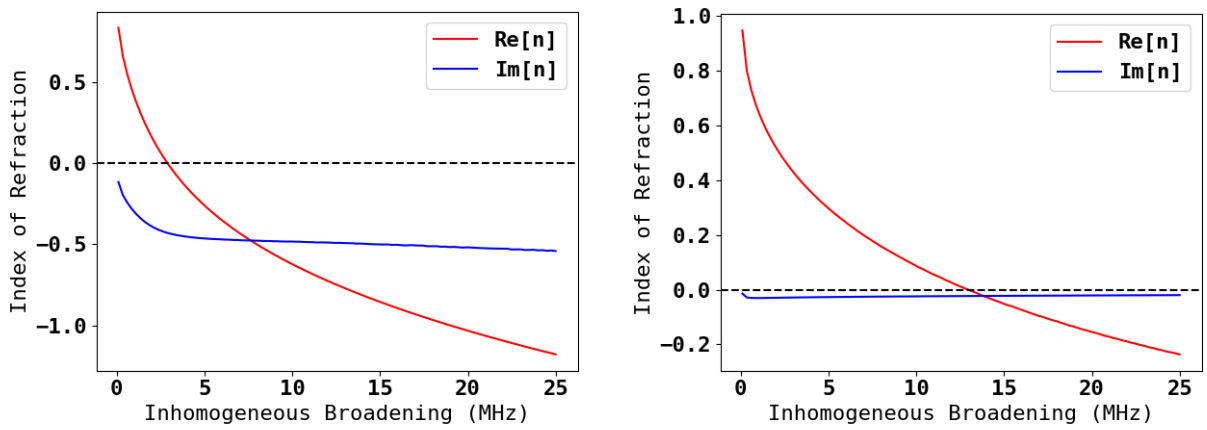

Figure 7.5: The index of refraction versus inhomogeneous broadening with the density adjusted to account for the narrower linewidth. On the left is the real and imaginary part of the index of refraction at the point where the real part is most negative. On the right, we have the real and imaginary parts for when absorption is at a minimum.

keep in mind. One is that we did not include crystal field mixing effects in the magnetic dipole moment. This will likely reduce the magnetic dipole moment, just like it did with europium. The effects of the crystal are also likely to broaden the optical transition's homogeneous linewidth. However, with a judicious choice of crystal, these effects could be minimized. Going forward, we will need to further study stoichiometric crystals in order to select a suitable crystal and to better understand the effects of the crystal on the spectroscopic properties on terbium. It would also be interesting to include higher order effects in the calculations done in [36]. Since the wavelength becomes elongated when the $|n| < 1$, it is easier to achieve proper phase matching for these effects, which could have an impact on the final result. Implementing these techniques will also require improvements to our laser system in order to produce a narrower laser linewidth in order to eliminate excess sources of noise and dephasing.

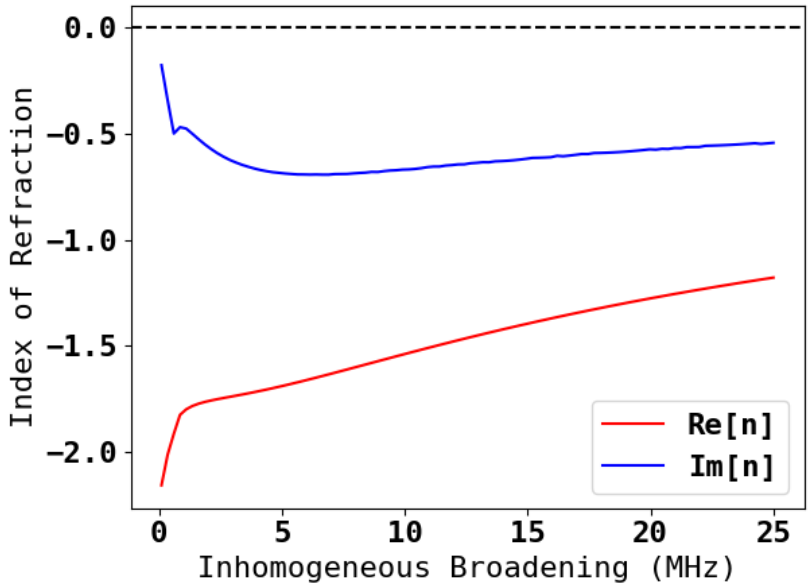

Figure 7.6: The minimum index of refraction versus the inhomogeneous broadening with no adjustments made to the density (all points in the plot were run with an ion density of 4×10^{27} m^{-3}.)

7.4 Conclusion

Through the work presented in this thesis, we have made significant strides towards producing an atomic metamaterial. One of the main challenges in producing such a metamaterial is finding an atomic system that has a strong magnetic response at optical frequencies. We have identified such a transition and measured its magnetic dipole moment via Rabi oscillations. In addition, we have acquired a better understanding of the mixing mechanisms that a host crystal imparts on its dopants. This understanding will be important going forward as we explore using other dopants and host crystals. We have also demonstrated manipulation of the magnetic susceptibility of our crystal in a linear way, via spectral hole burning, and in a nonlinear, coherent way via electromagnetically induced transparency. Such manipulations are important for chirality schemes that seek to enhance the magnetic response of a system through coherent coupling to

the electric response.

Over the past 20 years there has been an explosion in interest in negative index materials and materials with strong optical magnetic interactions. This explosion has been driven by metamaterials such as the split-ring resonator, and many of the exotic applications predicted by theory have been realized via these traditional metamaterials. The scale at which these metamaterials operate has also been pushed lower and lower over the past couple of decades, allowing for operation at shorter and shorter wavelengths. However, there are limitations to the shortest scale at which a traditional metamaterial can operate. These limitations are both technological, such as our ability to manufacture such small structures, and fundamental, as the frequency of operation begins to butt up against the plasma frequency of the underlying material that the structure is made out of. Our atomic metamaterial approaches offer the potential to overcome these limitations by exploiting the naturally small length scales present in crystal structures.

Despite the challenges we face going forward, atomic metamaterials are an exciting extension to the broader metamaterial community. In addition to extending established metamaterial applications to shorter wavelengths and smaller length scales, atomic metamaterials also offer an almost completely unexplored field in atomic and optical physics: interactions and interference between electric and magnetic optical transitions. Our group has already started exploring using this sort of interference to investigate things such as electromagnetic duality [117] and axion detection [118]. Even Heinrich Hertz couldn't see all the applications of the radio waves he discovered. I'm excited to see where the future takes this project.

Bibliography

[1] G. S. Ofelt, "Structure of the f6 configuration with application to rare-earth ions," *The Journal of Chemical Physics*, vol. 38, no. 9, pp. 2171–2180, 1963.

[2] V. G. Veselago, "The electrodynamics of substances with simultaneously negative values of ϵ and μ," *Soviet Physics Uspekhi*, vol. 10, no. 4, p. 509, 1968.

[3] J. B. Pendry, "Negative Refraction Makes a Perfect Lens," *Physical Review Letters*, vol. 85, no. 18, p. 3966, 2000.

[4] U. Leonhardt and T. G. Philbin, "General relativity in electrical engineering," *New Journal of Physics*, vol. 8, p. 247, 2006.

[5] U. Leonhardt, "Optical Conformal Mapping," *Science*, vol. 312, pp. 1777–1781, 2006.

[6] Y. Sun, T. Böttger, C. W. Thiel, and R. L. Cone, "Magnetic g tensors for the i 15/2 4 and i 13/2 4 states of Er3+: Y2 Si O5," *Physical Review B - Condensed Matter and Materials Physics*, vol. 77, no. 8, pp. 1–10, 2008.

[7] M. Mccall, J. B. Pendry, V. Galdi, Y. Lai, S. A. R. Horsley, J. Li, J. Zhu, R. C. Mitchell-Thomas, O. Quevedo-Teruel, P. Tassin, V. Ginis, E. Martini, G. Minatti, S. Maci, M. Ebrahimpouri, Y. Hao, P. Kinsler, J. Gratus, J. M. Lukens, A. W. Weiner, U. Leonhardt, I. I. Smolyaninov, V. N. Smolyaninova, R. T. Thompson, M. Wegener, M. Kadic, and S. A. Cummer, "Roadmap on transformation optics," *Journal of Optics*, vol. 20, p. 063001, 2018.

[8] J. B. Pendry, D. R. Smith, and S. Schultz, "Controlling Electromagnetic Fields," *Science*, vol. 312, no. June, pp. 1780–1783, 2006.

[9] M. Mccall, A. Favaro, P. Kinsler, and A. Boardman, "A spacetime cloak, or a history editor," *Journal of Optics*, vol. 13, p. 024003, 2011.

[10] M. Fridman, A. Farsi, Y. Okawachi, and A. L. Gaeta, "Demonstration of temporal cloaking," *Nature*, vol. 481, p. 62, 2012.

[11] J. M. Lukens, D. E. Leaird, and A. M. Weiner, "A temporal cloak at telecommunication data rate," *Nature*, vol. 498, no. 7453, pp. 205–208, 2013.

[12] S. Guenneau, C. Amra, and D. Veynante, "Transformation thermodynamics : cloaking and concentrating heat flux Abstract :," *Optics Express*, vol. 20, no. 7, pp. 8207–8218, 2012.

[13] G. Ma and P. Sheng, "Acoustic metamaterials : From local resonances to broad horizons," *Science Advances*, vol. 2, p. e1501595, 2016.

[14] S. Brûlé, S. Enoch, and S. Guenneau, "Emergence of seismic metamaterials : Current state and future perspectives," *Physics Letters A*, vol. 384, no. 1, p. 126034, 2020.

[15] S. A. Ramakrishna, J. B. Pendry, D. Schurig, D. R. Smith, and S. Schultz, "The asymmetric lossy near-perfect lens," *Journal of Modern Optics*, vol. 49, no. 10, pp. 1747–1762, 2002.

[16] S. A. Ramakrishna, "Physics of negative refractive index materials," *Reports on Progress in Physics*, vol. 68, pp. 449–521, 2005.

[17] G. Gomez-Santos, "Universal Features of the Time Evolution of Evanescent Modes in a Left-Handed Perfect Lens," *Physical Review Letters*, vol. 90, no. 7, p. 077401, 2003.

[18] G. W. 't Hooft, "Comment on "Negative Refraction Makes a Perfect Lens"," *Physical Review Letters*, vol. 87, no. 24, p. 249701, 2001.

[19] J. M. Williams, "Some Problems with Negative Refraction," *Physical Review Letters*, vol. 87, no. 24, p. 249703, 2001.

[20] N. Garcia and M. Nieto-Vesperinas, "Left-Handed Materials Do Not Make a Perfect Lens," *Physical Review Letters*, vol. 88, no. 20, p. 207403, 2002.

[21] J. Pendry, "Pendry Replies:," *Physical Review Letters*, vol. 87, no. 24, p. 249702, 2001.

[22] J. Pendry, "Pendry Replies:," *Physical Review Letters*, vol. 249703, p. 249704, 2001.

[23] J. B. Pendry, "Comment on "Left-Handed Materials Do Not Make a Perfect Lens"," *Physical Review Letters*, vol. 17, no. August, p. 99701, 2003.

[24] P. Markos and C. M. Soukoulis, *Wave Propagation: From Electrons to Photonic Crystals and Left-Handed Materials*. Princeton University Press, 2008.

[25] R. Ruppin, "Surface polaritons of a left-handed medium," *Physical Review A*, vol. 277, pp. 61–64, 2000.

[26] R. Ruppin, "Surface polaritons of a left-handed material slab," *Journal of Physics: Condensed Matter*, vol. 13, pp. 1811–1819, 2001.

[27] S. A. Maier, *PLASMONICS : FUNDAMENTALS AND APPLICATIONS*. Springer Science+Business Media LLC, 2007.

[28] J. B. Pendry, A. J. Holden, D. J. Robbins, and W. J. Stewart, "Magnetism from Conductors and Enhanced Nonlinear Phenomena," *IEEE Transactions on Microwave Theory and Techniques*, vol. 47, no. 11, pp. 2075–2084, 1999.

[29] M. Choi, J.-h. Choe, B. Kang, and C.-g. Choi, "A flexible metamaterial with negative refractive index at visible wavelength," *Current Applied Physics*, vol. 13, no. 8, pp. 1723–1727, 2013.

[30] S. Xiao, U. K. Chettiar, A. V. Kildishev, V. P. Drachev, and V. M. Shalaev, "Yellow-light negative-index metamaterials," *Optics Letters*, vol. 34, no. 22, pp. 3478–3480, 2009.

[31] R. S. Penciu, M. Kafesaki, T. Koschny, E. N. Economou, and C. M. Soukoulis, "Magnetic response of nanoscale left-handed metamaterials," *Physical Review B*, vol. 81, p. 235111, 2010.

[32] Y. Liang, Y. Zhiyong, R. Ningjuan, Q. Sun, and T. Xu, "Freestanding optical negative-index metamaterials of green light," *Optics Letters*, vol. 42, no. 16, p. 3239, 2017.

[33] L. Y. M. Tobing, L. Tjahjana, D. H. Zhang, and Q. Zhang, "Sub-100-nm Sized Silver Split Ring Resonator Metamaterials with Fundamental Magnetic Resonance in the Middle Visible Spectrum," *Advanced Optical Materials*, vol. 2, pp. 280–285, 2014.

[34] D. D. Yavuz and N. R. Brewer, "Left-handed electromagnetic waves in materials with induced polarization and magnetization," *Physical Review A*, vol. 90, no. October, p. 063807, 2014.

[35] D. E. Sikes and D. D. Yavuz, "Negative refraction with low absorption using Raman transitions with magnetoelectric coupling," *Physical Review A*, vol. 82, p. 011806, 2010.

[36] D. E. Sikes and D. D. Yavuz, "Negative refraction using Raman transitions and chirality," *Physical Review A*, vol. 84, p. 053836, 2011.

[37] D. E. Sikes, *THEORETICAL SCHEMES FOR NEGATIVE REFRACTION AND ENHANCED REFRACTIVE INDEX IN ATOMIC SYSTEMS*. Phd, University of Wisconsin - Madison, 2012.

[38] J. Kastel, M. Fleischhauer, S. F. Yelin, and R. L. Walsworth, "Tunable Negative Refraction without Absorption via Electromagnetically Induced Chirality," *Physical Review Letters*, vol. 99, p. 073602, 2007.

[39] J. Kastel, M. Fleischhauer, S. F. Yelin, and R. L. Walsworth, "Low-loss negative refraction by laser-induced magnetoelectric cross coupling," *Physical Review A*, vol. 79, p. 063818, 2009.

[40] D. D. Yavuz, "Refractive Index Enhancement in a Far-Off Resonant Atomic System," *Physical Review Letters*, vol. 95, no. November, p. 223601, 2005.

[41] N. A. Proite, B. E. Unks, J. T. Green, and D. D. Yavuz, "Refractive Index Enhancement with Vanishing Absorption in an Atomic Vapor," *Physical Review Letters*, vol. 101, no. OCTOBER, p. 147401, 2008.

[42] R. Cowan, *The Theory of Atomic Structure and Spectra*. University of California Press, Berkeley, 1981.

[43] B. R. Judd, *Operator Techniques in Atomic Spectroscopy*. McGraw-Hill, 1963.

[44] B. G. Wybourne and L. Smentek, *Optical Spectroscopy of Lanthanides: Magnetic and Hyperfine Interactions*. Taylor & Francis, 2007.

[45] Z. J. Simmons, *PROGRESS TOWARD A NEGATIVE REFRACTIVE INDEX IN AN ATOMIC SYSTEM: SPECTROSCOPY AND SIMULATIONS OF A RARE-EARTH DOPED CRYSTAL*. Phd, University of Wisconsin - Madison, 2015.

[46] G. Racah, "Theory of complex spectra. II," *Physical Review*, vol. 62, no. 9-10, pp. 438–462, 1942.

[47] G. Racah, "It III J.," *Physical Review*, vol. 61, p. 186, 1942.

[48] G. Racah, "Theory of complex spectra. III," *Physical Review*, vol. 63, no. 9-10, pp. 367–382, 1943.

[49] G. Racah, "Theory of complex spectra. IV," *Physical Review*, vol. 76, no. 9, pp. 1352–1365, 1949.

[50] S. HÜFNER, *Trivalent Ions in the Static Crystal Field*, vol. 1. Academic Press, 1 ed., 1978.

[51] M. C. Cunha, H. F. Brito, L. B. Zinner, G. Vicentini, and A. B. Nascimento, "Europium complexes with organic ligands containing oxygen as donor atom. Calculation of crystal-field and scalar strength parameters for C3v, D3 and D3d symmetries," *Coordination Chemistry Reviews*, vol. 119, no. C, pp. 1–28, 1992.

[52] B. R. Judd, "Optical absorption intensities of rare-earth ions," *Physical Review*, vol. 127, no. 3, pp. 750–761, 1962.

[53] G. S. Ofelt, "Intensities of Crystal Spectra of Rare-Earth Ions," *The Journal of Chemical Physics*, vol. 37, no. 3, pp. 511–520, 1962.

[54] M. P. Hehlen, M. G. Brik, and K. W. Kamerr, "50th anniversary of the Judd – Ofelt theory : An experimentalist ' s view of the formalism and its application," *Journal of Luminescence*, vol. 136, pp. 221–239, 2013.

[55] B. M. Walsh, "Judd-Ofelt Theory: Principles and Practices," in *Advances in Spectrocscopy for Lasers and Sensing*, pp. 403–433, Springer, 2006.

[56] G. H. Dieke and H. M. Crosswhite, "The Spectra of the Doubly and Triply Ionized Rare Earths," *Applied Optics*, vol. 2, no. 7, pp. 675–686, 1963.

[57] A. Freeman and R. Watson, "Theoretical Investigation of Some Magnetic and Spectroscopic Properties of Rare-Earth Ions," *Physical Review*, vol. 127, no. 6, pp. 2058–2075, 1962.

[58] M. Kasperczyk, S. Person, D. Ananias, L. D. Carlos, and L. Novotny, "Excitation of magnetic dipole transitions at optical frequencies," *Physical Review Letters*, vol. 114, p. 163903, 2015.

[59] F. Könz, Y. Sun, W. Thiel, L. Cone, W. Equall, L. Hutcheson, and M. Macfarlane, "Temperature and concentration dependence of optical dephasing, spectral-hole lifetime, and anisotropic absorption in Eu3+:Y2SiO5," *Physical Review B - Condensed Matter and Materials Physics*, vol. 68, no. 8, pp. 1–9, 2003.

[60] C. Li, C. Wyon, and R. Moncorgé, "Spectroscopic properties and fluorescence dynamics of Er3+ and Yb3+ in Y2SiO5," *IEEE*, vol. 28, no. 4, p. 1209, 1992.

[61] X. A. Shen and R. Kachru, "$^7F_0$-$^5D_1$ Transition in Eu^{3+}:Y_2SiO_5," *Journal of the Optical Society of America B*, vol. 11, no. 4, p. 591, 1994.

[62] R. Yano, M. Mitsunaga, and N. Uesugi, "Nonlinear laser spectroscopy of Eu^{3+}:Y_2SiO_5 and its application to time-domain optical memory," *Journal of the Optical Society of America B*, vol. 9, no. 6, p. 992, 1992.

[63] J. J. Longdell, A. L. Alexander, and M. J. Sellars, "Characterization of the hyperfine interaction in europium-doped yttrium orthosilicate and europium chloride hexahydrate," *Physical Review B - Condensed Matter and Materials Physics*, vol. 74, no. 19, pp. 1–7, 2006.

[64] B. Lauritzen, N. Timoney, N. Gisin, M. Afzelius, H. De Riedmatten, Y. Sun, R. M. MacFarlane, and R. L. Cone, "Spectroscopic investigations of Eu3+:Y2SiO 5 for quantum memory applications," *Physical Review B - Condensed Matter and Materials Physics*, vol. 85, no. 11, pp. 29–31, 2012.

[65] R. Beach, M. D. Shinn, L. Davis, R. W. Solarz, and W. F. Krupke, "Optical Absorption and Stimulated Emission of Neodymium in Yttrium Orthosilicate," *IEEE Journal of Quantum Electronics*, vol. 26, no. 8, pp. 1405–1412, 1990.

[66] R. M. Macfarlane and R. M. Shelby, "Spectroscopy of Solids Containing Rare Earth Ions," in *Spectroscopy of Solids Containing Rare Earth Ions* (A. A. Kaplianskii and R. M. MacFarlane, eds.), ch. 3, North Holland, Amsterdam, 1987.

[67] I. Mills and R. Jones, *Quantities, Units and Symbols in Physical Chemistry*, vol. 1. Blackwell Science Ltd, 1990.

[68] B. A. Maximov, Y. A. Charitonov, V. V. Ilyikhim, and N. B. Belov, "No," *Sov. Phys. Dokl.*, vol. 13, p. 1188, 1969.

[69] N. R. Brewer, *PROGRESS TOWARDS LEFT-HANDED ELECTROMAGNETIC WAVES IN RARE-EARTH DOPED CRYSTALS*. Phd, University of Wisconsin - Madison, 2017.

[70] N. R. Brewer, Z. N. Buckholtz, Z. J. Simmons, E. A. Mueller, and D. D. Yavuz, "Coherent magnetic response at optical frequencies using atomic transitions," *Physical Review X*, vol. 7, p. 011005, 2017.

[71] B. G. Wybourne, "Effective Operators and Spectroscopic Properties," *The Journal of Chemical Physics*, vol. 48, no. 6, p. 2596, 1968.

[72] M. Tanaka, G. Nishimura, T. Kushida, and T. J-mixing, "Contribution of J mixing to the $^5D_0$-$^7F_0$ transition of Eu^{3+} ions in several host matrices," *Physical Review B*, vol. 49, no. 24, p. 16917, 1994.

[73] R. W. Equall, Y. Sun, R. L. Cone, and R. M. Macfarlane, "Ultraslow optical dephasing in Eu^{3+}:Y_2SiO_5," *Physical Review Letters*, vol. 72, no. 14, pp. 2179–2182, 1994.

[74] A. L. Alexander, J. J. Longdell, and M. J. Sellars, "Measurement of the ground-state hyperfine coherence time of $^{151}Eu^{3+}$:Y_2SiO_5," *Journal of the Optical Society of America B*, vol. 24, no. 9, pp. 2479–2482, 2007.

[75] C. J. Hawthorn, K. P. Weber, and R. E. Scholten, "Littrow configuration tunable external cavity diode laser with fixed direction output beam," *Review of Scientific Instruments*, vol. 72, no. 12, pp. 4477–4479, 2001.

[76] R. W. P. Drever, J. L. Hall, F. V. Kowalski, J. Hough, G. M. Ford, A. J. Munley, and H. Ward, "Laser Phase and Frequency Stabilization Using an Optical Resonator," *Applied Physics B*, vol. 31, pp. 97–105, 1983.

[77] T. W. Hansch and B. Couillaud, "Laser frequency stabilization by polarization spectroscopy of a reflecting reference cavity," *Optics Communications*, vol. 35, no. 3, pp. 441–444, 1980.

[78] M. Nilsson, L. Rippe, N. Ohlsson, T. Christiansson, and S. Kröll, "Initial experiments concerning quantum information processing in rare-earth-ion doped crystals," *Physica Scripta T*, vol. 102, pp. 178–185, 2002.

[79] M. Nilsson, L. Rippe, S. Kröll, R. Klieber, and D. Suter, "Hole-burning techniques for isolation and study of individual hyperfine transitions in inhomogeneously broadened solids demonstrated in Pr 3+:Y2SiO5," *Physical Review B - Condensed Matter and Materials Physics*, vol. 70, no. 21, pp. 1–11, 2004.

[80] M. Zhong, M. P. Hedges, R. L. Ahlefeldt, J. G. Bartholomew, S. E. Beavan, S. M. Wittig, J. J. Longdell, and M. J. Sellars, "Optically addressable nuclear spins in a solid with a six-hour coherence time," *Nature*, vol. 517, no. 7533, pp. 177–180, 2015.

[81] K. J. Boller, A. Imamoglu, and S. E. Harris, "Observation of Electromagnetically Induced Transparency," *Physical Review Letters*, vol. 66, no. 20, pp. 2593–2596, 1991.

[82] J. E. Field, K. H. Hahn, and S. E. Harris, "Observation of Electromagnetically Induced Transparency in Collisionally Broadened Lead Vapor," *Physical Review Letters*, vol. 67, no. 22, p. 3062, 1991.

[83] S. E. Harris, "Lasers without Inversion: Interference of Lifetime-Broadened Resonances," *Physical Review Letters*, vol. 62, no. 9, pp. 1033–1036, 1989.

[84] S. E. Harris, J. E. Field, and A. Imamoglu, "Nonlinear Optical Processes Using Electromagnetically Induced Transparency," *Physical Review Letters*, vol. 64, no. 10, pp. 1107–1110, 1990.

[85] O. A. Kocharovskaya and Y. I. Khanin, "Population trapping and coherent bleaching of a three-level medium by a periodic train of ultrashort pulses 0.," *Sov. Phys. JETP*, vol. 63, no. May, pp. 945–950, 1986.

[86] P. Lambropoulos and P. Zoller, "Autoionizing states in strong laser fields," *Physical Review A*, vol. 24, no. 1, p. 379, 1981.

[87] H. Bachau, P. Lambropoulos, and R. Shakeshaft, "Theory oflaser-induced transitions between autoionizing states ofHe," *Physical Review A*, vol. 34, no. 6, p. 4785, 1986.

[88] S. P. Tewari and G. S. Agarwal, "Control of Phase Matching and Nonlinear Generation in Dense Media by Resonant Fields," *Physical Review Letters*, vol. 56, no. 17, p. 1811, 1986.

[89] B. S. Ham, P. R. Hemmer, and M. S. Shahriar, "Efficient electromagnetically induced transparency in a rare-earth doped crystal," *Optics Communications*, vol. 144, no. 4-6, pp. 227–230, 1997.

[90] B. S. Ham, M. S. Shahriar, M. K. Kim, and P. R. Hemmer, "Frequency-selective time-domain optical data storage by electromagnetically induced transparency in a rare-earth-doped solid," *Optics Letters*, vol. 22, no. 24, p. 1849, 1997.

[91] H. Q. Fan, K. H. Kagalwala, S. V. Polyakov, A. L. Migdall, and E. A. Goldschmidt, "Electromagnetically induced transparency in inhomogeneously broadened solid media," *Physical Review A*, vol. 99, p. 053821, 2019.

[92] L. V. Hau, S. E. Harris, Z. Dutton, C. H. Behroozi, and E. H. L. Boulevard, "Light speed reduction to 17 metres per second in an ultracold atomic gas," *Letters to Nature*, vol. 397, no. February, pp. 594–598, 1999.

[93] C. Liu, Z. Dutton, and C. H. Behroozi, "Observation of coherent optical information storage in an atomic medium using halted light pulses," *Letters to Nature*, vol. 409, no. January, 2001.

[94] A. V. Turukhin, V. S. Sudarshanam, and M. S. Shahriar, "Observation of Ultraslow and Stored Light Pulses in a Solid," *Physical Review Letters*, vol. 88, p. 023602, 2002.

[95] J. J. Longdell, E. Fraval, M. J. Sellars, and N. B. Manson, "Stopped light with storage times greater than one second using electromagnetically induced transparency in a solid," *Physical Review Letters*, vol. 95, no. 6, pp. 2–5, 2005.

[96] A. Andre and M. D. Lukin, "Manipulating Light Pulses via Dynamically Controlled Photonic Band gap," *Physical Review Letters*, vol. 89, no. 14, p. 143602, 2002.

[97] M. Bajcsy, A. S. Zibrov, and M. D. Lukin, "Stationary pulses of light in an atomic medium," *Letters to Nature*, vol. 426, p. 638, 2003.

[98] A. Andre, M. Bajcsy, A. S. Zibrov, and M. D. Lukin, "Nonlinear Optics with Stationary Pulses of Light," *Physical Review Letters*, vol. 94, p. 063902, 2005.

[99] J. Otterbach, R. G. Unanyan, and M. Fleischhauer, "Confining Stationary Light : Dirac Dynamics and Klein Tunneling," *Physical Review Letters*, vol. 102, p. 063602, 2009.

[100] Y.-h. Chen, M.-j. Lee, W. Hung, Y.-c. Chen, Y.-f. Chen, and I. A. Yu, "Demonstration of the Interaction between Two Stopped Light Pulses," *Physical Review Letters*, vol. 108, p. 173603, 2012.

[101] M.-j. Lee, K.-f. Chang, J. Ruseckas, C.-y. Lee, I. A. Yu, H.-w. Cho, and G. Juzeliu, "Experimental demonstration of spinor slow light," *Nature Communications*, vol. 5, p. 5542, 2014.

[102] C. L. G. Alzar, M. A. G. Martinez, P. Nussenzveig, and C. L. G. Alzar, "Classical analog of electromagnetically induced transparency Classical analog of electromagnetically induced transparency," *American Journal of Physics*, vol. 70, no. 37, p. 2002, 2014.

[103] M. Fleischhauer, A. Imamoglu, and J. P. Marangos, "Electromagnetically Induced Transparency : Optics in Coherent Media," *Reviews of Modern Physics*, vol. 77, p. 633, 2005.

[104] R. W. Boyd, *Nonlinear Optics*. Elsevier Inc., 2008.

[105] R. L. Ahlefeldt, M. R. Hush, and M. J. Sellars, "Ultranarrow Optical Inhomogeneous Linewidth in a Stoichiometric Rare-Earth Crystal," *Physical Review Letters*, vol. 117, p. 250504, 2016.

[106] J. J. Longdell, M. J. Sellars, and N. B. Manson, "Hyperfine interaction in ground and excited states of praseodymium-doped yttrium orthosilicate," *Physical Review B - Condensed Matter and Materials Physics*, vol. 66, no. 3, pp. 1–6, 2002.

[107] R. Macfarlane and R. Meltzer, "Optical measurement of the isotope shifts and hyperfine and superhyperfine interactions of Nd in the solid state," *Physical Review B - Condensed Matter and Materials Physics*, vol. 58, no. 9, pp. 5692–5700, 1998.

[108] R. M. Macfarlane, "High-resolution laser spectroscopy of rare-earth doped insulators: A personal perspective," *Journal of Luminescence*, vol. 100, no. 1-4, pp. 1–20, 2002.

[109] C. W. Thiel, T. Bottger, and R. L. Cone, "Rare-earth-doped materials for applications in quantum information storage and signal processing," *Journal of Luminescence*, vol. 131, no. 3, pp. 353–361, 2011.

[110] R. L. Ahlefeldt, M. J. Pearce, M. R. Hush, and M. J. Sellars, "Quantum processing with ensembles of rare-earth ions in a stoichiometric crystal," *Physical Review A*, vol. 101, no. 1, pp. 1–11, 2020.

[111] M. Lovrić, P. Glasenapp, and D. Suter, "Spin Hamiltonian characterization and refinement for Pr3 +:YAlO 3 and Pr3 +:Y 2SiO 5," *Physical Review B - Condensed Matter and Materials Physics*, vol. 85, no. 1, pp. 1–8, 2012.

[112] K. Holliday, M. Croci, E. Vauthey, and U. P. Wild, "Spectral hole burning and holography in an Y_2SiO_5:Pr^{3+} crystal," *Physical Review B*, vol. 47, no. 22, pp. 14741–14752, 1993.

[113] A. Arcangeli, M. LovriÄ, B. Tumino, A. Ferrier, and P. Goldner, "Spectroscopy and coherence lifetime extension of hyperfine transitions in 151Eu3+:Y2SiO5," *Physical Review B - Condensed Matter and Materials Physics*, vol. 89, no. 18, pp. 1–6, 2014.

[114] R. W. Ziolkowski, "Propagation in and scattering from a matched metamaterial having a zero index of refraction," *Physical Review E - Statistical Physics, Plasmas, Fluids, and Related Interdisciplinary Topics*, vol. 70, no. 4, p. 12, 2004.

[115] H. Suchowski, K. O'Brien, Z. J. Wong, A. Salandrino, X. Yin, and X. Zhang, "Phase Mismatch – Free Nonlinear Propagation in Optical Zero-Index Materials," *Science*, vol. 342, no. December, pp. 1223–1226, 2013.

[116] I. Liberal and N. Engheta, "Near-zero refractive index photonics," *Nature Photonics*, vol. 11, no. 3, pp. 149–158, 2017.

[117] D. D. Yavuz, "Magneto-electric interference and precision tests of EM duality," *to be submitted*, 2020.

[118] D. D. Yavuz, S. Inbar, and B. Lemberger, "Axion detection using laser four-wave mixing," 2020.

[119] R. Yano, M. Mitsunaga, and N. Uesugi, "Ultralong optical dephasing time in Eu^{3+}:Y_2SiO_5," *Optics Letters*, vol. 16, no. 23, p. 1884, 1991.

[120] F. Beil, J. Klein, G. Nikoghosyan, and T. Halfmann, "Electromagnetically induced transparency and retrieval of light pulses in a Λ-type and a V-type level scheme in Pr3+:Y 2SiO5," *Journal of Physics B: Atomic, Molecular and Optical Physics*, vol. 41, no. 7, 2008.

[121] A. E. Seigman, *Lasers*. University Science Books, 1986.

[122] A. Araya, S. Telada, K. Tochikubo, and S. Taniguchi, "Absolute-length determination of a long-baseline Fabry – Perot cavity by means of resonating modulation sidebands," *Applied Optics*, vol. 38, no. 13, p. 2848, 1999.

[123] P. J. Manson, "High precision free spectral range measurement using a phase modulated laser beam," *Review of Scientific Instruments*, vol. 70, p. 3834, 1999.

[124] K. M. Baird, "The Role of Interferometry in Long Distance Measurement," *Metrologia*, vol. 4, p. 135, 1968.

[125] A. N. Golubev, "ABSOLUTE LASER INTERFEROMETRIC DISTANCE MEASUREMENT," *Survey Review*, vol. 32, p. 248, 2013.

[126] D. Hils, J. L. Hall, D. Hils, and J. L. Hall, "Response of a Fabry – Perot cavity to phase modulated light," *Review of Scientific Instruments*, vol. 58, p. 1406, 1987.

[127] M. Aketagawa, S. Kimura, T. Yashiki, and H. Iwata, "Measurement of a free spectral range of a Fabry – Perot cavity using frequency modulation and null method under off-resonance conditions," *Measurement Science and Technology*, vol. 22, p. 025302, 2011.

[128] Scientific Materials Corp., "Y2SiO5 data sheet," 2010.

Appendix A

Spectral Hole Burning Details

Spectral hole burning can be tricky due to the large number of spectral features from both isotopes and the fact that we are using three beams, each of which will produce its own set of spectral features. In this appendix are sets of tables and diagrams which I found useful in sorting out why we were seeing peaks when we didn't expect to.

The class and transition labels in the tables are assigned as follows. The states are labeled with state one being the lowest ground state and state six being the highest excited state. The class label is determined by the two states connected by the beam doing the spectral hole burning. As discussed in the main text, there are nine such classes for each beam. The transition label refers to a particular transition within an ion class and is also labeled by the two states connected by whatever beam is used to observe the spectral holes.

The beam labels are the same labels used in Chapter 6. The tables in Secs. A.1 and A.2 assume that the burning beam, which could be the probe, coupling, or repump beams, is swept over a frequency range and produces spectral holes and antiholes with the same width that the burning beam was swept over. Then, the frequency ranges of these features are compared to the frequency ranges that the other two beams are being swept over in order to see where they overlap.

A.1 Troughs from Expected Upper State Splitting Order

A.1.1 Probe

Closest Beam	Class	Transition	Frequency Range
C	2→6	3→5	-78.5 to -66.5
R	2→6	3→4	-149.5 to -137.5
C	1→5	3→5	-92.8 to 80.8
R	1→5	3→4	-163.8 to -151.8

Table A.1: The antitroughs produced by the regions of the probe sweep that are not addressed by the repump.

If we compare the ranges in Tab. A.1 with the detuning of the beams we see that there is indeed some overlap.

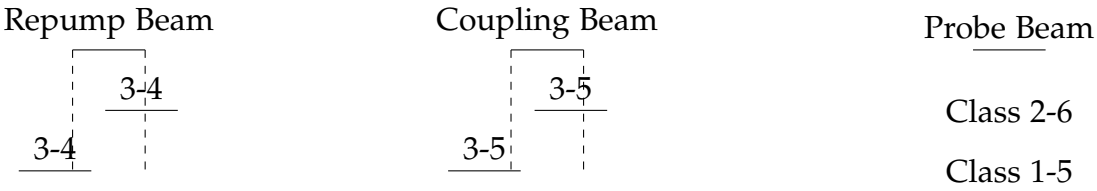

Figure A.1: Diagram showing the relation between the position (in frequency space) of the sweeping beams and the antitroughs created to sweeping $\pm$ 6 MHz around the probe frequency. The diagram is to scale with distance corresponding to frequency with left is negative, or decreasing frequency and right is positive, or increasing frequency. The first row shows the beam frequency with a sweep width of 12 MHz. The other rows are organized as follows. The right column specifies the ion class. Only ion classes with multiple antitroughs near the frequencies of the coupling and repump beams are considered. The rest of the columns in each row display the frequency range of the antitroughs. The transition that corresponds to that antitrough is indicated above each line. These are all from the 151 isotope.

A.1.2 Coupling

Closest Beam	Class	Transition	Frequency Range
R1	1→4	2→4	-63.3 to -51.3
R2	1→4	3→4	-92.8 to -80.8
R1	1→5	2→5	-63.3 to -51.3
R2	1→5	3→5	-92.8 to -80.8
R1	1→6	2→6	-63.3 to -51.3
R2	1→6	3→6	-92.8 to -80.8
R1	2→6	3→5	-78.5 to -66.5
R2	2→6	1→4	-62.7 to -50.7
R	3→6	2→4	-90.5 to -78.5
P	3→6	1→6	80.8 to 92.8
P1	3→5	2→6	66.5 to 78.5
P2	3→5	1→5	80.6 to 92.8

Table A.2: The antitroughs produced by the regions of the probe sweep that are not addressed by the repump.

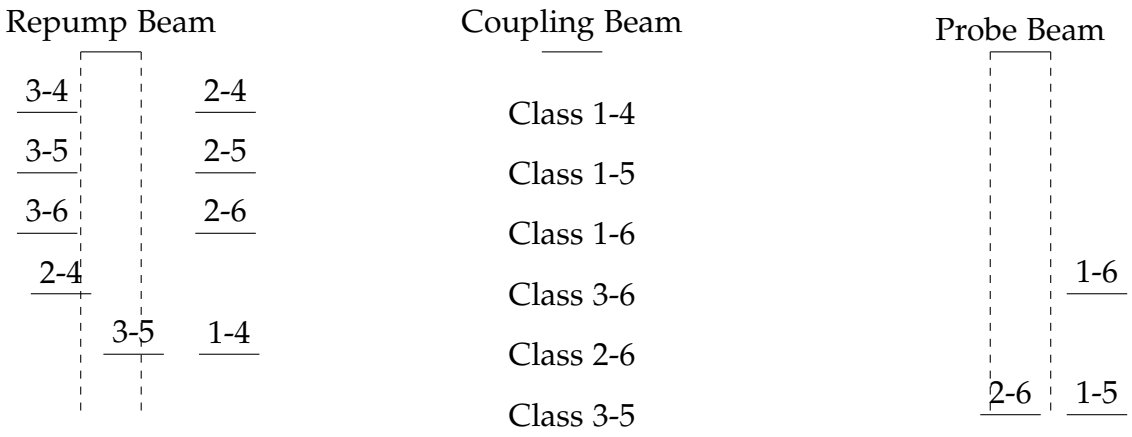

Figure A.2: Diagram showing the relation between the position (in frequency space) of the sweeping beams and the antitroughs created to sweeping $\pm$ 4 MHz around the coupling frequency. This diagram is organized the same way as Fig. A.1 except the antitroughs are 8 MHz wide due to the coupling beam only sweeping $\pm$ 4 MHz around the coupling frequency. The reason for this smaller sweep can be understood by examining the bottom class in the diagram, class 3-5. If the two antitroughs were 12 MHz wide then they would both overlap with the sweeping probe beam (also 8 MHz). This would prevent proper ion-class distillation. These are all from the 151 isotope.

A.1.3 Repump

Closest Beam	Class	Transition	Frequency Range
P1	3→4	2→6	137.5 to 149.5
P2	3→4	1→5	151.8 to 163.8
C	3→4	1→4	80.8 to 92.8
C1	3→5	1→5	80.8 to 92.8
C2	3→5	2→6	66.5 to 78.5
C1	2→4	3→6	78.5 to 90.5
C2	2→4	1→4	51.3 to 63.5

Table A.3: The antitroughs produced by the regions of the probe sweep that are not addressed by the repump.

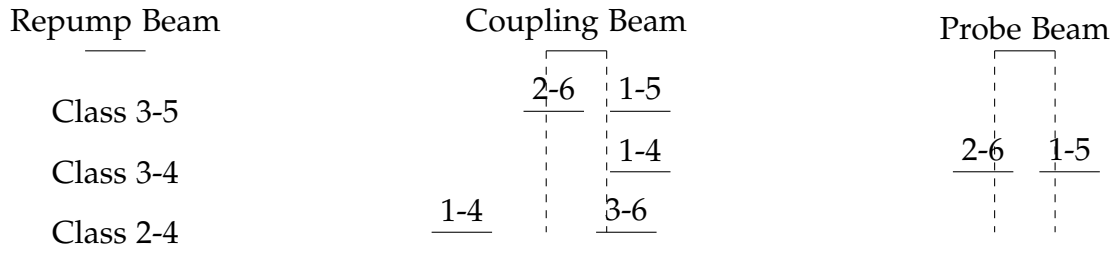

Figure A.3: Diagram showing the relation between the position (in frequency space) of the sweeping beams and the antitroughs created to sweeping ± 3 MHz around the repump frequency. This diagram is organized the same way as Fig. A.1 except the antitroughs are 8 MHz wide due to the repump beam only sweeping ± 3 MHz around the coupling frequency. The reason for this smaller sweep can be understood by examining the middle class in the diagram, class 3-4. If the two antitroughs were 12 MHz wide then they would both overlap with the sweeping probe beam (also 6 MHz). This would prevent proper ion-class distillation. These are all from the 151 isotope.

A.2 Troughs from Inverted Upper State Splitting Order

Because the ordering of the upper state splittings is not known, I have recreated the tables and figures from Sec. A.1 with the two excited splittings flipped.

A.2.1 Probe

Closest Beam	Class	Transition	Frequency Range
C	1→6	3→6	-92.8 to 80.8
R	1→6	3→5	-163.8 to -151.8

Table A.4: The antitroughs produced by the regions of the probe sweep that are not addressed by the repump.

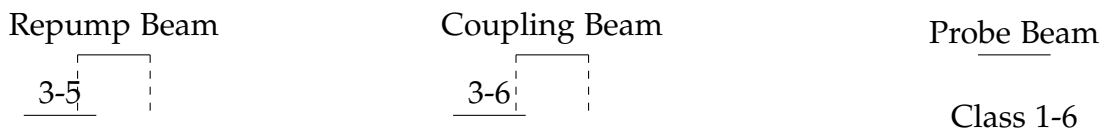

Figure A.4: Diagram showing the relation between the position (in frequency space) of the sweeping beams and the antitroughs created to sweeping $\pm$ 6 MHz around the probe frequency. The diagram is to scale with distance corresponding to frequency with left is negative, or decreasing frequency and right is positive, or increasing frequency. The first row shows the beam frequency with a sweep width of 12 MHz. The other rows are organized as follows. The right column specifies the ion class. Only ion classes with multiple antitroughs near the frequencies of the coupling and repump beams are considered. The rest of the columns in each row display the frequency range of the antitroughs. The transition that corresponds to that antitrough is indicated above each line. These are all from the 151 isotope.

A.2.2 Coupling

Closest Beam	Class	Transition	Frequency Range
R	3→6	2→4	-90.5 to -78.5
P	3→6	1→6	80.8 to 92.8

Table A.5: The antitroughs produced by the regions of the probe sweep that are not addressed by the repump.

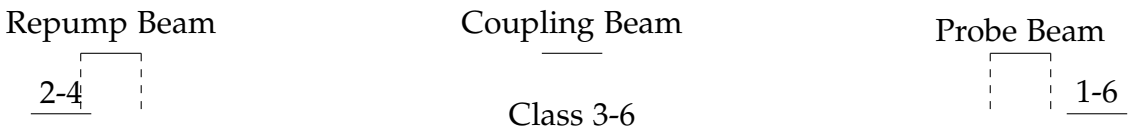

Figure A.5: Diagram showing the relation between the position (in frequency space) of the sweeping beams and the antitroughs created to sweeping $\pm$ 4 MHz around the coupling frequency. This diagram is organized the same way as Fig. A.1 except the antitroughs are 8 MHz wide due to the coupling beam only sweeping $\pm$ 4 MHz around the coupling frequency. The reason for this smaller sweep can be understood by examining the bottom class in the diagram, class 3-5. If the two antitroughs were 12 MHz wide then they would both overlap with the sweeping probe beam (also 8 MHz). This would prevent proper ion-class distillation. These are all from the 151 isotope.

A.2.3 Repump

Closest Beam	Class	Transition	Frequency Range
P	3→4	2→6	137.5 to 149.5
C1	3→4	2→5	66.5 to 78.5
C2	3→4	1→4	80.8 to 92.8
P	3→5	1→6	151.8 to 163.8
C	3→5	1→5	80.8 to 92.8

Table A.6: The antitroughs produced by the regions of the probe sweep that are not addressed by the repump.

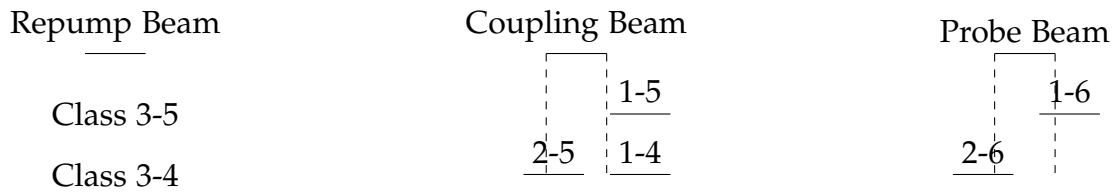

Figure A.6: Diagram showing the relation between the position (in frequency space) of the sweeping beams and the antitroughs created to sweeping ± 3 MHz around the repump frequency. This diagram is organized the same way as Fig. A.1 except the antitroughs are 8 MHz wide due to the repump beam only sweeping ± 3 MHz around the coupling frequency. The reason for this smaller sweep can be understood by examining the middle class in the diagram, class 3-4. If the two antitroughs were 12 MHz wide then they would both overlap with the sweeping probe beam (also 6 MHz). This would prevent proper ion-class distillation. These are all from the 151 isotope.

A.3 All SHB Features

Hole Frequencies

Eu 151

Frequency (MHz)	Transition	Class
-114.0	1→4	1→6
-114.0	3→4	3→6
-114.0	2→4	2→6
-71.0	3→4	3→5
-71.0	2→4	2→5
-71.0	1→4	1→5
-43.0	1→5	1→6
-43.0	3→5	3→6
-43.0	2→5	2→6
0	1→6	1→6
0	3→5	3→5
0	3→4	3→4
0	2→5	2→5
0	3→6	3→6
0	1→4	1→4
0	2→4	2→4
0	1→5	1→5
0	2→6	2→6
43.0	3→6	3→5
43.0	2→6	2→5
43.0	1→6	1→5
71.0	3→5	3→4
71.0	1→5	1→4
71.0	2→5	2→4
114.0	3→6	3→4
114.0	1→6	1→4
114.0	2→6	2→4

Eu 153

Frequency (MHz)	Transition	Class
-297.0	1→4	1→6
-297.0	2→4	2→6
-297.0	3→4	3→6
-183.0	1→4	1→5
-183.0	2→4	2→5
-183.0	3→4	3→5
-114.0	1→5	1→6
-114.0	2→5	2→6
-114.0	3→5	3→6
0	1→4	1→4
0	1→5	1→5
0	1→6	1→6
0	2→4	2→4
0	2→5	2→5
0	2→6	2→6
0	3→4	3→4
0	3→5	3→5
0	3→6	3→6
114.0	1→6	1→5
114.0	2→6	2→5
114.0	3→6	3→5
183.0	1→5	1→4
183.0	2→5	2→4
183.0	3→5	3→4
297.0	1→6	1→4
297.0	2→6	2→4
297.0	3→6	3→4

Negative Antihole Frequencies

Eu 151		
Frequency (MHz)	Transition	Class
-200.8	3→4	1→6
-171.3	2→4	1→6
-157.8	3→4	1→5
-143.5	3→4	2→6
-129.8	3→5	1→6
-128.3	2→4	1→5
-100.5	3→4	2→5
-100.3	2→5	1→6
-86.8	3→4	1→4
-86.8	3→5	1→5
-86.8	3→6	1→6
-84.5	2→4	3→6
-72.5	3→5	2→6
-57.3	2→4	1→4
-57.3	2→5	1→5
-57.3	2→6	1→6
-56.7	1→4	2→6
-43.8	3→6	1→5
-41.5	2→4	3→5
-29.5	3→4	2→4
-29.5	3→5	2→5
-29.5	3→6	2→6
-27.2	1→4	3→6
-15.8	3→5	1→4
-14.3	2→6	1→5
-13.7	1→4	2→5
-13.5	2→5	3→6

Eu 153		
Frequency (MHz)	Transition	Class
-521.5	3→4	1→6
-445.1	2→4	1→6
-407.5	3→4	1→5
-373.4	3→4	2→6
-338.5	3→5	1→6
-331.1	2→4	1→5
-262.1	2→5	1→6
-259.4	3→4	2→5
-224.5	3→4	1→4
-224.5	3→5	1→5
-224.5	3→6	1→6
-220.6	2→4	3→6
-190.4	3→5	2→6
-148.9	1→4	2→6
-148.1	2→4	1→4
-148.1	2→5	1→5
-148.1	2→6	1→6
-110.5	3→6	1→5
-106.6	2→4	3→5
-76.4	3→4	2→4
-76.4	3→5	2→5
-76.4	3→6	2→6
-72.5	1→4	3→6
-41.5	3→5	1→4
-37.6	2→5	3→6
-34.9	1→4	2→5
-34.1	2→6	1→5

Positive Antihole Frequencies

Eu 151

Frequency (MHz)	Transition	Class
13.5	3→6	2→5
13.7	2→5	1→4
14.3	1→5	2→6
15.8	1→4	3→5
27.2	3→6	1→4
29.5	2→4	3→4
29.5	2→5	3→5
29.5	2→6	3→6
41.5	3→5	2→4
43.8	1→5	3→6
56.7	2→6	1→4
57.3	1→4	2→4
57.3	1→5	2→5
57.3	1→6	2→6
72.5	2→6	3→5
84.5	3→6	2→4
86.8	1→4	3→4
86.8	1→5	3→5
86.8	1→6	3→6
100.3	1→6	2→5
100.5	2→5	3→4
128.3	1→5	2→4
129.8	1→6	3→5
143.5	2→6	3→4
157.8	1→5	3→4
171.3	1→6	2→4
200.8	1→6	3→4

Eu 153

Frequency (MHz)	Transition	Class
34.1	1→5	2→6
34.9	2→5	1→4
37.6	3→6	2→5
41.5	1→4	3→5
72.5	3→6	1→4
76.4	2→4	3→4
76.4	2→5	3→5
76.4	2→6	3→6
106.6	3→5	2→4
110.5	1→5	3→6
148.1	1→4	2→4
148.1	1→5	2→5
148.1	1→6	2→6
148.9	2→6	1→4
190.4	2→6	3→5
220.6	3→6	2→4
224.5	1→4	3→4
224.5	1→5	3→5
224.5	1→6	3→6
259.4	2→5	3→4
262.1	1→6	2→5
331.1	1→5	2→4
338.5	1→6	3→5
373.4	2→6	3→4
407.5	1→5	3→4
445.1	1→6	2→4
521.5	1→6	3→4

Appendix B

EuYSO Info

Here is a collection of data for Eu:YSO from various sources that would likely be useful to have in one spot for future students working on this project.

B.1 Eu:YSO Transitions

Transition	Site 1 ν (cm^{-1})	Site 1 λ (nm)	Site 2 ν (cm^{-1})	Site 2 λ (nm)
$\|^7F_0\rangle \rightarrow \|^7F_1\rangle$	203	49261.084	224	44642.857
$\|^7F_0\rangle \rightarrow \|^7F_1\rangle$	418	23923.445	409	24449.878
$\|^7F_0\rangle \rightarrow \|^7F_1\rangle$	506	19762.846	493	20283.976
$\|^7F_0\rangle \rightarrow \|^5D_0\rangle$	17240	580.046	17235	580.215
$\|^7F_0\rangle \rightarrow \|^5D_1\rangle$	18951	527.677	18955	527.565
$\|^7F_0\rangle \rightarrow \|^5D_1\rangle$	18994	526.482	18997	526.399
$\|^7F_0\rangle \rightarrow \|^5D_1\rangle$	19021	525.735	19016	525.873
$\|^7F_0\rangle \rightarrow \|^5D_2\rangle$	21384	467.639	21409	467.093
$\|^7F_0\rangle \rightarrow \|^5D_2\rangle$	21395	467.399	21424	466.766
$\|^7F_0\rangle \rightarrow \|^5D_2\rangle$	21414	466.984	21445	466.309
$\|^7F_0\rangle \rightarrow \|^5D_2\rangle$	21519	464.706	21494	465.246
$\|^7F_0\rangle \rightarrow \|^5D_2\rangle$	21537	464.317	21519	464.706

Table B.1: Transitions from the ground state according to [62].

Transition	Site 1 ν (cm^{-1})	Site 1 λ (nm)	Site 2 ν (cm^{-1})	Site 2 λ (nm)
$\|^5D_1\rangle \rightarrow \|^7F_0\rangle$	18951	527.677	18955	527.565
$\|^5D_1\rangle \rightarrow \|^7F_1\rangle$	18748	533.39	18731	533.874
$\|^5D_1\rangle \rightarrow \|^7F_1\rangle$	18533	539.578	18546	539.2
$\|^5D_1\rangle \rightarrow \|^7F_1\rangle$	18445	542.152	18462	541.653
$\|^5D_1\rangle \rightarrow \|^5D_0\rangle$	1711	5844.535	1720	5813.953
$\|^5D_1\rangle \rightarrow \|^5D_1\rangle$	43	232558.14	42	238095.238
$\|^5D_1\rangle \rightarrow \|^5D_1\rangle$	70	142857.143	61	163934.426
$\|^5D_1\rangle \rightarrow \|^5D_2\rangle$	2433	4110.152	2454	4074.98
$\|^5D_1\rangle \rightarrow \|^5D_2\rangle$	2444	4091.653	2469	4050.223
$\|^5D_1\rangle \rightarrow \|^5D_2\rangle$	2463	4060.089	2490	4016.064
$\|^5D_1\rangle \rightarrow \|^5D_2\rangle$	2568	3894.081	2539	3938.558
$\|^5D_1\rangle \rightarrow \|^5D_2\rangle$	2586	3866.976	2564	3900.156

Table B.2: Transitions from $|^5D_1\rangle$ according to [62].

B.2 Free Ion Energies

From Cowan's code.

Level	ν (cm^{-1})
$^7F_0$	0
$^7F_1$	374
$^7F_2$	1036
$^7F_3$	1888
$^7F_4$	2866
$^7F_5$	3921
$^7F_6$	5022
$^5D_0$	17374
$^5D_1$	**18945**
$^5D_2$	21508
$^5D_3$	24456
$^5D_4$	27747
$^3P_1$	37040
$^5K_6$	37573
$^5K_7$	38809

B.3 Free Ion States [1]

B.3.1 The ^{7}F Manifold

$$
\begin{aligned}
{}^7F_0 =& 0.968|{}^7F_0\rangle + 0.0016|{}^5D_0\rangle + 0.1659|{}^5D_0'\rangle - 0.1815|{}^5D_0''\rangle \\
{}^7F_1 =& 0.9742|{}^7F_1\rangle - 0.0027|{}^5P_1\rangle + 0.0052|{}^5D_1\rangle + 0.1472|{}^5D_1'\rangle - 0.1645|{}^5D_1''\rangle + 0.0263|{}^5F_1\rangle \\
& + 0.0162|{}^5F_1'\rangle \\
{}^7F_2 =& 0.9819|{}^7F_2\rangle - 0.0025|{}^5G_2\rangle + 0.0005|{}^5S_2\rangle - 0.0147|{}^5G_2'\rangle - 0.0035|{}^5P_2\rangle + 0.0172|{}^5G_2''\rangle \\
& + 0.0108|{}^5D_2\rangle + 0.1161|{}^5D_2'\rangle - 0.1353|{}^5D_2''\rangle + 0.0452|{}^5F_2\rangle + 0.0289|{}^5F_2'\rangle \\
{}^7F_3 =& 0.9897|{}^7F_3\rangle - 0.0327|{}^5G_3\rangle - 0.0327|{}^5G_3'\rangle - 0.0036|{}^5P_3\rangle + 0.0309|{}^5G_3''\rangle + 0.0180|{}^5D_3\rangle \\
& + 0.0219|{}^5H_3\rangle + 0.0863|{}^5D_3'\rangle + 0.0020|{}^5H_3'\rangle - 0.0953|{}^5D_3''\rangle + 0.0659|{}^5F_3\rangle + 0.0499|{}^5F_3'\rangle \\
{}^7F_4 =& 0.9897|{}^7F_4\rangle + 0.0126|{}^5D_4\rangle + 0.0428|{}^5D_4'\rangle - 0.0594|{}^5D_4''\rangle + 0.0751|{}^5F_4\rangle + 0.0435|{}^5F_4'\rangle \\
& - 0.0028|{}^5G_4\rangle - 0.0057|{}^5G_4'\rangle + 0.0591|{}^5G_4''\rangle + 0.0039|{}^5H_4\rangle \\
& + 0.0055|{}^5H_4'\rangle - 0.0004|{}^5I_4\rangle - 0.0002|{}^5I_4'\rangle \\
{}^7F_5 =& 0.9880|{}^7F_5\rangle + 0.0723|{}^5F_5\rangle + 0.0392|{}^5F_5'\rangle - 0.0405|{}^5G_5\rangle - 0.0847|{}^5G_5'\rangle + 0.0886|{}^5G_5''\rangle \\
& + 0.0075|{}^5H_5\rangle + 0.0096|{}^5H_5'\rangle - 0.0010|{}^5I_5\rangle - 0.0005|{}^5I_5'\rangle + 0.0001|{}^5K_5\rangle \\
{}^7F_6 =& 0.9825|{}^7F_6\rangle - 0.0676|{}^5G_5\rangle - 0.1201|{}^5G_6'\rangle + 0.1228|{}^5G_6''\rangle + 0.0094|{}^5H_6\rangle + 0.0106|{}^5H_6'\rangle \\
& - 0.0014|{}^5I_6\rangle - 0.0006|{}^5I_6'\rangle - 0.0014|{}^5K_6\rangle - 0.0001|{}^5L_6\rangle
\end{aligned}
\tag{B.1}
$$

B.3.2 The ^{5}D Manifold

$$
\begin{aligned}
{}^5D_0 =& -0.2381|^7F_0\rangle - 0.1969|^5D_0\rangle + 0.6893|^5D_0'\rangle - 0.5390|^5D_0''\rangle \\
{}^5D_1 =& -0.2096|^7F_0\rangle + 0.0012|^5P_1\rangle - 0.2066|^5D_1\rangle + 0.7162|^5D_1'\rangle - 0.5561|^5D_1''\rangle - 0.0536|^5F_1\rangle \\
& - 0.0373|^5F_1'\rangle \\
{}^5D_2 =& -0.1624|^7F_2\rangle - 0.0155|^5G_2\rangle + 0.0037|^5S_2\rangle + 0.0014|^5G_2'\rangle - 0.0054|^5P_2\rangle + 0.0038|^5G_2''\rangle \\
& - 0.2104|^5D_2\rangle + 0.7456|^5D_2'\rangle - 0.5742|^5D_2''\rangle - 0.0888|^5F_2\rangle - 0.0724|^5F_2'\rangle \\
{}^5D_3 =& -0.1085|^7F_3\rangle - 0.0437|^5G_3\rangle - 0.0252|^5G_3'\rangle - 0.0094|^5P_3\rangle + 0.0196|^5G_3''\rangle - 0.2036|^5D_3\rangle \\
& + 0.0146|^5H_3\rangle + 0.7509|^5D_3'\rangle + 0.0017|^5H_3'\rangle - 0.5826|^5D_3''\rangle - 0.1330|^5F_3\rangle - 0.0881|^5F_3'\rangle \\
{}^5D_4 =& -0.0401|^7F_4\rangle + 0.0107|^5G_4\rangle + 0.0656|^5G_4'\rangle - 0.0682|^5G_4''\rangle - 0.1754|^5D_4\rangle - 0.0544|^5H_4\rangle \\
& + 0.7419|^5D_4'\rangle - 0.0542|^5H_4'\rangle - 0.5783|^5D_4''\rangle 0.0191|^5I_4\rangle - 0.1716|^5F_4\rangle + 0.0052|^5I_4'\rangle \\
& - 0.1016|^5F_4'\rangle
\end{aligned}
\tag{B.2}
$$

B.4 General Properties of Some Rare Earths (and Y and Si)

Isotope	Nuclear Magnetic Moment (μ_N)	Nuclear Quadrupole Moment (fm^2)	I	Abundance (%)
$^{151}_{63}$Eu	3.47	90.3	5/2	47.8
$^{153}_{63}$Eu	1.53	241.2	5/2	52.2
$^{141}_{59}$Pr	4.28	-5.89	5/2	100
$^{167}_{68}$Er	-0.56	356.5	7/2	22.3
$^{143}_{60}$Nd	-1.065	-63	7/2	12.2
$^{145}_{60}$Nd	-0.656	-33	7/2	8.3

Table B.3: Some properties of the isotopes of rare earths that are commonly used as crystal dopants [67]. Note that some of these elements have unstable isotopes or isotopes with zero nuclear quadrupole moment. These isotopes are not listed in the above table.

Isotope	Nuclear Magnetic Moment (μ_N)	Nuclear Quadrupole Moment (fm^2)	I	Abundance (%)
$^{89}_{39}$Y	-0.137	-	1/2	100
$^{29}_{14}$Si	-0.555	-	1/2	4.7

Table B.4: Some nuclear properties of the constituents of YSO [67]. Although oxygen has a stable isotope with a nonzero nuclear magnetic moment, its abundance is 0.038 %.

B.5 YSO

The chemical unit of YSO is Y_2SiO_5. Within each unit cell there are 4 chemical units resulting in 8 Y's. These 8 Y's occupy two inequivalent sites in each unit cell, 4 Y's in each.

The dopant ions replace Y. At 0.1% doping in YSO results in an average spacing of dopant ions of 4.75 nm (the ion density is 9.35x10^{2}4 m^{-3}).

B.6 $^{153}_{63}$Eu: Site 1

All information about site 1 is for the $^7F_0 \rightarrow ^5D_0$ transition, which is a forced electric dipole transition due to the crystal field.

Dipole Moment	Oscillator Strength	Wavelength
5x10$^-$33 C m[64]	1.3x10^{-8} [59]	579.88 nm [119]

Optical T_1	Optical T_2	Optical Inhomogeneous Linewidth
2 ms [119]	0.477 ms [73]	8.6 Ghz [73]

Hyperfine T_1	Hyperfine T_2	Hyperfine Inhomogeneous Linewidth
>20 days [59]	-	-

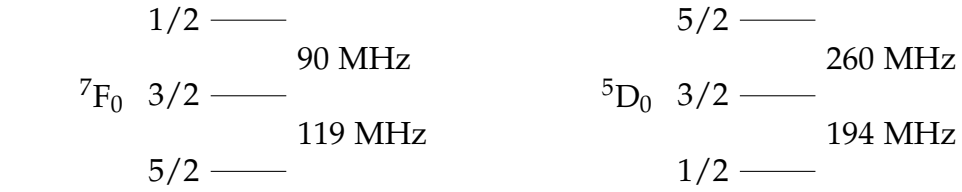

Figure B.1: ^{153}Eu site 1 hyperfine splittings for the $^7F_0$ and $^5D_0$ states.

The excited splittings can be found in [119, 64] and are known [64]. The ground state splittings can be found in [62, 64].

B.7 $^{153}_{63}$Eu: Site 2

B.7.1 $^7F_0 \rightarrow ^5D_1$ Transition

This transition is a magnetic dipole transition.

Dipole Moment	Oscillator Strength	Wavelength
0.063 μ_B [70]	6x10^{-8} [61]	527.5 nm [70, 61]

Optical T_1	Optical T_2	Optical Inhomogeneous Linewidth (4.5 K, 0.1% doping)
33 - 42 μs [70, 61]	56 μs [61]	1.6 Ghz [70]

Hyperfine T_1	Hyperfine T_2	Hyperfine Inhomogeneous Linewidth
>20 days [59]	-	-

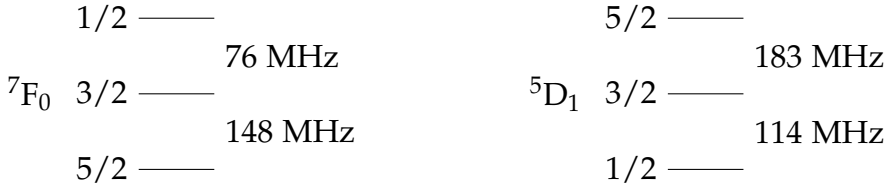

Figure B.2: ^{153}Eu site 2 hyperfine splittings for the $^7F_0$ and $^5D_1$ states.

The excited state splittings can be found in [61], and the ground state splittings can be found in [62]. The ordering of the upper transitions is not known. However, I have ordered them in analogy to the site 1 $^5D_0$ states.

B.7.2 $^7F_0 \rightarrow ^5D_0$ Transition

This transition is a forced electric dipole transition.

Dipole Moment	Oscillator Strength	Wavelength
5x10$^-$33 C m[64]	1.3-3x10^{-8} [59, 64]	580.05 nm [119, 73]

Optical T_1	Optical T_2	Optical Inhomogeneous Linewidth
1.7 ms [119]	0.822 - 2.6 ms [73]	5.6 Ghz [73]

Hyperfine T_1	Hyperfine T_2	Hyperfine Inhomogeneous Linewidth
>20 days [59]	-	-

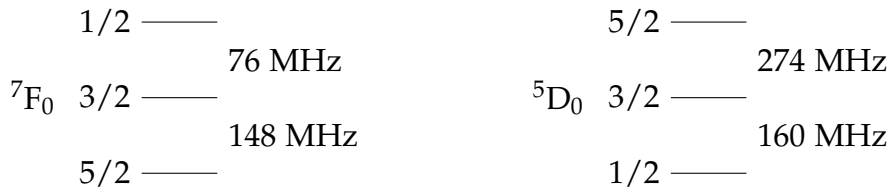

Figure B.3: ^{153}Eu site 2 hyperfine splittings for the $^7F_0$ and $^5D_0$ states.

The excited state splittings can be found in [119], and the ground state splittings can be found in [62]. The ordering of the upper transitions is not known. However, I have ordered them in analogy to the site 1 $^5D_0$ states.

B.8 $^{151}_{63}$Eu: Site 1

Dipole Moment	Oscillator Strength	Wavelength
-	-	580.05 nm -

Optical T_1	Optical T_2	Optical Inhomogeneous Linewidth
-	-	-

Transition	Hyperfine T_1	Hyperfine T_2	Hyperfine Inhomogeneous Linewidth
$1/2 \leftrightarrow 3/2$	>20 days [59]	-	21 kHz [113]
$3/2 \leftrightarrow 5/2$	>20 days [59]	-	38 kHz [113]

These are for the ground ($^7F_0$) hyperfine states. The T_1 times are actually for site 2, but I've assumed that they will be about the same for the site 1 transitions.

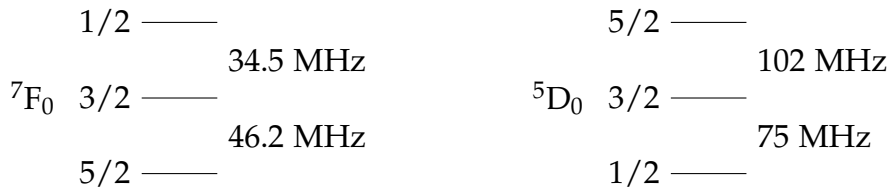

Figure B.4: ^{151}Eu site 1 hyperfine splittings for the $^7F_0$ and $^5D_0$ states.

The excited state splittings can be found in [113, 119, 63]. The ordering of the upper states seems to be quite debatable. The 1/2 to 3/2 transition is 75 MHz and the 3/2 to 5/2 trasition is 102 MHz in [119, 63]. The frequencies and transitions are flipped in [113]. I went with the ordering shown here mainly due to having a majority vote and agreement between [119] and [64] about one of the ^{153} sites. It is interesting to note that [63] reports the wrong wavelength for the transition. They report the Pr:YSO transition wavelength (605.7 nm).

The ground state splittings can be found in [113, 63, 62].

B.9 $^{151}_{63}$Eu: Site 2

B.9.1 $^7F_0 \rightarrow ^5D_0$ Transition

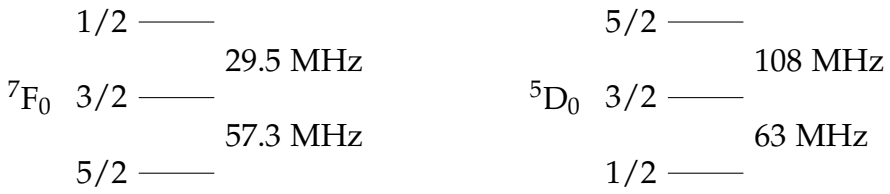

Figure B.5: ^{151}Eu site 2 hyperfine splittings for the $^7F_0$ and $^5D_0$ states.

The excited state splittings can be found in [119, 78], and the ground state splittings can be found in [78, 62]. The ordering of the upper transitions is not known.

All optical properties (optical decay times, dipole moment...) are the same as for 153. The change in isotope only affects the hyperfine properties.

B.9.2 $^7F_0 \rightarrow ^5D_1$ Transition

The only new information for this transition on this isotope that hasn't been mentioned in the 153 sections (optical properties) or the $^5D_0$ transition section (ground state splitting) is the hyperfine splittings of the $^5D_1$ state.

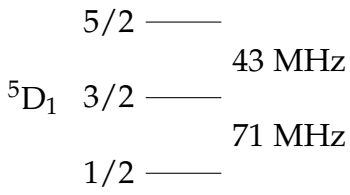

Figure B.6: ^{151}Eu site 2 hyperfine splittings for the $^5D_1$ state.

Again, the order of the upper states is not known. However, we have reason to believe that the ordering is that shown. This ordering has been infered by the excess population present after ion-class distillation. It seems more plossible that this ordering could produce that extra population.

B.10 $^{141}_{60}$Pr: Site 1

The transition typically used in Pr:YSO is the $^3H_4 \rightarrow ^1D_2$ transition. Although I refer to this site as site 1 , as does the literature, I'm not sure if it is the same site 1 as the Eu site 1.

Dipole Moment	Oscillator Strength	Wavelength
1.9x10$^-$32 C m[120]	10^{-7} [120]	605.7 - 605.98 nm [90, 89, 112]

Optical T_1	Optical T_2	Optical Inhomogeneous Linewidth
164 μs [89, 95]	111 μs [89, 95]	4 Ghz [89]

Transition	Hyperfine T_1	Hyperfine T_2	Hyperfine Inhomogeneous Linewidth
$1/2 \leftrightarrow 3/2$	100 s [112]	500 μs [95, 90]	30-50 kHz [112, 111]
$3/2 \leftrightarrow 5/2$	100 s [112]	500 μs [95, 90]	70-75 kHz [112, 111]

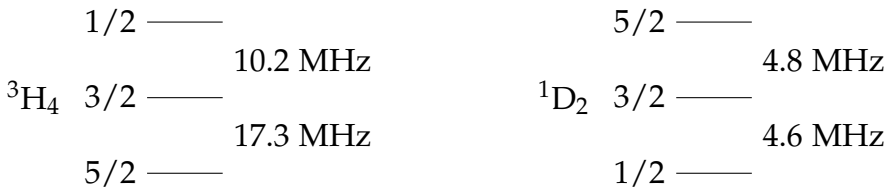

Figure B.7: ^{141}Pr site 1 hyperfine splittings for the $^3H_4$ and $^1D_2$ states.

These splittings can be found in [111, 120, 79, 90, 89] and [106]. There seems to be some disagreement on the ordering of the upper states. Although the 4.6 MHz transition is always between the 1/2 and 3/2 states and the 4.8 MHz transition is always between the 3/2 and 5/2 states, some papers have the order of the states reversed from what I've shown here. The references with the order reversed are [90, 89] and [106]. The references with the same order that I've shown are [111, 120] and [79]. I chose to show the ordering that I did because that is the ordering found in more recent papers.

Appendix C

EIT Derivations

C.1 Derivation of the EIT Susceptibility

C.1.1 With Phenomenologically added Decay

In order to transform to the rotating frame, we will transform our system with a unitary transformation Under the unitary transformation $|\Psi\rangle \rightarrow U|\Psi_0\rangle$, where $i\hbar\frac{\partial|\Psi_0\rangle}{\partial t} = H_0|\Psi\rangle$, the Hamiltonian H for $|\Psi\rangle$ can be expressed in terms of H_0 as

$$H = UH_0U^\dagger + i\hbar\frac{\partial U}{\partial t}U^\dagger \tag{C.1}$$

The derivation goes as such:

$$\begin{aligned} H|\Psi\rangle &= i\hbar\frac{\partial|\Psi\rangle}{\partial t} \\ &= i\hbar\left(\frac{\partial U}{\partial t}\right)|\Psi_0\rangle + i\hbar U\frac{\partial|\Psi_0\rangle}{\partial t} \\ &= \left(i\hbar\frac{\partial U}{\partial t} + UH_0\right)|\Psi_0\rangle \\ &= \left(i\hbar\frac{\partial U}{\partial t}U^\dagger + UH_0U^\dagger\right)|\Psi\rangle \end{aligned}$$

The unitary transformation that will be used can be written as the 3x3 matrix

$$U = \begin{pmatrix} e^{i\omega_a t} & 0 & 0 \\ 0 & e^{i\omega_b t} & 0 \\ 0 & 0 & e^{i\omega_d t} \end{pmatrix}$$

The terms in the transformed Hamiltonian that do not include the perturbations can be written

$$U^\dagger H_0 U + i\hbar U \frac{\partial U^\dagger}{\partial t} = \hbar \begin{pmatrix} \omega_1 - \omega_a & 0 & 0 \\ 0 & \omega_2 - \omega_b & 0 \\ 0 & 0 & \omega_3 - \omega_d - i\Gamma_3/2 \end{pmatrix}$$

where we have added in the decay term Γ_3.

In this system there are two perturbing beams incident on the atom. The probe beam connects $|1\rangle$ and $|3\rangle$ and the control beam connects $|2\rangle$ and $|3\rangle$. All dipole moments except for the ones between these states are zero. Thus, the perturbation can be written as

$$V = -\begin{pmatrix} 0 & 0 & E_p \cos(\omega_p t)\langle 1|r|3\rangle \\ 0 & 0 & E_c \cos(\omega_c t)\langle 2|r|3\rangle \\ E_p \cos(\omega_p t)\langle 3|r|1\rangle & E_c \cos(\omega_c t)\langle 3|r|2\rangle & 0 \end{pmatrix}$$

This perturbation can be written in terms of the Rabi frequency, $\Omega = E\mu/\hbar$ where μ is the dipole moment between the two states, and complex exponents as

$$V = -\hbar \begin{pmatrix} 0 & 0 & \frac{\Omega_p}{2}(e^{i\omega_p t} + e^{-i\omega_p t}) \\ 0 & 0 & \frac{\Omega_c}{2}(e^{i\omega_c t} + e^{-i\omega_c t}) \\ \frac{\Omega_p}{2}(e^{i\omega_p t} + e^{-i\omega_p t}) & \frac{\Omega_c}{2}(e^{i\omega_c t} + e^{-i\omega_c t}) & 0 \end{pmatrix} \tag{C.2}$$

The transformed perturbation part of the Hamiltonian is given by

$$U^\dagger V U = -\hbar \begin{pmatrix} 0 & 0 & \frac{\Omega_p}{2}(e^{i((\omega_d-\omega_a)+\omega_p)t}+e^{i((\omega_d-\omega_a)-\omega_p)t}) \\ 0 & 0 & \frac{\Omega_c}{2}(e^{i((\omega_d-\omega_b)+\omega_c)t}+e^{i((\omega_d-\omega_b)-\omega_c)t}) \\ \frac{\Omega_p}{2}(e^{i((\omega_a-\omega_d)+\omega_p)t}+e^{i((\omega_a-\omega_d)-\omega_p)t}) & \frac{\Omega_c}{2}(e^{i((\omega_b-\omega_d)+\omega_c)t}+e^{i((\omega_b-\omega_d)-\omega_c)t}) & 0 \end{pmatrix}$$

If we pick $\omega_a = \omega_1$, $\omega_b = \omega_1 + \omega_p - \omega_c$, and $\omega_d = \omega_1 + \omega_p$, along with using the rotating wave approximation (high frequency components average to zero), our transformed Hamiltonian parts becomes

$$U^\dagger H_0 U + i\hbar U \frac{\partial U^\dagger}{\partial t} = \hbar \begin{pmatrix} 0 & 0 & 0 \\ 0 & \delta\omega & 0 \\ 0 & 0 & \Delta\omega_p - i\Gamma_3/2 \end{pmatrix}$$

$$U^\dagger V U = \hbar \begin{pmatrix} 0 & 0 & -\frac{\Omega_p}{2} \\ 0 & 0 & -\frac{\Omega_c}{2} \\ -\frac{\Omega_p}{2} & -\frac{\Omega_c}{2} & 0 \end{pmatrix}$$

with $\delta\omega = \omega_2 - \omega_b$ and $\Delta\omega_p = \omega_3 - \omega_d$. Thus the full transformed Hamiltonian is

$$\boxed{H = \hbar \begin{pmatrix} 0 & 0 & -\frac{\Omega_p}{2} \\ 0 & \delta\omega & -\frac{\Omega_c}{2} \\ -\frac{\Omega_p}{2} & -\frac{\Omega_c}{2} & \Delta\omega_p - i\Gamma_3/2 \end{pmatrix}} \tag{C.3}$$

The ω's can be interpreted as follows:

- $\omega_a = \omega_1$: self explanatory.
- $\omega_b = \omega_1 + \omega_p - \omega_c$: represents a two photon process that starts in $|1\rangle$, is excited to a detuned $|3\rangle$, and then is de-excited to a detuned $|2\rangle$.

- $\omega_d = \omega_1 + \omega_p$: represent a single photon process that starts in $|1\rangle$ and ends in a detuned $|3\rangle$.
- $\delta\omega = \omega_2 - \omega_b$: the detuning of the two photon process from $|2\rangle$.
- $\Delta\omega_p = \omega_3 - \omega_d$: the detuning of the single photon process from $|3\rangle$.

These are not the only choices we could have made for the frequencies in the unitary matrix. For example, The unitary matrix we used to set up our Rabi flopping simulations was chosen so that all the diagonal elements were zero [69].

Because we are ultimately looking for the coherences between states, it will be convenient to work with the density matrix. Since the density matrix is defined as $|\Psi\rangle\langle\Psi|$, the matrix turns into

$$\rho = |\Psi\rangle\langle\Psi| = U^\dagger|\Psi_0\rangle\langle\Psi_0|U = U^\dagger\rho_0 U$$

$$\begin{pmatrix} \rho_{11} & \rho_{12} & \rho_{13} \\ \rho_{21} & \rho_{22} & \rho_{23} \\ \rho_{31} & \rho_{32} & \rho_{33} \end{pmatrix} = \begin{pmatrix} e^{-i\omega_a t} & 0 & 0 \\ 0 & e^{-i\omega_b t} & 0 \\ 0 & 0 & e^{-i\omega_d t} \end{pmatrix} \begin{pmatrix} \rho_{0,11} & \rho_{0,12} & \rho_{0,13} \\ \rho_{0,21} & \rho_{0,22} & \rho_{0,23} \\ \rho_{0,31} & \rho_{0,32} & \rho_{0,33} \end{pmatrix} \begin{pmatrix} e^{-i\omega_a t} & 0 & 0 \\ 0 & e^{-i\omega_b t} & 0 \\ 0 & 0 & e^{-i\omega_d t} \end{pmatrix}$$

$$= \begin{pmatrix} \rho_{0,11} & \rho_{0,12}e^{i(\omega_p-\omega_c)t} & \rho_{0,13}e^{i\omega_p t} \\ \rho_{0,21}e^{-i(\omega_p-\omega_c)t} & \rho_{0,22} & \rho_{0,23}e^{i\omega_c t} \\ \rho_{0,31}e^{-i\omega_p t} & \rho_{0,32}e^{-i\omega_c t} & \rho_{0,33} \end{pmatrix} \tag{C.4}$$

The density matrix and the Hamiltonian with phenomenological decay term are then put into the equation of motion

$$\dot{\rho} = -\frac{i}{\hbar}[H, \rho].$$

After carrying out the matrix multiplication, the time derivative of the density matrix is given by

$$\begin{aligned}
\dot{\rho_{11}} &= \frac{i\Omega_p}{2}(\rho_{31} - \rho_{13}) \\
\dot{\rho_{12}} &= \frac{i\Omega_p}{2}\rho_{32} - \frac{i\Omega_c}{2}\rho_{13} + i\delta\omega\rho_{12} \\
\dot{\rho_{13}} &= \frac{i\Omega_p}{2}(\rho_{33} - \rho_{11}) - \frac{i\Omega}{2}\rho_{12} - (\frac{\Gamma_3}{2} - i\Delta\omega_p)\rho_{13} \\
\dot{\rho_{21}} &= -\frac{i\Omega_p}{2}\rho_{32} + \frac{i\Omega_c}{2}\rho_{13} - i\delta\omega\rho_{12} \\
\dot{\rho_{22}} &= \frac{i\Omega_c}{2}(\rho_{32} - \rho_{23}) \\
\dot{\rho_{23}} &= \frac{i\Omega_c}{2}(\rho_{33} - \rho_{22}) - \frac{i\Omega_p}{2}\rho_{21} + (i\Delta\omega_p - i\delta\omega - \frac{\Gamma_3}{2})\rho_{23} \\
\dot{\rho_{31}} &= -\frac{i\Omega_p}{2}(\rho_{33} - \rho_{11}) + \frac{i\Omega}{2}\rho_{12} + (\frac{\Gamma_3}{2} - i\Delta\omega_p)\rho_{13} \\
\dot{\rho_{32}} &= -\frac{i\Omega_c}{2}(\rho_{33} - \rho_{22}) + \frac{i\Omega_p}{2}\rho_{21} - (i\Delta\omega_p - i\delta\omega - \frac{\Gamma_3}{2})\rho_{23} \\
\dot{\rho_{33}} &= \frac{i\Omega_p}{2}(\rho_{13} - \rho_{31}) + \frac{i\Omega_C}{2}(\rho_{23} - \rho_{32})
\end{aligned} \tag{C.5}$$

C.1.2 Susceptibility

We can find an expression for the susceptibility from the definition of the polarization, $P = \epsilon_0\chi\tilde{E} = N < \mu >$. Thus the expression for the susceptibility is

$$\boxed{\chi = \frac{N < \mu >}{\epsilon_0\tilde{E}}} \tag{C.6}$$

where N is the density of atoms, $\tilde{E}$ is the complex electric field, and $< \mu >$ is the expectation value of the dipole operator.

Expectation Value of the Dipole Operator

In the density matrix formulation, the expectation value of an operator, such as $< \mu >$, is given by

$$< \mu > = \mathrm{Tr}(\rho\mu) = \mathrm{Tr}\left[\begin{pmatrix} \rho_{11} & \rho_{12} & \rho_{13} \\ \rho_{21} & \rho_{22} & \rho_{23} \\ \rho_{31} & \rho_{32} & \rho_{33} \end{pmatrix} \begin{pmatrix} 0 & 0 & \mu_{13} \\ 0 & 0 & \mu_{23} \\ \mu_{31} & \mu_{32} & 0 \end{pmatrix} \right]$$
$$= \mu_{31}\rho_{13} + \mu_{32}\rho_{23} + \mu_{13}\rho_{31} + \mu_{23}\rho_{32}$$

Since all the time dependence of the expectation value for the dipole operator is in the density matrix elements (C.4), we can use the orthogonality of the complex exponentials and the relation $\tilde{E} \propto < \mu >$ to eliminate all but the ρ_{13} and ρ_{31} terms.

Finding the Density Matrix Elements

We will solve for the density matrix elements in the steady state (i.e. $\dot{\rho} = 0$) assuming that most of the population remains in $|1\rangle$, the ground state (i.e. $\rho_{11} = 1$, and $\rho_{22} = \rho_{33} = 0$, a.k.a weak probe beam, a.k.a. small rabi frequency). Since all we need are the density matrix elements ρ_{13} and ρ_{31} and since the density matrix is Hermitian, we will solve for the element ρ_{13} using elements (1, 2), (1, 3), and (3, 2) from C.5. Starting with element (1, 2) we get

$$0 = \frac{i\Omega_p}{2}\rho_{23} - \frac{i\Omega_c}{2}\rho_{13} + i\delta\omega\rho_{12}$$
$$\rho_{12} = \frac{1}{\delta\omega}\left(\frac{\Omega_c}{2}\rho_{13} - \frac{\Omega_p}{2}\rho_{32}\right)$$

From element (3, 2) we get

$$0 = \frac{i\Omega_p}{2}\rho_{12} + (i\delta\omega + \Gamma_3/2 - i\Delta\omega_p)\rho_{32}$$
$$\rho_{32} = \frac{i\Omega_p\rho_{12}}{2i\Delta\omega_p - 2i\delta\omega - \Gamma_3}$$

Putting the result for ρ_{32} into the equation for ρ_{12} gives

$$\rho_{12} = \frac{\Omega_c}{2\delta\omega}\rho_{13} - \frac{i\Omega_p^2\rho_{12}}{2\delta\omega(2i\Delta\omega_p - 2i\delta\omega - \Gamma_3)} = \frac{\Omega_c}{2\delta\omega}\rho_{13}$$

where the last equality results from the weak probe beam (Ω_p^2 term drops out). We can get another expression involving ρ_{12} and ρ_{13} from element (1, 3)

$$0 = -\frac{i\Omega_p}{2} - \frac{i\Omega_c}{2}\rho_{12} - (\frac{\Gamma_3}{2} - i\Delta\omega_p)\rho_{13}$$
$$\rho_{13} = \frac{-i}{\Gamma_3 - 2i\Delta\omega_p}(\Omega_p + \Omega_c\rho_{12})$$

Combining the last two results and rearranging gives us the final expression for ρ_{13}

$$\boxed{\rho_{13} = \frac{2\delta\omega\Omega_p}{4\delta\omega\Delta\omega_p - 2i\delta\omega\Gamma_3 - \Omega_c^2}} \tag{C.7}$$

Explicit Form of the Susceptibility

Referring back to the relation $P = \epsilon_0\chi\tilde{E} = N < \mu >$ and taking the electric field to be $Ee^{i\omega_p t}$, we can see that the corresponding part of the polarization that responds at this frequency is $N\mu_{31}\rho_{0,13}e^{i\omega_p t}$. From here on out we will drop the 0 subscript from the density matrix elements and find that the susceptibility corresponding to ρ_{13} is

$$\chi_{13} = \frac{N\mu_{13}}{\epsilon_0 E_p}\rho_{13}$$

The electric field amplitude can be replaced with the Rabi frequency to get

$$\chi_{13} = \frac{N\mu_{31}}{\epsilon_0}\frac{\mu_{13}}{\Omega_p\hbar}\rho_{13} = \frac{N|\mu_{13}|^2}{\epsilon_0\hbar\Omega_p}\rho_{13}$$

since $\mu_{31}\mu_{13} = \mu_{31}\mu_{31}^* = \mu_{13}^*\mu_{13} = |\mu_{13}|^2$. Substituting in Eq. C.7 gives the final form of the susceptibility

$$\chi_{13} = \frac{2N|\mu_{13}|^2}{\epsilon_0\hbar}\frac{\delta\omega}{4\Delta\omega_p\delta\omega - \Omega_c^2 - 2i\delta\omega\Gamma_3} \tag{C.8}$$

with real and imaginary parts

$$\Re[\chi_{13}] = \frac{2N|\mu_{13}|^2}{\epsilon_0\hbar}\frac{4\Delta\omega_p\delta\omega^2 - \delta\omega\Omega_c^2}{(4\Delta\omega_p\delta\omega - \Omega_c^2)^2 + 4\delta\omega^2\Gamma_3^2}$$
$$\Im[\chi_{13}] = \frac{2N|\mu_{13}|^2}{\epsilon_0\hbar}\frac{2\delta\omega^2\Gamma_3}{(4\Delta\omega_p\delta\omega - \Omega_c^2)^2 + 4\delta\omega^2\Gamma_3^2}$$

A particular case of interest is when $\delta\omega = \Delta\omega_p$. From their definitions ($\delta\omega = \omega_2 - \omega_1 - \omega_p + \omega_c$ and $\Delta\omega_p = \omega_3 - \omega_1 - \omega_p$) we see that $\omega_3 = \omega_2 + \omega_c$, i.e. the control beam is not detuned and is constant. Therefore, both variables depend only on ω_p and its detuning. The real and imaginary parts of the response are

$$\Re[\chi_{13}] = \frac{2N|\mu_{13}|^2}{\epsilon_0\hbar}\frac{4\Delta\omega_p^3 - \Delta\omega_p\Omega_c^2}{(4\Delta\omega_p^2 - \Omega_c^2)^2 + 4\Delta\omega_p^2\Gamma_3^2} \tag{C.9}$$
$$\Im[\chi_{13}] = \frac{2N|\mu_{13}|^2}{\epsilon_0\hbar}\frac{2\Delta\omega_p^2\Gamma_3}{(4\Delta\omega_p^2 - \Omega_c^2)^2 + 4\Delta\omega_p^2\Gamma_3^2} \tag{C.10}$$

C.1.3 With Lindblad Superoperators

The system discussed so far included a phenomenological decay by changing the upper state frequency from a real number to a complex number. This is unsatisfying for several reasons. One is that it does not allow for a closed system. The complex frequency adds

exponential decay to the time evolution. Another is that real systems can have decay from more than just the upper state. Also, there can be dephasing, which destroys coherence but does not cause population decay. Last, it would be nice to be able to derive the decay. A common derivation starts with the Jaynes-Cummings and the density matrix. The system is assumed to have no memory and the Born approximation is used with the quantum Louiville equation. Although we will not go through a derivation, some can be found in [**?**, **?**]. The result is known as the Lindblad form of the master equation.

The Lindblad form of the master equation can be written as

$$\dot{\rho} = -\frac{i}{\hbar}[\hat{H}, \rho] + \sum_i \Gamma_i D[c_i]\rho \tag{C.11}$$

where the sum is over all the decay channels. D is known as the Lindblad superoperator and can be expressed as

$$D[c]\rho = c\rho c^\dagger - \frac{1}{2}\{c^\dagger c, \rho\} \tag{C.12}$$

As an example, we can take one of the most general closed system forms of our three-level system. Population can decay from the upper state and end up in either of the ground states. There is also dephasing of states $|2\rangle$ and $|3\rangle$. Eq. C.11 can be explicitly rewritten for this particular case as

$$\dot{\rho} = -\frac{i}{\hbar}[\hat{H}, \rho] + \Gamma_{31} D[\sigma_{13}]\rho + \Gamma_{32} D[\sigma_{23}]\rho + \gamma_3 D[\sigma_3]\rho + \gamma_2 D[\sigma_2]\rho. \tag{C.13}$$

Γ_{31} and Γ_{32} are the population decay rates from state $|3\rangle$ to $|1\rangle$ and $|3\rangle$ to $|2\rangle$ respectively. γ_3 and γ_2 are the dephasing rates of states 3 and 2 respectively. The σ_{ij} matrices are transfer matrices fro the state j to the state i and the σ_k matrices give the population of

state k. They can be written as

$$\sigma_{13} = \begin{pmatrix} 0 & 0 & 1 \\ 0 & 0 & 0 \\ 0 & 0 & 0 \end{pmatrix}; \quad \sigma_{23} = \begin{pmatrix} 0 & 0 & 0 \\ 0 & 0 & 1 \\ 0 & 0 & 0 \end{pmatrix}; \quad \sigma_3 = \begin{pmatrix} 0 & 0 & 0 \\ 0 & 0 & 0 \\ 0 & 0 & 1 \end{pmatrix}; \quad \sigma_2 = \begin{pmatrix} 0 & 0 & 0 \\ 0 & 1 & 0 \\ 0 & 0 & 0 \end{pmatrix} \tag{C.14}$$

Each of the decoherence (dephasing and population decay) terms in Eq. C.13 can be written in matrix form as

$$\Gamma_{31} D[\sigma_{13}]\rho = \Gamma_{31} \begin{pmatrix} \rho_{33} & 0 & -\frac{1}{2}\rho_{13} \\ 0 & 0 & -\frac{1}{2}\rho_{23} \\ -\frac{1}{2}\rho_{31} & -\frac{1}{2}\rho_{32} & -\rho_{33} \end{pmatrix}; \quad \Gamma_{32} D[\sigma_{13}]\rho = \Gamma_{32} \begin{pmatrix} 0 & 0 & -\frac{1}{2}\rho_{13} \\ 0 & \rho_{33} & -\frac{1}{2}\rho_{23} \\ -\frac{1}{2}\rho_{31} & -\frac{1}{2}\rho_{32} & -\rho_{33} \end{pmatrix}$$

$$\gamma_3 D[\sigma_3]\rho = \gamma_3 \begin{pmatrix} 0 & 0 & -\frac{1}{2}\rho_{13} \\ 0 & 0 & -\frac{1}{2}\rho_{23} \\ -\frac{1}{2}\rho_{31} & -\frac{1}{2}\rho_{32} & 0 \end{pmatrix}; \quad \gamma_2 D[\sigma_2]\rho = \gamma_2 \begin{pmatrix} 0 & -\frac{1}{2}\rho_{12} & 0 \\ -\frac{1}{2}\rho_{21} & 0 & -\frac{1}{2}\rho_{23} \\ 0 & -\frac{1}{2}\rho_{32} & 0 \end{pmatrix}. \tag{C.15}$$

These matrices can be combined into a single decoherence matrix

$$\begin{pmatrix} \Gamma_{31}\rho_{33} & -\frac{\gamma_2}{2}\rho_{12} & -\frac{\Gamma_{31}+\Gamma_{32}+\gamma_3}{2}\rho_{13} \\ -\frac{\gamma}{2}\rho_{21} & \Gamma_{32}\rho_{33} & -\frac{\Gamma_{31}+\Gamma_{32}+\gamma_3+\gamma_2}{2}\rho_{23} \\ -\frac{\Gamma_{31}+\Gamma_{32}+\gamma_3}{2}\rho_{31} & -\frac{\Gamma_{31}+\Gamma_{32}+\gamma_3+\gamma_2}{2}\rho_{32} & -(\Gamma_{31}+\Gamma_{32})\rho_{33} \end{pmatrix} \tag{C.16}$$

If we make the same assumptions about EIT that we did before ($\rho_{11} = 1$, $\rho_{22} = \rho_{33} = 0$) and add Eq. C.16 to Eq. C.5 we see that this effectively replaces each of the frequency terms, ($\delta\omega$, $\Delta\omega_p$, etc.) with a complex number. We then derive an expression for ρ_{13} following the same procedure that we used with Eq. C.16 except with Eq. C.5 added. By doing this we get a new form of Eq. C.7 with $\delta\omega$ replaced with $\delta\omega - i\gamma_2/2$ and Γ_3 replaced with $\Gamma_{31} + \Gamma_{32} + \gamma_3$. Using the notation of [103] ($\gamma_{21} = \gamma_2$, $\gamma_{31} = \Gamma_{31} + \Gamma_{32} + \gamma_3$),

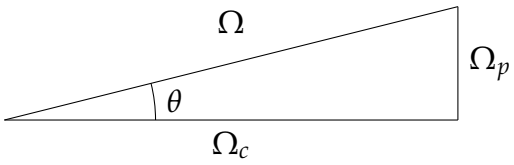

Figure C.1: The Rabi frequencies Ω_p, Ω_c, and $\Omega = \sqrt{\Omega_p^2 + \Omega_c^2}$ represented as a right triangle.

Eq. C.7 becomes

$$\rho_{13} = \frac{2\delta\omega\Omega_p - i\gamma_{21}\Omega_p}{4\delta\omega\Delta\omega_p - \gamma_{21}\gamma_{31} - \Omega_c^2 - 2i(\gamma_{21}\Delta\omega_p + \delta\omega\gamma_{31})}. \tag{C.17}$$

The susceptibility then becomes

$$\begin{aligned}
\Re[\chi_{13}] &= \frac{N|\mu_{13}|^2}{\epsilon_0\hbar}\frac{2\delta\omega(4\delta\omega\Delta\omega_p - \gamma_{21}\gamma_{31} - \Omega_c^2) + 2\gamma_{21}(\gamma_{21}\Delta\omega_p + \delta\omega\gamma_{31})}{(4\delta\omega\Delta\omega_p - \gamma_{21}\gamma_{31} - \Omega_c^2)^2 + 4(\gamma_{21}\Delta\omega_p + \delta\omega\gamma_{31})^2} \\
\Im[\chi_{13}] &= -\frac{N|\mu_{13}|^2}{\epsilon_0\hbar}\frac{4\delta\omega(\gamma_{21}\Delta\omega_p + \delta\omega\gamma_{31}) - \gamma_{21}(4\delta\omega\Delta\omega_p - \gamma_{21}\gamma_{31} - \Omega_c^2)}{(4\delta\omega\Delta\omega_p - \gamma_{21}\gamma_{31} - \Omega_c^2)^2 + 4(\gamma_{21}\Delta\omega_p + \delta\omega\gamma_{31})^2}
\end{aligned} \tag{C.18}$$

which if $\delta\omega = \Delta\omega_p$, becomes

$$\begin{aligned}
\Re[\chi_{13}] &= \frac{N|\mu_{13}|^2}{\epsilon_0\hbar}\frac{8\Delta\omega_p^3 + 2\gamma_{21}^2\Delta\omega_p - 2\Omega_c^2\Delta\omega_p}{(4\Delta\omega_p^2 - \gamma_{21}\gamma_{31} - \Omega_c^2)^2 + 4\Delta\omega_p^2(\gamma_{21} + \gamma_{31})^2} \\
\Im[\chi_{13}] &= -\frac{N|\mu_{13}|^2}{\epsilon_0\hbar}\frac{4\gamma_{31}\Delta\omega_p^2 + \gamma_{21}^2\gamma_{31} + \gamma_{21}\Omega_c^2}{(4\Delta\omega_p^2 - \gamma_{21}\gamma_{31} - \Omega_c^2)^2 + 4\Delta\omega_p^2(\gamma_{21} + \gamma_{31})^2}
\end{aligned} \tag{C.19}$$

C.2 Adiabatic Theorem

Notice that $\Omega = \sqrt{\Omega_p^2 + \Omega_c^2}$ is reminiscent of a right triangle.

For now we will ignore decay, so the eigenvectors of Eq. **??** are

$$|\psi_0\rangle = \begin{pmatrix} \frac{\Omega_c}{\Omega} \\ \frac{-\Omega_p}{\Omega} \\ 0 \end{pmatrix} = \begin{pmatrix} \cos\theta \\ -\sin\theta \\ 0 \end{pmatrix}; \qquad |\psi_\pm\rangle = \frac{1}{\sqrt{2}}\begin{pmatrix} \pm\frac{\Omega_p}{\Omega} \\ \pm\frac{\Omega_c}{\Omega} \\ 1 \end{pmatrix} = \frac{1}{\sqrt{2}}\begin{pmatrix} \mp\sin\theta \\ \mp\cos\theta \\ 1 \end{pmatrix} \tag{C.20}$$

or, in terms of the free atom basis functions,

$$\begin{aligned}\psi_0 &= \cos\theta\psi_1 - \sin\theta\psi_2 \\ \psi_+ &= -\frac{\sin\theta}{\sqrt{2}}\psi_1 - \frac{\cos\theta}{\sqrt{2}}\psi_2 + \frac{1}{\sqrt{2}}\psi_3 \\ \psi_- &= \frac{\sin\theta}{\sqrt{2}}\psi_1 + \frac{\cos\theta}{\sqrt{2}}\psi_2 + \frac{1}{\sqrt{2}}\psi_3.\end{aligned} \tag{C.21}$$

In general, the atoms will be in a state described by

$$\psi(t) = A_0(t)\psi_0(t) + A_-(t)\psi_-(t) + A_+(t)\psi_+(t) \tag{C.22}$$

where the states are time dependent because θ can be time dependent. The action of the Hamiltonian on this state at any particualr time is to multiply each basis state by the corresponding eigenvalue,

$$H(t)\psi(t) = -\Omega(t)A_-(t)\psi_-(t) + \Omega(t)A_+(t)\psi_+(t). \tag{C.23}$$

The time derivative of the state is given by

$$\frac{d\psi(t)}{dt} = \left(\dot{A_0} + \frac{A_-\dot{\theta}}{\sqrt{2}} - \frac{A_+\dot{\theta}}{\sqrt{2}}\right)\psi_0 + \left(\dot{A_-} - \frac{A_0\dot{\theta}}{\sqrt{2}}\right)\psi_- + \left(\dot{A_+} + \frac{A_0\dot{\theta}}{\sqrt{2}}\right)\psi_+ \tag{C.24}$$

. Eqs. C.23 and C.24 are related to each other by the Schrödinger equation $d\psi/dt = -iH\psi$. That relationship can be reexpressed in matrix form as

$$\begin{pmatrix}\dot{A_o} \\ \dot{A_-} \\ \dot{A_+}\end{pmatrix} = \begin{pmatrix}0 & -\frac{\dot{\theta}}{\sqrt{2}} & \frac{\dot{\theta}}{\sqrt{2}} \\ \frac{\dot{\theta}}{\sqrt{2}} & i\Omega(t) & 0 \\ -\frac{\dot{\theta}}{\sqrt{2}} & 0 & -i\Omega(t)\end{pmatrix}\begin{pmatrix}A_0 \\ A_- \\ A_+\end{pmatrix}. \tag{C.25}$$

As the probe beam is turned on we want the atoms to remain in the ground state. Using Eq. C.25, we can see that the condition fr this is that the contributions to states

ψ_- and ψ_+ from the off diagonal elements are small compared to the contributions from the diagonal elements.

$$\dot{\theta} << \Omega(t). \tag{C.26}$$

Another way to think of this is that A_- or A_+ are rotating through the complex plane at a rate of $\Omega(t)$. With the off-diagonal elements present, there will be additional contributions proportional to $\dot{\theta}$. However, if $\dot{\theta}$ changes slowly as compared to the time $A_\pm$ takes to rotate through the complex plane ($\Omega(t)$), then in one rotation the off-diagonal element contributions have constant magnitude but phases relative to $A_\pm$ that are uniformly distributed between 0 and 2π. Therefore, these contributions will sum to zero.

Using $\theta = \tan^{-1}(\Omega_p/\Omega_c)$, Eq. C.26 becomes

$$\frac{\frac{d}{dt}\left(\frac{\Omega_p}{\Omega_c}\right)}{1+\left(\frac{\Omega_p}{\Omega_c}\right)^2} << \Omega(t) \tag{C.27}$$

However, we have the additional conditions, at least in our case, that Ω_c is a constant and is much larger than Ω_p at all times. Therefore the adiabatic condition simplifies to

$$\frac{d\Omega_p}{dt} << \Omega_c^2. \tag{C.28}$$

Appendix D

Magnetic Dipole Verification: Standing Waves

D.1 A Brief Introduction: What were we trying to do?

Back in late 2015 and early 2016, we were working on a Rabi flopping experiment on an optical transition that we suspected was a magnetic-dipole transition with the intention of characterizing the transition's interaction with the magnetic field of our beam. We used an intense green laser at 527 nm to induce the flopping behavior and observed the transmission after various durations of flopping. However, it is well known that Rabi flopping can occur due to interactions with the electric field as well. Thus, there was still the need to conclusively verify that our transition was indeed a magnetic-dipole transition and we weren't seeing any electric effects. The fate of the lab was in the balance.

D.2 How did we try to do this?

The short answer is several different ways. The long answer is:

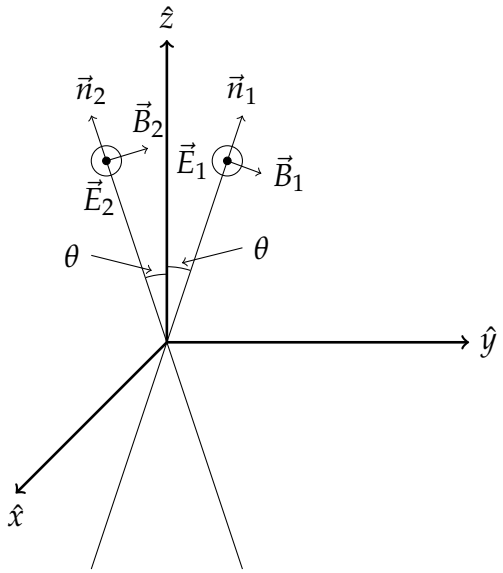

Figure D.1: Visualization of the beams. Each beam is described by a propagation direction $\hat{n}$, electric field $\vec{E}$, and a magnetic field $\vec{B}$. The beams are propagating in the yz plane with the z-axis bisecting the angle between propagation directions.

D.2.1 Standing waves

Our first few attempts at identifying the nature of the transition were centered around an interesting property of standing waves. Imagine two beams of the same frequency that cross each other at an angle 2θ. Without loss of generality, we can put a coordinate system in such that the beams are propagating in the yz plane and each beam's k-vector is an angle θ from the z-axis. See Fig. D.1.

In the figure, $\hat{n}$, $\vec{E}$, and $\vec{B}$ are the propagation direction, elecric field vector, and magnetic field vector, respectively[1]. We assume that the beams have the same amplitude and the electric fields are both pointing out of the page. The same analysis can be done with the magnetic field pointing out of the page. In this case one would get the same results except the electric and magnetic fields would be switched. In general, there can

[1]We assume right-handed waves throughout.

also be a phase difference between the two beams. We have for the electric fields

$$\vec{E}_1 = E_0 e^{i(k\hat{n}_1\cdot\vec{r}-\omega t)}\hat{x} \tag{D.1a}$$

$$\vec{E}_2 = E_0 e^{i(k\hat{n}_2\cdot\vec{r}-\omega t+\phi)}\hat{x} \tag{D.1b}$$

From Fig. D.1 we see that the propagation directions can be written as

$$\hat{n}_1 = \sin\theta\hat{y} + \cos\theta\hat{z} \tag{D.2a}$$

$$\hat{n}_2 = -\sin\theta\hat{y} + \cos\theta\hat{z} \tag{D.2b}$$

When we add the electric fields together we get

$$\begin{aligned}\vec{E}_1 + \vec{E}_2 &= E_0 e^{i(k\cos\theta z-\omega t)}\left(e^{ik\sin\theta y} + e^{-i(k\sin\theta y-\phi)}\right)\hat{x} \\ &= E_0 e^{i(k\cos\theta z-\omega t)}e^{\phi/2}\left(e^{ik\sin\theta y-\phi/2} + e^{-i(k\sin\theta y-\phi/2)}\right)\hat{x} \\ &= 2E_0 e^{i(k\cos\theta z-\omega t+\phi/2)}\cos(k\sin\theta y-\phi/2)\hat{x}\end{aligned} \tag{D.3}$$

We can find the direction of the magnetic field using Faraday's law, $\hat{n}\times\hat{E} = \omega\vec{B}$. Note that we are only considering the direction of the fields here, not the magnitude. The specific relation between the amplitudes of the electric and magnetic fields is not the important part; we only need to know that the electric field amplitude is much larger than the magnetic field amplitude. From this equation, we can see that the directions of the magnetic fields are

$$\hat{B}_1 = \cos\theta\hat{y} - \sin\theta\hat{z} \tag{D.4}$$

$$\hat{B}_2 = \cos\theta\hat{y} + \sin\theta\hat{z} \tag{D.5}$$

so the full magnetic fields are

$$\vec{B}_1 = B_0 e^{i(k\hat{n}_1\cdot\vec{r}-\omega t)}(\cos\theta\hat{y} - \sin\theta\hat{z}) \tag{D.6a}$$

$$\vec{B}_2 = B_0 e^{i(k\hat{n}_2\cdot\vec{r}-\omega t+\phi)}(\cos\theta\hat{y} + \sin\theta\hat{z}) \tag{D.6b}$$

which when added together give

$$\vec{B}_1 + \vec{B}_2 = 2B_0 e^{i(k\cos\theta z-\omega t+\phi/2)}[\cos\theta\cos(k\sin\theta y - \phi/2)\hat{y} + 2i\sin\theta\sin(k\sin\theta y - \phi/2)\hat{z}]. \tag{D.7}$$

Taking the real parts of Eqs. D.3 and D.7 gives us the physical fields,

$$\Re[\vec{E}_1 + \vec{E}_2] = \vec{E} = 2E_0\cos(k\cos\theta z - \omega t + \phi/2)\cos(k\sin\theta y - \phi/2)\hat{x} \tag{D.8}$$

$$\begin{aligned}\Re[\vec{B}_1 + \vec{B}_2] = \vec{B} =& 2B_0\cos(k\cos\theta z - \omega t + \phi/2)\cos\theta\cos(k\sin\theta y - \phi/2)\hat{y} \\ &+2B_0\sin(k\cos\theta z - \omega t + \phi/2)\sin\theta\sin(k\sin\theta y - \phi/2)\hat{z}.\end{aligned} \tag{D.9}$$

Eqs. D.8 and D.9 can be more easily understood by considering two completely antiparallel beams ($\theta = \pi/2$). Assuming $\phi = 0$ for simplicity, the fields in this case are

$$\vec{E} = 2E_0\cos(\omega t)\cos(ky)\hat{x} \tag{D.10}$$

$$\vec{B} = -2B_0\sin(\omega t)\sin(ky)\hat{z} \tag{D.11}$$

This is a very interesting result! It shows that, when the beams are counterpropagating, the spatial maxima of the electric and magnetic fields are $\pi/2$ out-of-phase (so are the temporal maxima, but those will average out in the experiment). If our crystal really did only respond to the magnetic field, we could, in principle, see a standing wave of crystal fluorescence (orange) alternating with the green of our laser due to scattering (our eye and cameras are more sensitive to the electric field).

The challenge with seeing the standing wave pattern of these antiparallel beams is

that it is extremely small. In fact, it is by necessity right at the diffraction limit. However, the size of the standing wave pattern can be increased by decreasing θ from $\pi/2$, or, in other words, transition the beams from antiparallel to parallel. As this is done, the counterpropagating component of the k-vector, the y component, begins to decrease corresponding to a larger effective wavelength in the y direction. The caveat is that as θ is decreased the magnetic field gains a component in the y direction. This component is in phase with the electric field and grows as θ is decreased. Therefore we must strike a balance; find a value of θ with an out-of-phase magnetic field standing wave pattern that is large enough to image but isn't washed out by the in-phase component of the magnetic field.

D.2.2 What Do We Expect to See?

An important question to ask is "just how big is this standing wave going to be?" That's a good question Zach, let me fill you in.

The counterpropagating component of the wave vector for both the electric and magnetic fields is given by $k_y = k \sin\theta = 2\pi n \sin\theta/\lambda$ where n is the index of refraction of the crystal and λ is the free space wavelength of the laser. We must keep in mind, though, that it is the intensity we will be observing. Thus, we must square the field amplitudes which corresponds to doubling the wavevector. This final intensity standing wave pattern can be thought of as having an effective k-vector of $2\pi/\lambda_{standing}$ with a length scale of $\lambda_{standing}$. Equating these wavevectors gives us the relation

$$\frac{2n\sin\theta}{\lambda} = \frac{1}{\lambda_{standing}}. \tag{D.12}$$

Since we have an idea of how small of an object we can image, we can set this and solve

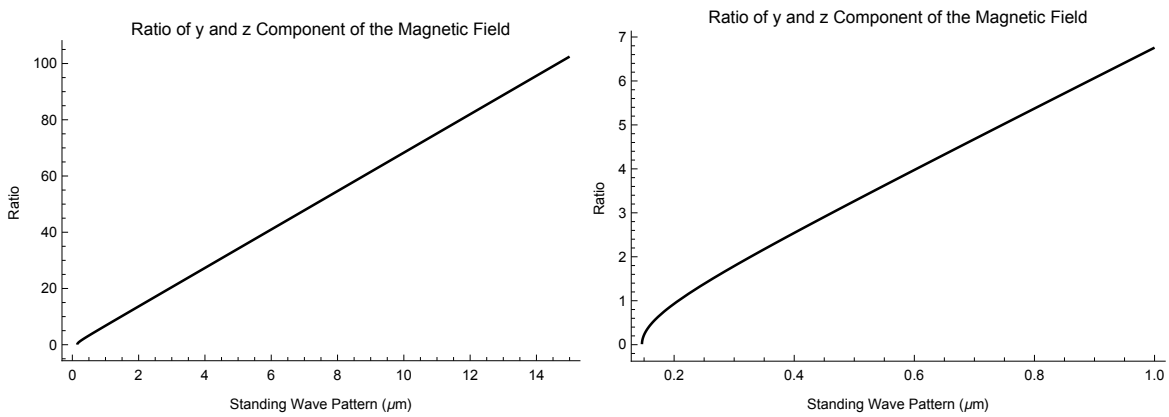

Figure D.2: Plot of the ratio of the components of the magnetic field, B_y/B_z. The plot on the left shows the relation becoming linear for large standing wave patterns and the plot on the right is zoomed in to show to show the lower limit behavior.

Eq. D.12 for θ as a function of $\lambda_{standing}$,

$$\theta = \arcsin\left(\frac{\lambda}{2n\lambda_{standing}}\right). \tag{D.13}$$

The next thing we need to consider is the relative amplitudes of the magnetic field components. What we want is to be able to destinguish fluorescence caused by the magnetic field from any fluorescence that might be caused by the electric field. Because one of the magnetic field components is in phase with the electric field, we must be careful in attributing the source of the fluorescence. Since the beams are oscillating much faster than the response time of our detectors, the terms $\cos^2(k\cos\theta z - \omega t)$ and $\sin^2(k\cos\theta z - \omega t)$ will average out and cancel. Thus the amplitude ratios are

$$\frac{B_y}{B_z} = \cot\theta = \cot\left(\arcsin\left(\frac{\lambda}{2n\lambda_{standing}}\right)\right). \tag{D.14}$$

This equation can be expanded around small values of $1/\lambda_{standing}$ to show the limiting

behavior of the ratio as $\lambda_{standing}$ becomes large.

$$\cot\left(\arcsin\left(\frac{\lambda}{2n\lambda_{standing}}\right)\right) \approx \frac{2n\lambda_{standing}}{\lambda} - \frac{\lambda}{4n\lambda_{standing}} + ... \tag{D.15}$$

For our values of n and λ this is equal to[2]

$$6.83\lambda_{standing} - \frac{0.073}{\lambda_{standing}} + ... \tag{D.16}$$

Plots of Eq. D.14 can be seen in Fig. D.2 depicting this linear behavior. Just for reference, the expansion of θ for large $\lambda_{standing}$ is given by

$$\theta \approx \frac{\lambda}{2n\lambda_{standing}} + ... = \frac{0.146}{\lambda_{standing}} + ... \tag{D.17}$$

D.2.3 Standing Wave Experiment Variant 1: Crisscrossed Beams

The idea for this experiment was to try and image the standing wave pattern with the beams almost copropagating (θ small). To see the magnetic field pattern, a long pass filter was used to block the green light and let through the orange fluorescence. The electric field pattern would be seen using a short pass filter that blocked the orange. In theory, by comparing the recorded intensity patterns of the electric and magnetic field, we would be able to see if the orange pattern lined up with the green pattern like we expect. The imaging was done with a ccd camera.

We used an Air Force resolution target to get an idea of how small of a pattern could be seen using a short focal length lens. Based on the resolution target, the smallest object that could be resolved with the camera/lens combo was about 5 μm. From Eq. D.14, this means that the ratio of the in-phase to the out-of-phase components of the magnetic field was 34.2, which corresponds to an angle of $\theta = 0.029$ or 1.7°. However, since we

[2]All lengths are in μm

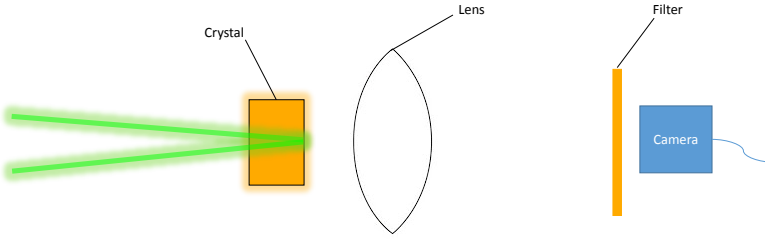

Figure D.3: The experimental setup. A different filter was used depending on whether we were trying to observe the electric or magnetic fields. The camera was connected to a computer through a BNC cable. The camera was a Watec ccd camera originally meant for closed circuit security recording.

would actually be measuring intensities, the ratio we would expect to observe with the camera was $34.2^2 = 1170$. The experimental setup can be seen in Fig. D.3.

Using this setup we weres able to see standing wave patterns. In fact, the electric field standing wave was pretty easy to see; we actually had to use ND filters to cut down on the brightness, see Fig. D.4. The magnetic field, however, was harder to see. The in-phase component of the magnetic field, right side of Fig. D.4, was barely visible. The factor of 1170 reduction in intensity from the small crossing angle made it impossible to see the out-of-phase component. Better results could have potentially been obtained with a better camera. The Watec camera used in this setup did not allow for ISO control (the ISO automatically adjusted). The camera we used also didn't have any cooling mechanism or use any other noise reduction methods. We did not try this particular setup with the camera from the localization experiment.

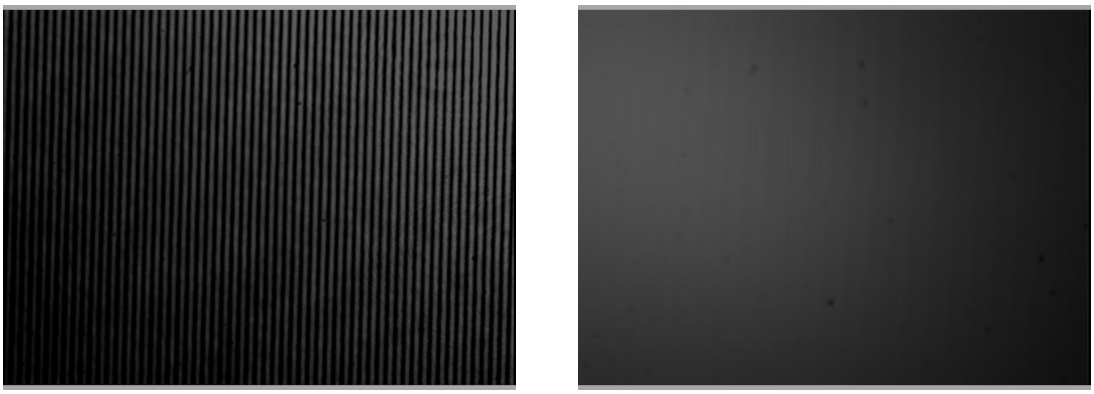

Figure D.4: Images taken with the setup in Fig. D.3. The left side of this figure is the electric field standing wave after going through an ND filter and the right side is the in-phase magnetic field pattern. The out-of-phase pattern could not be imaged this way.

D.2.4 Standing Wave Experiment Variant 2: A New Hope?

With the setup from the previous section looking like it wasn't going to work, we decided to change things up a bit. Although we couldn't image the standing wave when $\theta = \pi/2$ directly, we still might be able to distinguish the intensity maxima from the minima. The idea was to place a very small aperture between the crystal and the lens in order to select a small slice of the standing wave. Although we might not be able to resolve the aperture, we know what part of the standing wave the light is coming from. The amount of light getting through an aperture of width w is given by

$$\int_x^{x+w} \sin^2(k\theta)d\theta = \frac{w}{2} - \frac{1}{2k}(\sin(x+w)\cos(x+w) - \sin(x)\cos(x)) \tag{D.18}$$

where k is the wavevector of the standing wave pattern and x is the position of the aperture. If this expression gives the in-phase component, the out-of-phase component is given by

$$\frac{w}{2} + \frac{1}{2k}(\sin(x+w)\cos(x+w) - \sin(x)\cos(x)) \tag{D.19}$$

Both of these expressions are in arbitrary units. See Fig. D.5 for more details.

We went through numerous iterations of this experiment while we smoothed out all the issues that came up. In order to get a decent signal, there must be a balance between having a large enough out-of-phase signal, having fine enough control over the aperture location, and not having an aperture width that is a multiple of the standing wave scale (Eqs. D.18 and D.19 are zero in this case), see Fig. D.5. In the last iteration we overcame these difficulties by using a 1 μm slit glued to a piezo and set $\theta = 0$. With $\theta = 0$ the out-of-phase component is maximized and using a slit instead of of a pinhole increased the signal. Putting it on a piezo meant that we could have very fine control over the displacement of the slit. The piezo also, at least in theory, helped us overcome another problem. Since our standing wave was so small, even small mechanical vibrations could throw off our measurements. The piezo would allow us to move the slit faster than these vibratons. The presence of vibrations also required us to measure the magnetic and electric field standing waves at the same time. We did this by using a beam splitter, a couple of filters, and a couple of photon counters, see Fig. D.6.

Dispite our best efforts, we were not able to see the magnetic field standing wave. The conclusion was that there were two reasons for this: the signal was too small and there were too many vibrations caused by driving the piezo. However, we were able to see the electric field, although just barely. This was confirmed by blocking the beam and seeing the signal on the oscilloscope change. If we were to try this again, the best bet would be to try a larger value of θ to increase the amplitude of the out-of-phase component as suggested in Fig. D.5.

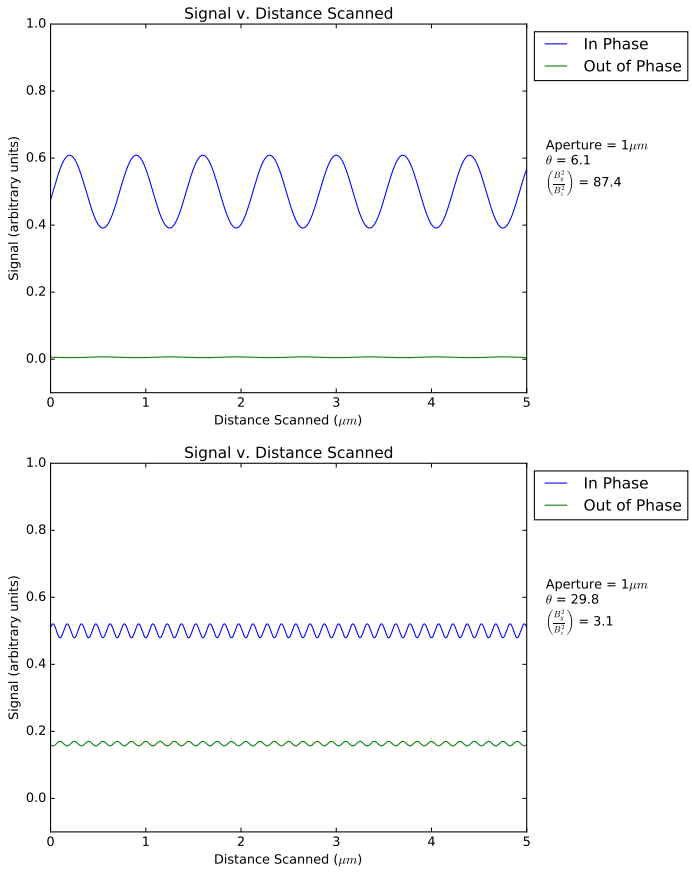

Figure D.5: The expected in-phase and out-of-phase signals for different values of θ with the same size aperture. In both plots, the out-of-phase signal is divided by the intensity ratio. Using a small value of θ can lead to a high contrast for the in-phase signal, however due to the large ratio of intensities, the contrast of the out-of-phase signal is much smaller (left). At a larger angle, the out-of-phase component has higher contrast at the expense of lower contrast for the in-phase component and a much shorter signal period, which requires finer control of the aperture (right)

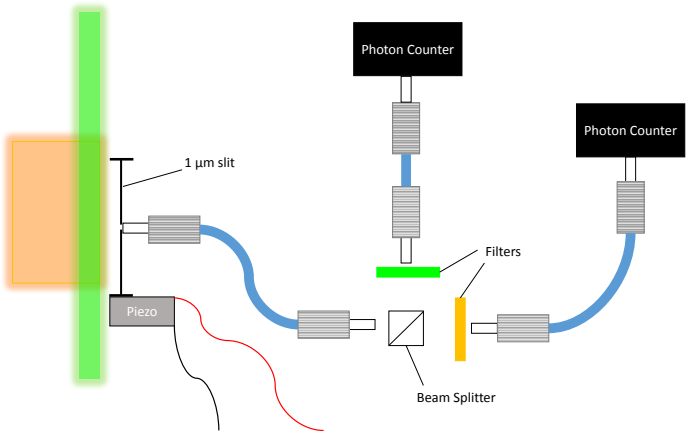

Figure D.6: Experimental Setup. The actual setup included some mirrors to align the fibers. The piezo was driven at many different frequencies. As we changed the driving freqency, it became apparent that there was some resonance with the table, which added to the noise in the signal. This setup was on a separate table from the table with the laser and SHG cavity on it. This was to prevent the piezo vibrations from adding more noise by disrupting the incoming laser.

Appendix E

Measurement of the Index of Refraction using the Free Spectral Range of a Fabry-Perot Cavity

Our externally dirven scheme for negative indices calls for a second order electric response induced in the host crystal. In order to properly induce this second order response and produce the second harmonic, we must accurately know the indices of refraction at the fundamental frequency, in this case 1055 nm. The Sellmeier coefficients for YSO were reported in [65]. However, their measurements were only taken out to about 650 nm. Although we do not expect there to be any resonances between 650 nm and 1055 nm and could likely just use the equations from [65] (or use another host crystal), we started looking into ways in which we could measure the index ourselves.

In this appendix, I go through a scheme I came up with to use a technique that precisely measures the free spectral range of a Fabry-Perot cavity to measure the index of refraction of our crystal. The introduction goes through a qualitative description of why we need to know the indices for SHG. Then I go through an over view of Fabry-Perot cavities, followed by a description of a technique for measuring the free spectral

range. Last I go through a quantitative calculation to determine what sort of precision we could expect from this method.

E.1 Introduction

In general, the index of refraction is frequency dependent. The result of this is that frequency components of different frequencies propagate with different velocities. One consequence of this dispersion is that a short pulse, which is composed of many frequency components, will spread out in time as it propagates through the material.

The aspect of the index of refraction that draws our attention is its involvement in second harmonic generation (SHG). As a wave with a particular frequency, which we will refer to as the fundamental frequency, propagates through a material it produces a polarization in that material that oscillates at the fundamental frequency. Since this polarization wave is driven by the electromagnetic wave it will propagate with the same velocity as the electromagnetic wave. Due to nonlinearities in the materials response the polarization wave will also have frequency components that are twice the fundamental frequency, a frequency which we will refer to as the second harmonic frequency. Because it is composed of oscillating charges, the polarization wave will emit electromagnetic waves of its own that oscillate at the same frequency as the polarization. Thus the polarization wave will generate electromagnetic waves at the second harmonic frequency which, due to dispersion, will propagate at a velocity different from the velocity of the electromagnetic wave that generated the polarization in the first place. At any given point in an isotropic medium, this discrepancy in velocities, and therefore phases, will lead to destructive interference between the second harmonic light being generated at that point and second harmonic light that was generated upstream sometime in the past [104].

One can get around this destructive interference by using an anisotropic material such

as YSO. In an anisotropic medium the index of refraction is direction and polarization dependent. Consider a beam of light with a particular polarization, the fundamental beam, propagating in a particular direction in an anisotropic medium. As discussed above, this beam, facilitated by the nonlinearities of the material, will generate its second harmonic. If this second harmonic has the same polarization as the fundamental beam, then there will be destructive interference. However, due to the anisotropy of the medium, a different polarization will propagate with a different velocity. If the direction of propagation is chosen carefully, then second harmonic light generated with a polarization different from the polarization of the fundamental beam could propagate with the same velocity as the fundamental beam therefore avoiding the destructive interference from the previous paragraph.

In order to produce second harmonic light, one must know the index of refraction's dependence on direction and frequency. Measuring the index over these parameters is the goal of this experiment.

E.2 Fabry-Perot Cavities

A Fabry-Perot cavity is basically just two mirrors facing each other. Mirrors in this configuration will have a resonance with particualr modes of the electromagnetic field. Often, the mirrors will be curved to tune the resonance to a particular spatial mode. The length of the cavity selects the frequency. See Fig. E.1. We will consider a lossless cavity with mirrors that have the same reflection and transmission coefficients. In general the reflection and transmission coefficients of the two mirrors will not be the same, and the cavity will not be lossless. However, the following procedure can still be used in the general case.

A quantity that is often of interest when using a Fabry-Perot cavity is the steady state circulating power. This quantity can be written as a function of the cavity parameters as

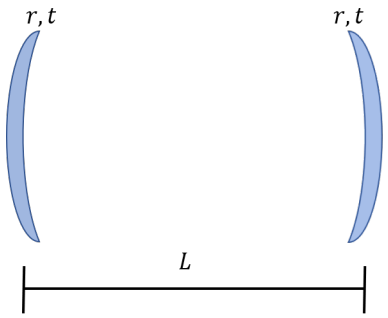

Figure E.1: A Fabry-Perot cavity of length L. Due to the finite size of L, the modes of the cavity will have discrete frequencies. The curvature of the mirrors select which spatial modes of the electromagnetic field will be resonant with the cavity. These spatial modes are often described using the Hermite-Gauss polynomials. See [121] for more details. The amount of steady state circulating power inside the cavity is determined by the reflection and transmission coefficients of the two mirrors. The field reflection and transmission coefficients, r and t, for our example are the same for both mirrors. The cavity is assumed to be lossless.

well as the frequency of the incident light and is used in a variety of calculations. In this case, we are interested in calculating the amplitude and phase of the transmitted light.

The circulating field amplitude can be calculated by considering the steady state buildup step by step as shown in Fig. E.2. We start with a beam of amplitude E_i incident on a cavity with no field inside it. Immediately after the beam hits the first mirror, the field just inside the mirror is tE_i (Fig. E.2a). A short time later, that first light has made one complete round trip through the cavity. The amplitude is then modified by the reflectivities of each mirror (along with any cavity losses, which we ignore here) as well as a phase factor for propagating through space resulting in an amplitude of $tE_i r^2 e^{2ikL}$. However, the incident beam is still on, so there is still light entering the cavity with an amplitude of tE_i. The resulting total amplitude just inside the first mirror after this first round trip is $tE_i + tE_i r^2 e^{2ikL}$ (Fig. E.2b). After the second round trip, the field amplitude just inside the first mirror is $tE_i + tE_i r^2 e^{2ikL} + tE_i (r^2 e^{2ikL})^2$. We continue adding up the

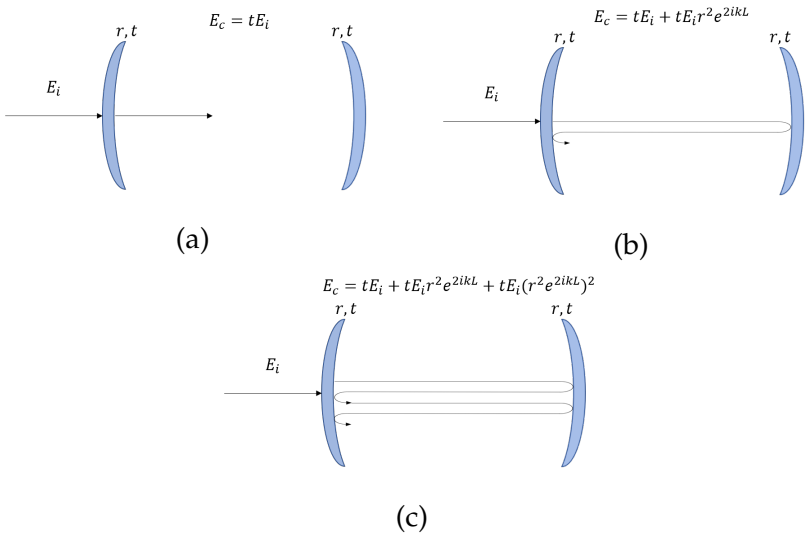

Figure E.2: A Fabry-Perot cavity of length L. The field reflection and transmission coefficients, r and t, are the same for both mirrors. The cavity is assumed to be lossless.

field amplitude after each successive round trip and end up with a geometric series

$$E_c = tE_i \sum_{n=0}^{\infty} (r^2 e^{2ikL})^n = \frac{tE_i}{1 - r^2 e^{2ikL}} = \frac{tE_i(1 - R\cos(2kL) + iR\sin(2kL))}{1 + R^2 - 2R\cos(2kL)} \tag{E.1}$$

where $R = r^2$.

Before we continue, we will introduce a convenient quantity called the free spectral range (FSR). The FSR is the fundamental frequency of the cavity. For a Fabry-Perot cavity it is given by the formula

$$\nu_{FSR} = \frac{2L}{c}. \tag{E.2}$$

We can use the result in Eq. E.1 to calculate the intensity transmission coefficient of the cavity as well as the phase of the transmitted field. The expressions we get for these quantities, in terms of the FSR, are

$$T_c = \frac{|E_t|^2}{|E_i|^2} = \frac{|tE_c|^2}{|E_i|^2} = \frac{T}{1 + R^2 - 2R\cos\left(2\pi\frac{\nu}{\nu_{FSR}}\right)}; \qquad \phi = \arctan\left(\frac{R\sin\left(2\pi\frac{\nu}{\nu_{FSR}}\right)}{1 - R\cos\left(2\pi\frac{\nu}{\nu_{FSR}}\right)}\right). \tag{E.3}$$

These quantities are plotted in Fig. E.3.

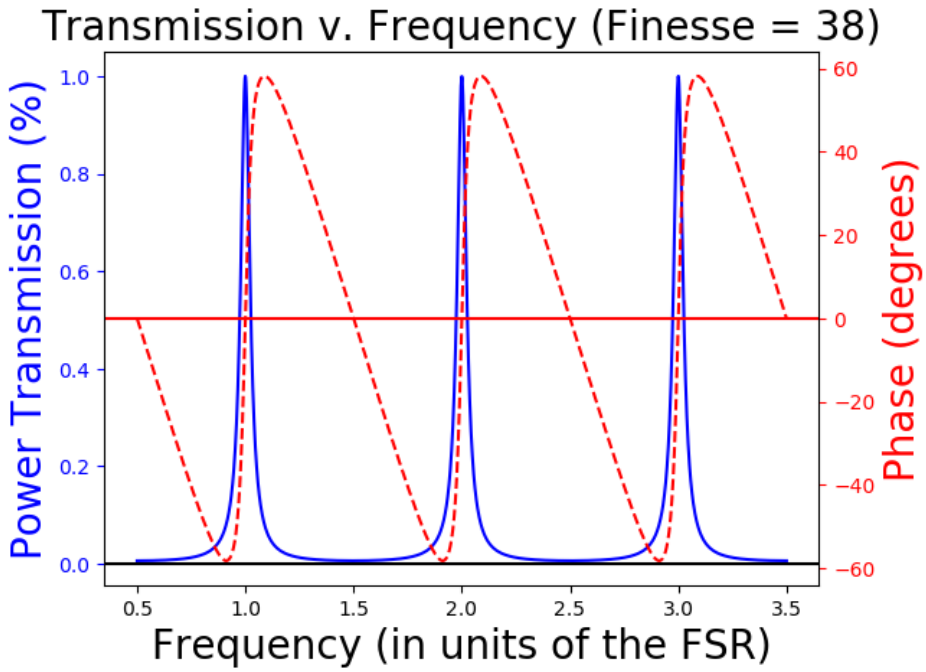

Figure E.3: The amplitude and phase of a beam transmitted through a Fabry-Perot relative to the incident beam. We are assuming that the there is no absorption within the cavity and $r^2 + t^2 = 1$.

E.3 FSR Measurement

The FSR measurement technique we are discussing here was developed in the 1990's in the context of gravitational wave measurements [122] and metrology [123] and grew out of techniques from surveying and geology [124, 125] and frequency locking [76, 126].

The main idea is to use the sharp phase and amplitude properties of the Fabry-

Perot cavity in Fig. E.3 to create a beat frequency pattern that is extremely sensitive to detuning. This is done by using a device such as an EOM to modulate the light that is incident on the cavity. The modulation frequency is at about, but not quite the FSR, shown in Fig. E.4. In addition the central band of the beam is slightly detuned from resonance with the cavity. When these conditions are met, then the beam's sidebands will wind up with very different amplitudes and phases due to the sharp frequency dependence of the Fabry-Perot. The result is a beat pattern between the beam's bands that has a very strong dependence on the EOM's frequency.

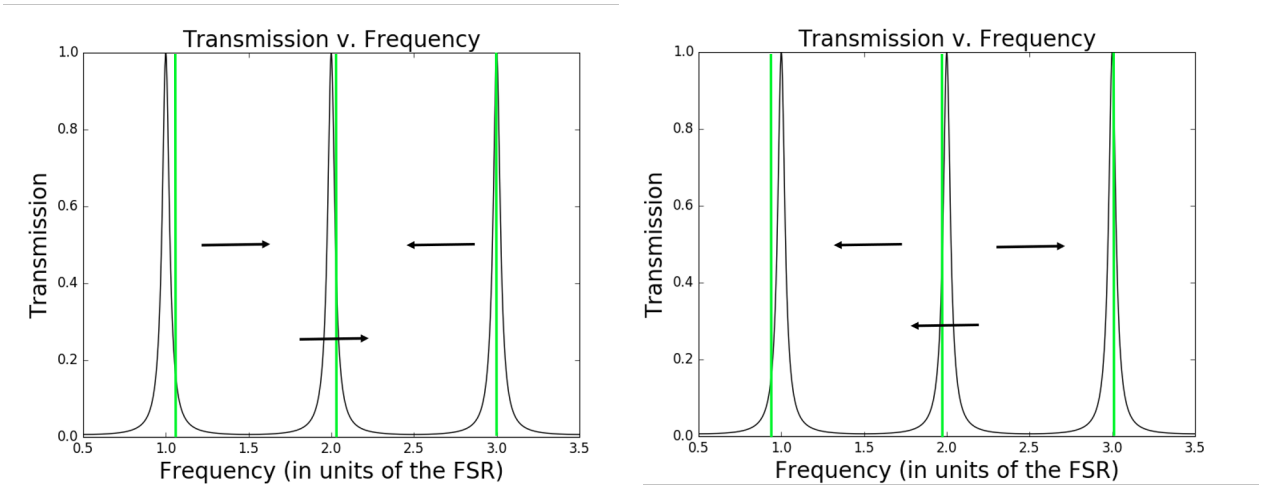

Figure E.4: The output of an EOM (green) overlaid on the amplitude transmission function of a Fabry-Perot cavity. If the EOM's modulation frequency is slightly off from the FSR and the beam's central band is slightly off resonance, then the rapid variation of the Fabry-Perot's transmission function will cause a beat pattern between the beam's bands that is highly dependent on the EOM's frequency. On the left the EOM's frequency is slightly below the FSR and the center beam is red detuned from resonance. The right hand plot has both of these features reversed.

The resulting beat pattern can be seen in Fig. E.5. The figure clearly shows a very sharp variation of the beat pattern as the modulation frequency is changed. After zooming in three times, we see that this technique can measure the FSR to better than one

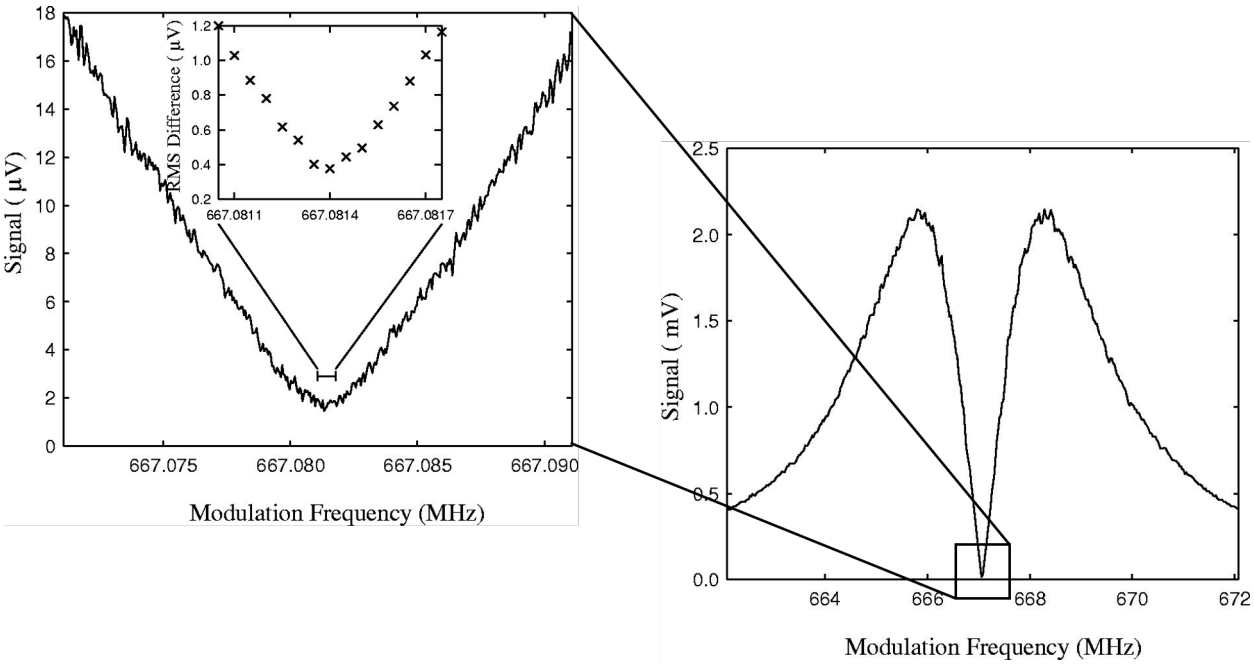

Figure E.5: The modulation frequency dependent beat pattern in the transmitted beam. Reproduced from [123] with permission of AIP publishing.

part in a million. This precision can be made even higher with a higher finesse and/or beam intensity.

E.4 Experiment with YSO

The high precision this technique offers in measuring the FSR translates into a high precision measurement of the optical path length within the cavity and thus the index of refraction. An example of a future setup is shown in Fig. E.6. Because out crystals are cut with its optical axes perpendicular to the surfaces, the placement of the crystal in Fig. E.6 adds the effects of one of the principle indices of refraction to the optical path length difference. by either using crystals of different length or changing the medium around the crystal, we can get a precise measurement of the principle indices of refraction.

The most straightforward way to measure the index of refraction is to solve the equa-

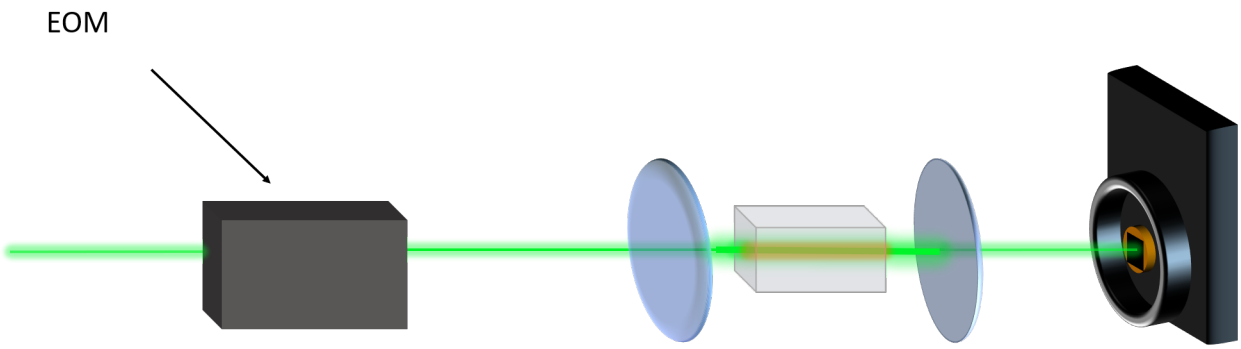

Figure E.6: A simplified schematic of the experimental setup

tion for the FSR for the index of refraction

$$\nu_c = \frac{c}{2(L_{nc} + n_c L_c)} \quad \Leftrightarrow \quad n_c = \frac{1}{L_c}\left(\frac{c}{2\nu_c} - L_{nc}\right). \tag{E.4}$$

Because the index is a function of L_c, L_{nc}, and ν_c the form of the uncertainty in the index is

$$\Delta n^2 = \left[\frac{-1}{L_c^2}\left(\frac{c}{2\nu_c} - L_{nc}\right)\right]^2 \Delta L_c^2 + \left[\frac{-c}{2L_c\nu_c^2}\right]^2 \Delta\nu_c^2 + \left[\frac{-1}{L_c}\right]^2 \Delta L_{nc}^2. \tag{E.5}$$

Plugging in the values from Sec. E.4 into Eq. E.5 we get

$$\Delta n^2 = (10^4 m^{-2})\Delta L_c^2 + (4\times 10^{-17}) Hz^{-2}\Delta\nu_c^2 + (10^4 m^{-2})\Delta L_{nc}^2. \tag{E.6}$$

Parameters

To get a quantitative idea of the accuracy of this method, I will use the geometric parameters of our ULE cavity. Since there will be a crystal in the cavity for this experiment, the finesse should be closer to that of the SHG cavity.

- L_0 = 10 cm: length of cavity with nothing in it
- L_c = 1 cm: length of the crystal
- L_{nc} = 9 cm: length of whatever is not the crystal ($L_{notcrystal}$)

- ν_0 = 1.5 GHz: FSR with no crystal
- w_0 = 180 μm: waist of the beam inside the cavity
- R = 20 cm: radius of curvature of the curved cavity mirror

- $\mathcal{F} \approx 40$: Finesse of the cavity. This factor is limited due to losses from the crystal interfaces and absorption.
- $\nu_0' \approx 1.5$ GHz: FSR with no crystal, but the cavity is filled with gas (or liquid)
- $\nu_c \approx 1.5$ GHz: FSR with the crystal
- $\nu_c' \approx 1.5$ GHz: FSR with the crystal and the cavity is filled with gas (or liquid)

- n_c: index of refraction of the crystal
- n_{nc}: index of refraction of whatever is not the crystal

- c: speed of light in vacuum

Measurement

The methods described in [123, 127, 122] are capable of measuring the FSR to level of ones to tens of Hz. Even if our measurement was much worse, the coefficient of the second term on the right of Eq. E.6 is so small that I argue we can drop it.

Both the length uncertainties will be limited by ΔL_c. This is because the total length of the cavity, L_0, can be measured very precisely by measuring the FSR with no crystal, ν_0'. Then $L_{nc} = L_0 - L_c$ and the uncertainty will be dominated by ΔL_c. We then get

$$\Delta n_c = 141 m^{-1} \Delta L_c \tag{E.7}$$

Typical calipers can measure lengths to the level of 5×10^{-5} m. This would give $\Delta n_c = 0.007$. This doesn't give us as many decimals as is known for KTP, but it does put us in the ballpark of the index for YSO at 527 nm.

Improved Measurement

A measurement of ν_c gives the total optical length of our cavity. Therefore, we need a way to separate out the two lengths from the index of refraction. One way to do this, as described above, is to use calipers. However, I believe we can potentially get a much more precise measurement by making FSR measurements of different configurations of the cavity.

The first step would be to measure the FSR with and without the crystal in vacuum, ν_c and ν_0'. This would then give us

$$\frac{c}{2\nu_0} - \frac{c}{2\nu_c} = L_0 - (L_{nc} + n_c L_c) = (n_c - 1)L_c. \tag{E.8}$$

The uncertainty in $L_0 = c/2\nu_0$ is

$$\Delta L_0 = \frac{c}{2\nu_0^2}\Delta\nu_0 = 6.67 \times 10^{-11}\text{Hz}^{-1}\Delta\nu_0. \tag{E.9}$$

Here we are still stuck with a combination of n_c and L_c, neither of which is known separately. However, by making two more FSR measurements, we can find L_{nc} and replace L_c with $L_0 - L_{nc}$. These measurements involve measuring the FSR while the cavity is filled with a gas or liquid instead of vacuum.

For the measurement of L_{nc} to be precise, we must know the index of whatever is filling the cavity that is not the crystal, n_{nc}. A measurement of the FSR without the crystal but with the non-vacuum, ν_0', gives us

$$n_{nc} = \frac{c}{2\nu_0'\nu_0} = \frac{\nu_0}{\nu_0'} \tag{E.10}$$

with uncertainty

$$\Delta n_{nc}^2 = \left(\frac{1}{\nu_0'}\right)^2 \Delta\nu_0^2 + \left(\frac{\nu_0}{\nu_0'^2}\right)^2 \Delta\nu_0'^2. \tag{E.11}$$

We can estimate the uncertainty by setting $\nu_0' \approx \nu_0 = 1.5$ GHz (this slightly underestimates the uncertainty)

$$\boxed{\Delta n_{nc} = 9.4 \times 10^{-10}\text{Hz}^{-1}\Delta\nu_0.} \tag{E.12}$$

Now all that is left is to measure L_{nc}. This can be done by measuring the FSR with both the crystal and extra gass/liquid, ν_c'.

$$\nu_c' = \frac{c}{2(n_{nc}L_{nc} + n_c L_c)} \quad \Leftrightarrow \quad L_{nc} = \frac{1}{n_{nc}-1}\left[\frac{c}{2\nu_c'} - \frac{c}{2\nu_c}\right]. \tag{E.13}$$

L_{nc} has an uncertainty of

$$\Delta L_{nc}^2 = \left(\frac{c}{2(n_{nc}-1)\nu_c'^2}\right)^2 \Delta\nu_c'^2 + \left(\frac{c}{2(n_{nc}-1)\nu_c^2}\right)^2 \Delta\nu_c^2 + \frac{1}{(n_{nc}-1)^2}\left[\frac{c}{2\nu_c'} - \frac{c}{2\nu_c}\right]\Delta n_{nc}^2. \tag{E.14}$$

If the cavity is filled with water so that $n_{nc} = 1.33$, then $\nu_c' = \nu_c/1.33$. If we use this assumption, set $\Delta\nu_c' = \Delta\nu_c$, and factor out $1/(n_{nc}-1)$ Eq. E.14 gives us

$$\Delta L_{nc} = \frac{7.3 \times 10^{-10}\text{Hz}^{-1}}{n_{nc}-1}\Delta\nu_c. \tag{E.15}$$

If $n_{nc} < 1.33$ than the numerator in the above equation is too large.

Now we have all the pieces to find n_c which is given by Eq. E.8

$$n_c - 1 = \frac{1}{L_0 - L_{nc}}\left[\frac{c}{2\nu_0} - \frac{c}{2\nu_c}\right]. \tag{E.16}$$

The uncertainty for n_c is

$$\Delta n_c^2 = \left(\frac{n_c - 1}{L_0 - L_{nc}}\right)^2 (\Delta L_0^2 + \Delta L_{nc}^2) + \left(\frac{1}{L_0 - L_{nc}}\frac{c}{2\nu_0^2}\right)^2 \Delta\nu_0^2 + \left(\frac{1}{L_0 - L_{nc}}\frac{c}{2\nu_c}\right)^2 \Delta\nu_c^2 \tag{E.17}$$

where Eq. E.16 has been used to simplify the expression. Eqs. E.9 and E.15 can be used to simplify further

$$\Delta n_c^2 = \left[\left(\frac{1}{L_0 - L_{nc}}\frac{c}{2\nu_0^2}\right)^2 + \left(\frac{n_c - 1}{L_0 - L_{nc}}6.67 \times 10^{-11}\right)^2\right]\Delta\nu_0^2 \tag{E.18}$$

$$+ \left[\left(\frac{1}{L_0 - L_{nc}}\frac{c}{2\nu_c^2}\right)^2 + \left(\frac{n_c - 1}{L_0 - L_{nc}}\frac{7.3 \times 10^{-10}}{n_{nc} - 1}\right)^2\right]\Delta\nu_c^2. \tag{E.19}$$

If we use $\nu_0 = \nu_c$ and $n_c = 1.8$ we get

$$\Delta n_c^2 = 7.3 \times 10^{-17}\text{Hz}^{-1}\Delta\nu_0^2 + 4.4 \times 10^{-17}\text{Hz}^{-1}\Delta\nu_c^2 + \frac{3.4 \times 10^{-15}\text{Hz}^{-1}}{(n_{nc} - 1)^2}\Delta\nu_c^2 \tag{E.20}$$

or

$$\boxed{\Delta n_c \approx \frac{5.8 \times 10^{-8}\text{Hz}^{-1}}{n_{nc} - 1}\Delta\nu_c} \tag{E.21}$$

E.4.1 Challenges

- Eq. E.21 shows that the larger n_{nc} the more precise the measurement. If we used air at STP, $n_{nc} = 1.0003$ and $\Delta n_c = 0.0002$. The best measurements would be made with something that would give us $n_{nc} - 1 = 0.1$ to 1. This would have to be a liquid which would make stablizing the cavity difficult.

- For Eq. E.15 to stay small we would need Eq. E.12 to stay small. This means we would have to keep the pressure and temperature of the gas very steady.

- This would be more of a problem for liquids, but filling the cavity with a high index fluid would change the mode matching conditions.

- The coefficient of thermal expansion for YSO is 7×10^{-6} C^{-1} [128]. Since the crystal is only 0.01 m long heating from the laser probably wouldn't too big of an issue, but we should be wary of it.